OPTICAL PROPERTIES OF PLASMONIC ZONE PLATE LENS, SERS-ACTIVE SUBSTRATE AND INFRARED DIPOLE ANTENNA

A Dissertation

by

HYUN CHUL KIM

Submitted to the Office of Graduate Studies of
Texas A&M University
in partial fulfillment of the requirements for the degree of

DOCTOR OF PHILOSOPHY

August 2009

Major Subject: Electrical Engineering

OPTICAL PROPERTIES OF PLASMONIC ZONE PLATE LENS, SERS-ACTIVE SUBSTRATE AND INFRARED DIPOLE ANTENNA

A Dissertation

by

HYUN CHUL KIM

Submitted to the Office of Graduate Studies of
Texas A&M University
in partial fulfillment of the requirements for the degree of

DOCTOR OF PHILOSOPHY

Approved by:

Co-Chairs of Committee, Mosong Cheng
Xing Cheng
Committee Members, Arum Han
Jorge Seminario
Head of Department, Costas N. Georghiades

August 2009

Major Subject: Electrical Engineering

ABSTRACT

Optical Properties of Plasmonic Zone Plate Lens, SERS-active Substrate and Infrared Dipole Antenna.

(August 2009)

Hyun Chul Kim, B.S.; M.S., Sungkyunkwan University

Co-Chairs of Advisory Committee: Dr. Mosong Cheng
Dr. Xing Cheng

Nowadays plasmonics is rapidly developing areas from fundamental studies to more application driven research. This dissertation contains three different research topics on plasmonics. In the first research topic, by modulating the zone width of a plasmonic zone plate, we demonstrate that a beam focused by a proposed plasmonic zone plate lens can be achieved with higher intensity and smaller spot size than the diffraction-limited conventional zone plate lens. This sub-diffraction focusing capability is attributed to extraordinary optical transmission, which is explained by the complex propagation constant in the zone regions afforded by higher refractive index dielectric layer and surface plasmons. On the other hand, the resulted diffraction efficiency of this device is relatively low. By introducing a metal/dielectric multilayered zone plate, we present higher field enhancement at the focal point. This higher field enhancement originates not only from surface plasmon polaritons-assisted diffraction process along the propagation direction of the incident light (longitude mode), but also from multiple scattering and coupling of surface plasmons along the metal/dielectric interface (transverse mode).

In the second research topic, we suggest a novel concept of SERS-active substrate applications. The surface-enhanced Raman scattering enhancement factor supported by gap surface plasmon polaritons is introduced. Due to higher effective refractive index induced by gap surface plasmon polaritons in the spacer region between two metal plates, incident light tends to localize itself mostly in the medium with higher refractive index than its adjacent ones and thereby the lights can confine with larger field enhancement.

In the last research topic, we offer a simple structure in which a gold dipole antenna is formed on the SiC substrate. Surface phonon polaritons, counterparts of surface plasmon polaritons in the mid-infrared frequencies, are developed. Due to the synergistic action between the conventional dipole antenna coupling and the resonant excitation of surface phonon polaritons, strong field enhancement in the gap region of dipole antenna is attained.

Most of research topics above are expected to find promising applications such as maskless nanolithography, high resolution scanning optical microscopy, optical data storage, optical antenna, SERS-active substrate, bio-molecular sensing and highly sensitive photo-detectors.

DEDICATION

To my family

ACKNOWLEDGEMENTS

It has been a long journey leading me to a Ph.D. degree in electrical engineering. I would like to express my sincere gratitude to my advisors, Dr. Mosong Cheng and Dr. Xing Cheng, for distributing their wisdom, experience, and encouragement. Also, I am very thankful to my committee members, Dr. Arum Han and Dr. Jorge Seminario. Without them, this dissertation would not have been accomplished. Moreover, I am deeply grateful to the Samsung Electronics from South Korea for supporting my research and study through the Human Resource Cultivation Program.

There are many friends and colleagues to whom I desire to express my gratitude: Jongun, Yongwook, Sungkyu, Hyungduk, Myungjoon, Jungmoo, Hyunsoo, Jaewon, Jaewoo, Murat, Huifeng, Dehu, Patrick, Tao-Hua, Muchuan, and association of Korean students in chemical engineering for their friendship and support in helping me through this toughest of times.

In the end, I would like to give special thanks from the deepest of my heart to my parents and family, especially my lovely wife Sookyoung, my son Dongyoung, and my daughter Chayeun, for their love, trust and encouragement, for always believing in me throughout all time during my studies.

TABLE OF CONTENTS

CHAPTER Page

LIST OF TABLES

LIST OF FIGURES

Page

Page

CHAPTER I

INTRODUCTION

1.1 Motivations of This Study

Plasmonics has the potential to play a unique and important role in enhancing the processing speed and capabilities of future integrated photonic circuitry. The role of plasmonic devices on a chip is also becoming more well-defined and can be illustrated in the graph shown in Figure 1.[1]

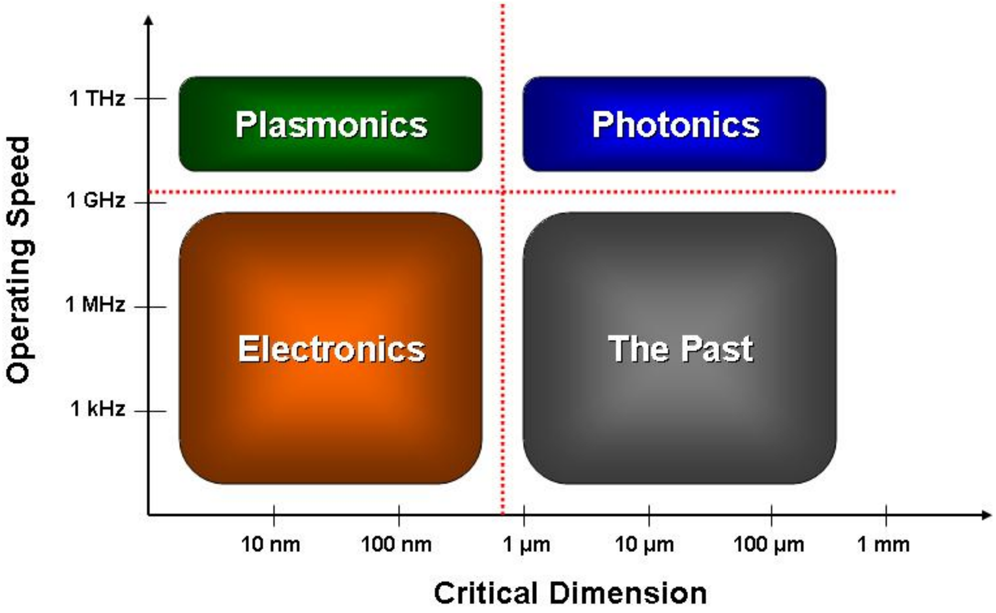

Figure 1 Comparison of the operating speeds and critical dimensions of different chip-scale device technologies.

This dissertation follows the style and format of Optics Express.

In the past devices were relatively slow and bulky. Thanks to the semiconductor industry, electronic devices have reached nano scale regime. Unfortunately, the processing speed of integrated circuits may be limited by interconnect delay time. On the other hand, photonics devices enable to processing of enormous data with high operating speed. At the same time, these devices are limited in their size by the fundamental law known as diffraction-limit. As a solution, plasmonics, which process photonic signals with nano scale circuit elements, can offer precisely both the size of electronics and the speed of photonics.

1.1.1 Plasmonic zone plate lens

The optical diffraction limit has been the dominant barrier to achieving higher optical resolution in the fields of microscopy, photolithography, and optical data storage. Spatial resolution is a measure of the ability to distinguish two separated point-like objects from a single object. The diffraction limit implies that optical resolution is ultimately limited by the wavelength of light. In order to explain diffraction limit, the concept of the point-spread function (PSF) is introduced. The PSF is a measure of the resolving power of an optical system. The narrower the PSF the better the resolution will be. As the name implies, the PSF defines the spread of a point source.[2]

Considering two point emitter separated by certain distance in the object plane, each point source will be identified with its PSF having some characteristic width. If we move the two emitters in the object plane closer and closer to each other, their PSF in the image plane will start to overlap and then reach a point where they become indistinguishable. If the maxima of two point-spread functions are separated by more than the characteristic width of one individual PSF, they can only be distinguished. This diffraction pattern is referred to as the Airy. Airy discs appear regardless of the geometry of the aperture and in the case of circular apertures (which is usually the case in imaging) show circular symmetry. The problem of diffraction limited imaging was realized by Ernst Abbe in 1873.[3] He stated that the distinguishable minimum distance in the image plane corresponds to the distance between the two point-spread functions for which the maximum of one PSF coincides with the first minimum of the second PSF.

Before the advent of near-field optics it has been believed that the diffraction limit imposes a hard boundary and that physical law strictly does not permit resolution significantly better than λ/2. One of applications for the near-field optics is a near-field microscopy. The central idea of near-field optical microscopy is to retain the spatial frequencies associated with evanescent waves thereby increasing the bandwidth of spatial frequencies.

Near-field optical probes such as laser-irradiated metal tips are the key components of near-field optical microscopy. The most common optical probes are uncoated fiber probes, aperture probes, pointed metal and semiconductor probes and nano-emitters. Until now, there have been limitations of traditional near-field optical microscopy: (1) practically zero working distance (< 20 nm) and an extremely small depth of field (< 20 nm), (2) Extremely long scan times for high resolution images or large specimen areas, and (3) very low transmission due to the aperture smaller than the incident wavelength. To address these issues, most recently, plasmonic zone plate lens are introduced as near-field optical probe. The key parameters and properties are summarized in Table 1.

Table 1 Comparison between conventional ZP and plasmonic ZP with respect to the key parameters.

Parameters	Conventional ZP	Plasmonic ZP
Total number of zones (required good focusing)	> 100	~ 30
Outmost zone width (determines resolution and NA)	Under diffraction limit	Beyond diffraction limit
Opaque zone materials, thickness, profile (focusing efficiency)	SiO_2, SiN (for Phase ZP)	Negative dielectric constant metals (e.g., Ag, Al, Au, Cu)
Focal length (working distance)	Several thousand μm	$\lambda < f < 10\lambda$

The objectives of this study are as follows: (1) to utilize the unique property such extraordinary optical transmission induced by surface plasmon polaritons, (2) to obtain a focused small spot size beyond diffraction limit through plasmonic zone plate lens, and (3) to improve working distance (WD) and depth of field (DOF).

1.1.2 Surface-enhanced Raman scattering-active substrate

Surface-Enhanced Raman Scattering (SERS) is a powerful analytical technique for chemical and biological detections. It has been reported that the SERS enhancements prominently depend on the size, shape, and assembly of metallic nanostructures. Many efforts have been made to utilize nano-structured metals as ultrasensitive SERS-active substrates by microstructure optimization. Until now, among various nano-structured SERS-active substrates, high SERS enhancement could be obtained for molecules localized in a small volume known as 'hot spot' within the inter-particle interstice. Generally, the optical field strength in the hot spots with the gaps of sub-10nm can reach ~ 10^{11} or more. However, this high enhancement, which exceeds that at isolated metal particles by ~ 6 orders of magnitude, falls off rapidly as the inter-particle gap increases.[4]

Theoretical and experimental studies indicate that the precise control of inter-particle gaps on a SERS-active substrate in the sub-10 nm regime is extremely difficult to be obtained by current nanofabrication processes. Although it enables to be fabricated by using the electron beam lithography (EBL), it is unfortunately very expensive to produce large area substrates, unless the technique is combined with a nanoimprint lithography (NIL).[5]

SERS-active substrate design and fabrication is now a fast developing branch of nanotechnology. Our work has basically focused on the development of SERS-active substrates with a high enhancement factor. Moreover, these substrates can generate a reproducible and uniform response and is simple to fabricate. Surface plasmons provide the opportunity to confine light to very small dimensions and the basic support comes from the physics of surface plasmons that deals with the properties of electromagnetic fields on the nanometric spatial scale and femto-second times. To obtain high SERS enhancement factor (EF) and simple fabrication, we introduce the concept of gap surface plasmon polaritons (GSPPs). By modulating the geometrical parameters such as particle shape, resonant length and gap thickness, strong GSPPs can be excited to the pre-determined location and thereby larger localized surface plasmon resonance and SERS EF can be achieved.

1.1.3 Infrared optical antenna

Infrared optical antenna can have mainly two applications such as infrared photodetector and surface enhanced infrared spectroscopy (SEIRS). Infrared photodetector is a photodetector that responds to infrared radiation. There have been two types of photodetector such as thermal-type and photon-type. In Table 2, we compare the advantages and disadvantages of thermal-type and photon-type photodetector, respectively. The main objective of this research is to find out the ways to improve photodetector's performance without cooling. Until now, there have been several ways to improve photodetector's performance without cooling such as interference enhanced photodetector and immersed Dember photodetector. Some limitations still exist at the ways: (1) the gain can be obtained only in narrow spectral regions, (2) less effective for oblique incidence, (3) mechanical matching problem, (4) severe transmission and reflection losses, and (5) total reflection. To address these problems, we introduce infrared dipole antenna enhanced by surface phonon polaritons.

Table 2 Advantages and disadvantages of thermal-type and photon-type photodetector, respectively.

	Thermal-type	Photon-type
Advantages	▪ Photo sensitivity independent of wavelength ▪ Not require cooling system ▪ Light, rugged, reliable and low cost	▪ Perfect signal-to-noise performance ▪ Very fast response time
Disadvantages	▪ Slow response time (ms order) ▪ Low detectivity at high frequency	▪ Selective wavelength dependence ▪ Cryogenic cooling is required ▪ Bulky, heavy, expensive and inconvenient to use

Another useful application for infrared optical antenna is to be used in surface enhanced infrared absorption (SERIA)-active substrate. Infrared spectroscopy is not only a powerful technique for the study of vibrational mode, but also very effective for the investigation of ultrathin film and well-ordered monolayers on metal surfaces. The most commonly used substrates for SERIA are metal island films, or metallic colloids which are the same active rough surface used in SERS-active substrate. Generally, for the IR applications, the SEIRA active nanostructures are fabricated on a reliable substrate that must be an infrared transparent material such as CaF_2, Si. Ge, ZnSe, and MgO for transmission geometry, or a reflecting substrate for the SEIRA experiment.[6] Notice that the dielectric properties of the substrate (i.e., refractive index) may play a crucial role in the observed spectra, particularly in the SEIRA experiment, where the observation of positive and negative absorption depends on the incident angle and the polarization of the incident radiation. Metal colloids can be employed as SEIRA-active nanostructures. Although aqueous metal colloids are one of the most common media employed in SERS due to the very low Raman scattering cross-sections of water, the extremely high infrared absorption of water prevents their straightforward application in infrared measurement. Ag and Au-island films are the most widely used SEIRA-active substrates, but SEIRA models predict enhancement on transition metals as strongly as them. More recently, the enhanced infrared absorption due to phonon resonance has been demonstrated for molecules adsorbed on the surfaces of silicon carbide and aluminum oxide nano-particles.[7]

If this substrate succeeds in placing molecules close enough to the metallic nano-structures for sensing the enhanced electromagnetic field, the infrared spectra would benefit from such enhancement. In order to enhance electromagnetic field, we introduce surface phonon polaritons (SPhPs) which is a counterpart of surface plasmon polarions (SPPs), so that main objective in this research is to achieve the enhanced electromagnetic field for both applications.

1.2 Organization of the Dissertation

This dissertation is an investigation for the interaction between materials, especially metals, and lights. This dissertation starts from the fact that the light can interact with matter such as reflection, refraction, scattering, interference, absorption, diffraction, and transmission. The researches presented in this dissertation falls into three different research topics which have different operating wavelengths. The first one is a

‘Plasmonic Zone Plate Lens’, which includes the novel methods of a small spot size beyond diffraction limit and the enhancement of transmission efficiency, where the incident light of 405 nm is chosen to excite surface plasmon polaritons. The second one is a ‘Surface-Enhanced Raman Scattering-active Substrate’, which includes a unconventional method for optical field confinement and enhancement, where the incident lights of 633 nm and 785 nm are chosen to excite gap surface plasmon polaritons. The last one is an ‘Infrared Dipole Antenna’, which includes the creative method for optical field confinement and enhancement, where the incident lights of 10.6 μm is chosen to excite surface phonon polaritons.

This dissertation is organized into seven chapters. In this chapter or Chapter I, the dissertation is inaugurated from the introduction of motivations and objectives of the proposed research topics.

In Chapter II, theoretical backgrounds to accomplish the proposed research topics are briefly summarized. In order to design plasmonic zone plate lens with high quality, basic theories such as near-field optics, metal optics, dispersion relation of surface plasmons, extraordinary optical transmission (EOT), and optics for conventional zone plate are discussed. In the section of SERS-active substrate, enhancement mechanisms of SERS such as electromagnetic mechanism and chemical mechanism are also included. In the section of infrared optical antenna, surface phonon polaritons which is a counterpart of surface plasmon polaritons are also provided. Finally, finite-difference time-domain (FDTD) method in the last section is presented.

In Chapter III, novel plasmonic zone plate lens to enable a small spot size beyond diffraction limit is introduced. By modulating the zone width of a plasmonic zone plate lens, consisting of metallic nanostructures covered with a dielectric layer, we demonstrate that a focused beam can be achieved with higher intensity and smaller spot size than the diffraction limited conventional zone plate lens.

In Chapter IV, we investigate the optical field enhancement by a metal/dielectric multilayered zone plate. By comparing multilayered zone plate lenses to a conventional monolayered zone plate lens, we present the effects associated the number of building blocks and different dielectric materials in the building block on the efficiency of the transmission.

In Chapter V, we study the SERS enhancement factor (EF) supported by GSPPs. By comparing SERS EF by the electromagnetic mechanism, we present SERS EFs predict enhancement of up to 10^{11} for equilateral triangular prism-shaped particles.

In Chapter VI, we investigate the field confinement properties of a gold dipole antenna formed on the SiC substrate. Due to the synergistic action of the dipole antenna and the resonant excitation of surface phonon polaritons, strong field enhancement in the gap region can be achieved.

Finally, Chapter VII discusses the summary for the proposed research topics. Optical property of highly conductive metals and their surface plasmon wave vectors and propagation lengths, simulation codes, optical property of polar materials and their effective refractive indices and propagation lengths are included in the appendix to help understanding of the achievement in the proposed research topics.

CHAPTER II

THEORETICAL REVIEW

Light interacts with matter in many different ways. The electromagnetic surface waves in the interface between a metal (a polar material) and a dielectric have been known as surface plasmons (surface phonons) or surface plasmon polaritons (surface phonon polaritons). These surface modes are built up via a coupling of coherent oscillations of the conduction electrons (lattice vibrations) at the metal (polar material) surface with interfacial electromagnetic fields and can be excited both via particle impact and photons provided that the conservation of energy and momentum is satisfied.

2.1 Plasmonic Zone Plate Lens

In order to design plasmonic zone plate lens that utilizes the unique property such as extraordinary optical transmission (EOT) induced by surface plasmon assisted multiple diffraction, the theoretical review deals with the physical origin such as near-field optics, metal optics and dispersion relation of surface plamon, EOT, and optics for conventional Fresnel zone plate.

2.1.1 Near field optics

Since conventional microscopy has numerous advantages such as noninvasive, reliable, fast, inexpensive, easy to use, it remains the most widespread imaging technique in use today. Nevertheless, the conventional optical microscopy has been suffered from optical diffraction limit. The best resolution at the visible range is several hundred nanometers, according to the limit derived by Ernst Abbe.[3] The spatial resolution of an optical system operating outside of the optical near-field can be given by the Rayleigh criterion [8]

$$d = \frac{0.61\lambda}{NA} \tag{2.1}$$

where d is the smallest distance distinguishable between two objects, λ is the incident wavelength and NA is the numerical aperture of the lens. In an effort to circumvent this limit, a method was first proposed in which light is leaked through an aperture much smaller than the incident wavelength in an opaque screen.[9] It is well-known that such an aperture has heavy diffraction and the power flux through such an aperture is evanescent. Therefore, in order to utilize this evanescent power flux, the aperture must be placed in the optical near-field region of the probe.[10] This method is called near-field scanning optical microscopy (NSOM) and was realized practically.[11, 12]

Figure 2 shows how to generate an optical near-field on a small sphere and a small aperture with conventionally propagating incident light. For the small sphere, since a << λ, the volume of this optical near-field is much smaller than the diffraction-limited value. However, it cannot be separated from the sphere because it is localized on sphere. For the small circular aperture with a sub-wavelength diameter, the size of optical near-field depends on the size of the aperture. Generally, the optical near-field is formed in the optical near-field region corresponding to the incident wavelength.

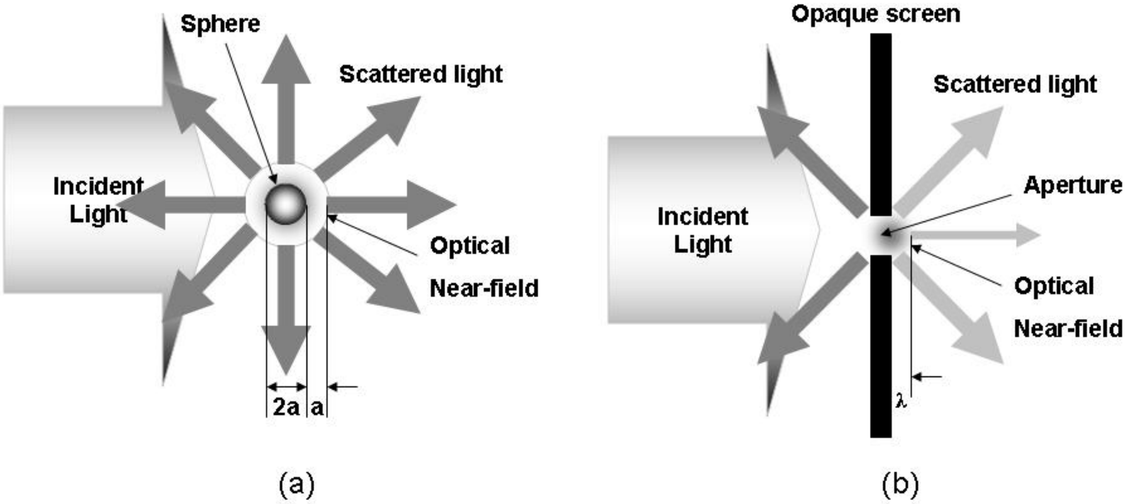

Figure 2 Schematic figures of an optical near-field: (a) on a small sphere and (b) on a small aperture.[13]

NSOM is a technique that affords capabilities of equal to or even better than 100 nm. The basic concept of NSOM is to combine scanning probe techniques and optical microscopy. However, it is noticeable that the transmission of light through the fiber tip is typically quite low. To improve the resolution and limited transmission, apertureless NSOM (a-NSOM) is introduced, in which the sharpen tip can support surface plasmons that leads to enhancement factors of the electric field of a few hundred times and also affords capability of breaking resolution limits on the order of tens-nanometer.

Figure 3 shows six common types of NSOM configuration. Because the evanescent light from the aperture has to be detected, an optical fibre probe must be positioned at a short distance from the sample surface. The major difference between aperture-type and apertureless-type NSOM is the feature of the probe. Aperture-type

NSOM has been used metal coated fibre optic probes as scanning tips but in apertureless-type NSOM , standard atomic force microscopy (AFM) tips can be used.

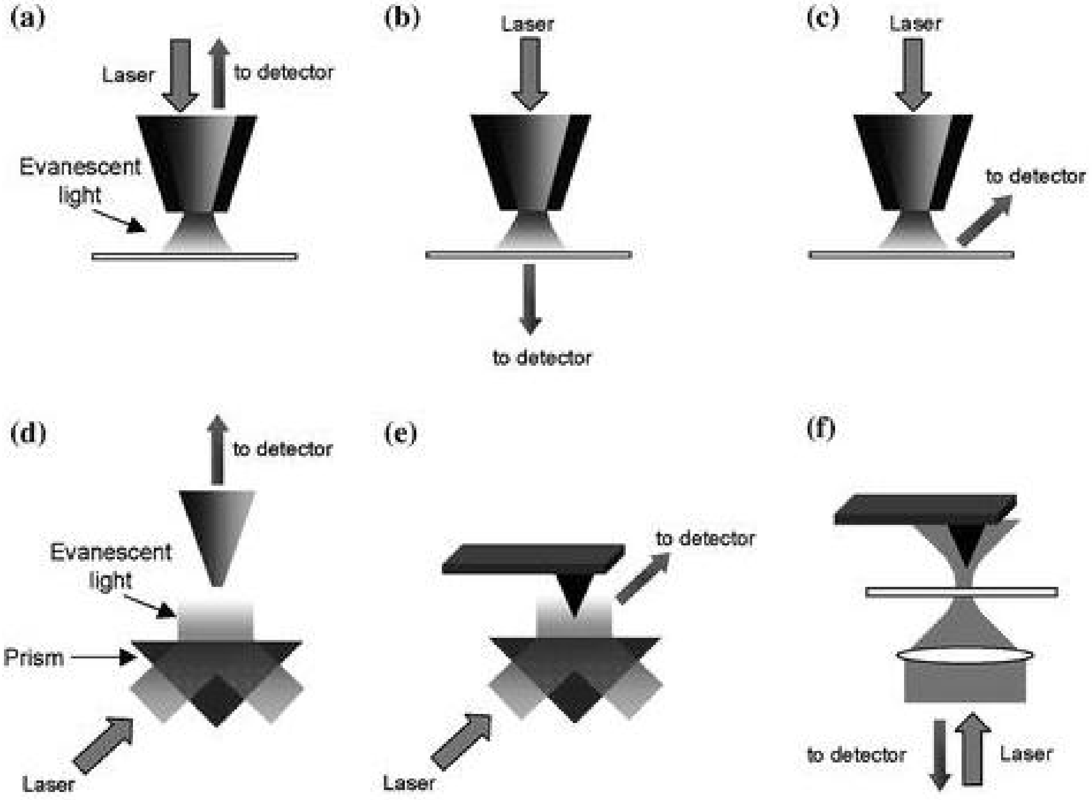

Figure 3 Schematic figures for NSOM configuration: (a) ~ (c) aperture-type and (d) ~ (f) apertureless-type.[8]

2.1.2 Optical properties of metals

Metals contain large densities of free electrons that originate from the valence electrons of the metal atoms. In 1900, P. Drude proposed the free electron model of metals. One simple way to introduce the Drude model is by using the Lorentz model for the atomic polarizability. This model describes the optical response of an electron in an atom or molecule, bound with a restoring force characterized by a resonant frequency ω_0. Therefore, the optical properties of metals can be explained by a plasma model, where the conduction electrons are not bound or “free”, and thus they experience zero restoring force (i.e., $\omega_0 \approx 0$). The Drude relative dielectric function of a metal can be obtained by taking $\omega_0 = 0$ in the Lorentz model, that is:[14]

$$\varepsilon(\omega) = 1 - \frac{ne^2}{m\varepsilon_0} \frac{1}{\omega^2 + i\gamma_0\omega} \tag{2.2}$$

where n is the number of free electrons per unit volume and m their mass. The damping term γ_0 corresponds to the collision rate of free electrons with the crystal or impurities. It is usually small compared to ω. In a solid the negative charges of the conduction electrons are balanced by an equal concentration of positive charge of the ion cores. The optical response of the positive ions in the crystal has so far been ignored. Therefore, the Drude model can be led to the expression for $\varepsilon(\omega)$, namely:

$$\varepsilon(\omega) = 1 - \frac{\omega_p^2}{\omega^2 + i\gamma_0\omega} \tag{2.3}$$

where plasma frequency ω_p can be defined as

$$\omega_p = \sqrt{\frac{ne^2}{m\varepsilon_0}}\,. \tag{2.4}$$

Plasma is a medium with equal concentration of positive and negative charges, of which at least one charge type is mobile. From plasma frequency, the corresponding wavelength can also be defined as $\lambda_p = 2\pi c/\omega_p$. Taking the real and imaginary parts of the expression of Drude model, we have:

$$\mathrm{Re}(\varepsilon(\omega)) = 1 - \frac{\omega_p^2}{\omega^2 + \gamma_0^2} \tag{2.5a}$$

and

$$\mathrm{Im}(\varepsilon(\omega)) = \frac{\omega_p^2 \gamma_0}{\omega(\omega^2 + \gamma_0^2)}. \tag{2.5b}$$

Since the damping term γ_0 is usually small compared to ω, we can have $\mathrm{Re}(\varepsilon(\omega)) < 0$ in the region where $\omega < \omega_p$ (wavelength longer than λ_p). Moreover, if ω is not too small, the absorption which is characterized by $\mathrm{Im}(\varepsilon(\omega))$ is also small in this region. These two conditions, $\mathrm{Re}(\varepsilon(\omega)) < 0$ and small $\mathrm{Im}(\varepsilon(\omega))$, can make possible the interesting optical effects such as plasmon resonances.

2.1.3 Dispersion relation of surface plasmon polaritons

The solutions of the Maxwell equations are divided in two waves such as s-polarized (TE) waves and p-polarized (TM) waves. The case when the electric field is parallel to the interface is described as the TE solution, while the case when the magnetic field is parallel to the interface is corresponded to the TM solution. Since SPP waves must propagate along the interface (i.e., along the x-axis in Figure 4), an E_z component perpendicular to the interface must exist, so that TE components are not satisfied for SPP propagation. Thus, no surface modes exist for TE polarization. SPPs only exist for TM polarization.[15]

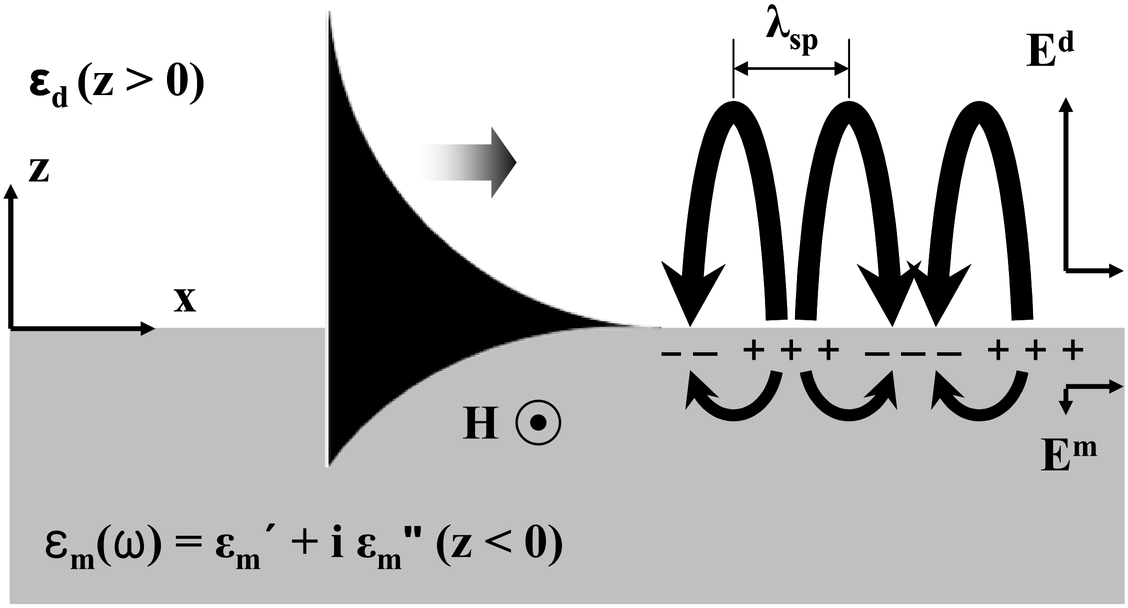

Figure 4 Schematic diagram of an intensity distribution and electromagnetic field components of a surface plasmon polariton supported by the interface between a metal and a dielectric.

Consider the interface (z = 0) between a metal with a complex dielectric constant $\varepsilon_m = \varepsilon_m' + i\varepsilon_m''$ and a positive dielectric constant ε_d as shown in Figure 4. A p-polarized (TM-wave) light propagates in the x-direction. There is no y dependence. Now these fields can be described in the dielectric and metal as follows:

for the dielectric medium, where z > 0,

$$H_d = (0, H_{yd}, 0)\exp i(k_{xd}x + k_{zd}z - \omega t) \tag{2.6a}$$

$$E_d = (E_{xd}, 0, E_{zd})\exp i(k_{xd}x + k_{zd}z - \omega t) \tag{2.6b}$$

with ω the light frequency and $k_d = (k_{xd},0,k_{zd})$ the wave number in the dielectric medium, for the metal, where z < 0,

$$H_m = \left(0, H_{ym}, 0\right) \exp i\left(k_{xm} x + k_{zm} z - \omega t\right) \tag{2.7a}$$

$$E_m = \left(E_{xm}, 0, E_{zm}\right) \exp i\left(k_{xm} x + k_{zm} z - \omega t\right). \tag{2.7b}$$

These fields have to fulfill Maxwell’s equations in medium i (i = metal or dielectric)

$$\nabla \cdot \varepsilon_i E = 0 \tag{2.8a}$$

$$\nabla \cdot H = 0 \tag{2.8b}$$

$$\nabla \times E = -\mu_0 \frac{\partial H}{\partial t} \tag{2.8c}$$

$$\nabla \times H = \varepsilon_i \frac{\partial E}{\partial t}. \tag{2.8d}$$

At the boundary,

$$E_{xm} = E_{xd} \tag{2.9a}$$

$$\varepsilon_m E_{zm} = \varepsilon_d E_{zd} \tag{2.9b}$$

$$H_{ym} = H_{yd}. \tag{2.9c}$$

From equations (2.9a) and (2.9c) follows the continuity of

$$k_{xm} = k_{xd} = k_x. \tag{2.10}$$

Equation (2.8d) gives

$$k_{zm} H_{ym} - \varepsilon_m E_{xm} \frac{\omega}{c} = 0 \tag{2.11a}$$

$$k_{zd} H_{yd} + \varepsilon_d E_{xd} \frac{\omega}{c} = 0 \tag{2.11b}$$

where $c = 1/\sqrt{\varepsilon_0 \mu_0}$ is the vacuum light speed.

Equation (2.11b) together with equations (2.9a) and (2.9c) yield

$$H_{ym} - H_{yd} = 0 \tag{2.12a}$$

$$\frac{k_{zm}}{\varepsilon_m} H_{ym} + \frac{k_{zd}}{\varepsilon_d} H_{yd} = 0\,. \tag{2.12b}$$

To obtain a solution, the determinant D_0 has to be zero

$$D_0 = \frac{k_{zm}}{\varepsilon_m} + \frac{k_{zd}}{\varepsilon_d} = 0\,. \tag{2.13}$$

This expression shows that the condition for the SPP existence is that it propagates at the interface of two media with opposite signs of the dielectric permittivity. This means that one of the two media must have a negative dielectric constant, as in the case of metals at optical frequencies. From the continuity condition for the in-plane wave numbers, we can get the total wave number in medium i as

$$k_x^2 + k_{zi}^2 = \varepsilon_i \left(\frac{\omega}{c}\right)^2 . \tag{2.14}$$

From Equation (2.13) together with Equation (2.14) follows[16]

$$k_{sp} = k_x = \sqrt{\varepsilon_i \left(\frac{\omega}{c}\right)^2 - k_{zi}^2} = \frac{\omega}{c} \sqrt{\frac{\varepsilon_m \varepsilon_d}{\varepsilon_m + \varepsilon_d}}\ . \tag{2.15}$$

Considering that in the dielectric the constant is real, and positive ($\varepsilon_d > 0$), and that in the metal the constant $\varepsilon_m = \varepsilon_m' + i\varepsilon_m''$ is complex, and $\varepsilon_m'' < |\varepsilon_m'|$, we have $k_{sp} = k_{sp}' + ik_{sp}''$. The surface plasmon wavelength is given by $\lambda_{sp} = 2\pi / k_{sp}'$. Thus we can get

$$\lambda_{sp} = \frac{2\pi c}{\omega} \sqrt{\frac{\varepsilon_d + \varepsilon_m'}{\varepsilon_d \varepsilon_m'}} \tag{2.16}$$

which is a very important relation because it demonstrates that for a metal with a negative dielectric constant in the visible and near-infrared region, with $|\varepsilon_m'| > \varepsilon_d$, we have $\lambda_{sp} < \lambda_0$ with $\lambda_0 = (2\pi c / \omega) / \sqrt{\varepsilon_d}$ the wavelength of the excitation, incident from the dielectric side for the metal/dielectric interface.

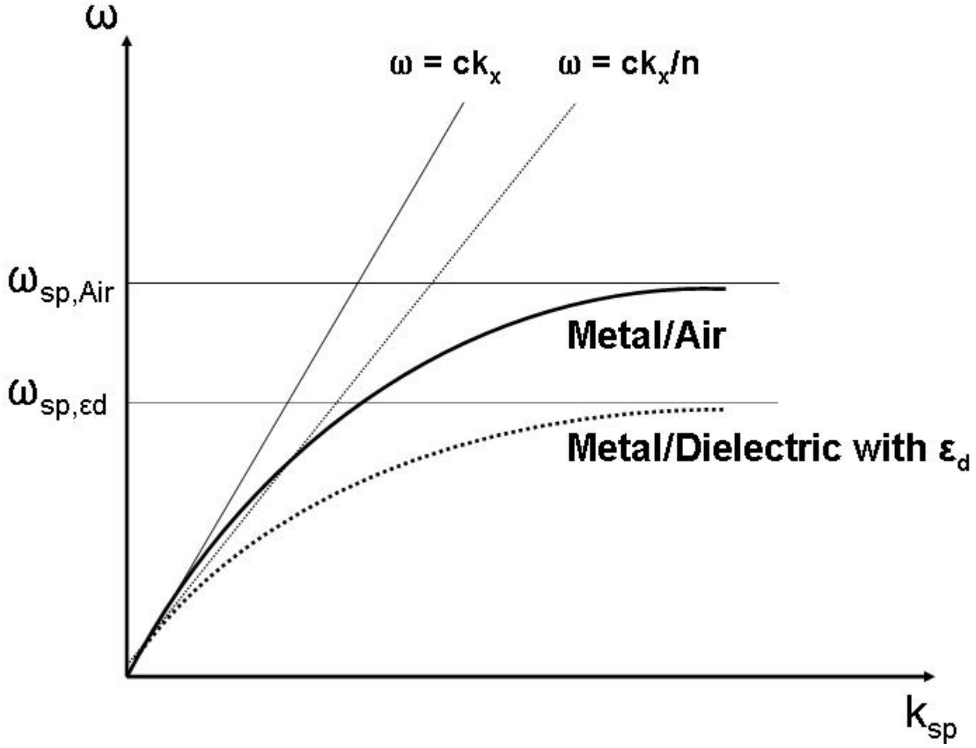

Figure 5 Dispersion relation of SPPs at the interface between a highly conductive metal and air and dielectric with ε_d, respectively.

Figure 5 shows dispersion relations for surface plasmon polaritons propagating at a flat interface between a highly conductive metal and air and dielectric with ε_d, respectively. It was calculated from using simple boundary condition of equation (2.15).

As can be seen, the dispersion relations of SPPs always lie to the right of the respective light line, approaching $\omega_{sp} = \omega_p / \sqrt{1+\varepsilon_d}$ for large wave vectors, the magnitude of the wave vector at ω_{sp} being limited by dissipation.

2.1.4 Extraordinary optical transmission (EOT)

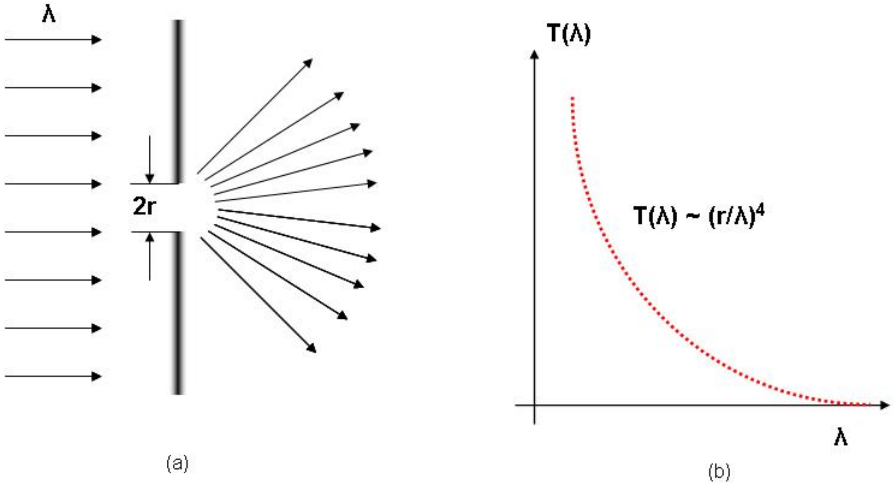

Figure 6 (a) Diffraction and (b) typical transmission through a subwavelength hole in an infinitely thin perfect metal film.

In 1944, Bethe studied the transmission of light through single subwavelength hole as shown in Figure 6. Diffraction and its transmission are characterized by both the radius of the hole and its depth. Assuming that the film is infinitely thin and that the metal is a perfect conductor, he derived the transmission efficiency (T(λ)) at the normal incidence.

$$T(\lambda) = \frac{64(kr)^4}{27\pi^2} \tag{2.17}$$

here, $k = 2\pi/\lambda$ is the free-space wave vector and r is the radius of the hole. Indeed, this transmission efficiency scaling with $(r/\lambda)^4$ is very small and it will be further decreased when considering the finite film thickness.

In 1998, Thomas Ebbessen and co-workers reported an extraordinary optical transmission through 2D arrays of subwavelength holes perforated in metallic films, in which 150 nm diameter holes with a regular periodicity between 600 and 1800 nm formed by a focused ion beam through 200 nm thick silver films on quartz substrate.[17] Figure 7 shows the transmission spectrum for normally incident light on a silver screen of thickness t = 200 nm perforated with an array of circular holes of diameter d = 150 nm arranged on a square lattice with period a_0 = 900 nm. The transmitted light was characterized by a narrow silver surface plasmon peak (at 326 nm) and a set of well-defined minima and maxima related to the geometry of the hole array.

They explained this phenomenon to surface plasmons (SPs), which are oscillations of surface charges at the metal interface and are excited when their momentum matches the momentum of the incident photon and the grating as follows:

$$k_{sp} = k_x \pm nG_x \pm mG_y = k_0 \sin\theta \pm (n+m)\frac{2\pi}{a_0} \tag{2.18}$$

where k_{sp} is the surface plasmon wave vector, $k_x = (2\pi/\lambda)\sin\theta$ is the component of the incident photon's wave vector in the plane of the grating and $G_x = G_y = 2\pi/a_0$ are the grating momentum wave vectors for a square array. For phase-matching via a square lattice, it can easily be shown by combining equation (2.18) and the typical form of the

SPP dispersion relation (equation 2.15) that for normally incident light the transmission maxima occur at wavelengths fulfilling the condition:[18]

$$\lambda_{spp}(n,m) = \frac{n_{spp} a_0}{\sqrt{n^2 + m^2}} \tag{2.19}$$

$n_{spp} = k_{sp}c/\omega$ is the effective refractive index of the SPP, which is for the single interface between a metal and a dielectric. Clearly, the array is actively involved in light transmission, most likely via resonance interactions with surface plasmons, localized in and around the holes in the metallic film.

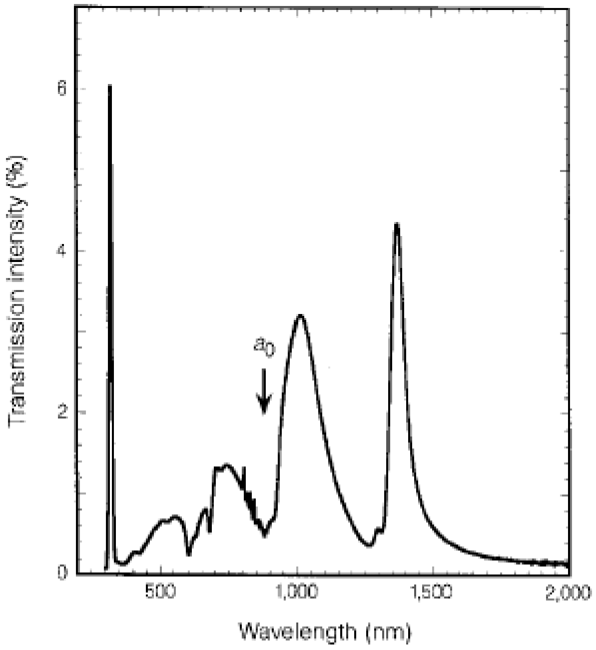

Figure 7 Zero-order transmission spectrum of an Ag array (lattice constant $a_0 = 0.9$ µm, diameter d = 150 nm, thickness t = 200 nm).[17]

2.1.5 Optical properties of Fresnel zone plate

A Fresnel zone plate (FZP) lens is an optical device that was designed to bring the incident light into focus through diffraction phenomena. To understand a zone plate, we need to take a diffraction grating into account. A diffraction grating is an optical component with a regular pattern, which diffracts light into several beams travelling in different direction.

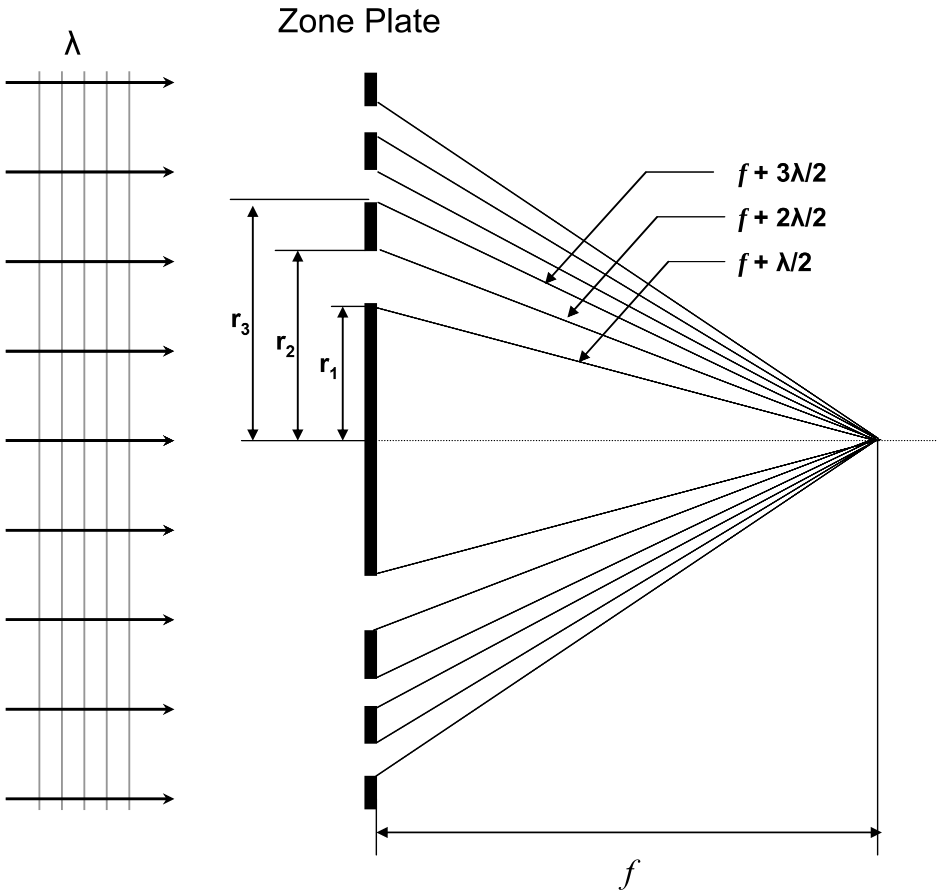

Figure 8 Zone plate diffractive focusing is illustrated for the first order.

As shown in Figure 8, we can see a plane wave incident on a zone plate from left side and focused into the focal point. We can derive the basic equation for the zone radii, using the notations in the figure. If we draws a right triangle with the focal length (*f*), the radius of any zone (r_n) and the hypotenuse of length ($f + n\lambda/2$), then the zone radii by the Pythagorean Theorem are given by

$$f^2 + r_n^2 = \left(f + \frac{n\lambda}{2} \right)^2 . \tag{2.20a}$$

After rearrangement,

$$r_n^2 = n\lambda f + \frac{n^2\lambda^2}{4} . \tag{2.20b}$$

The term $n^2\lambda^2/4$ can be neglected when $f >> \lambda$.

The expressions for the lens diameter D, focal length *f*, numerical aperture NA = $\sin\theta$, spatial resolution, and depth of focus can be obtained in terms of the wavelength λ, the total number N of zones (i.e., the sum of both opaque and transparent zones), and the outer zone width Δr.

We can begin from the case of $f >> n\,\lambda/2$

$$r_n^2 \cong n\lambda f . \tag{2.21a}$$

Now we write down for n → N as follows:

$$r_N^2 - r_{N-1}^2 = N\lambda f - (N-1)\lambda f = \lambda f . \tag{2.21b}$$

From the definition of Δr and since $\Delta r << r_N$

$$r_N^2 - (r_N - \Delta r)^2 \cong 2 r_N \Delta r \tag{2.21c}$$

$$2r_N \Delta r \cong \lambda f \ . \tag{2.21d}$$

Since $\lambda f \cong r_N^2 / N$ and $D = 2r_N$

$$D \cong 4N\Delta r \ . \tag{2.22}$$

The equation related to the focal length can then be obtained:

$$f \cong \frac{4N(\Delta r)^2}{\lambda} \ . \tag{2.23}$$

This is a very important relationship for the design of zone plate microscope lenses in that it shows that the focal length scales directly with the number of zones, with the square of the outer zone width, and inversely with the wavelength, thus introducing a strong chromatic effect. Another equation related to the numerical aperture of a zone plate lens is given by NA = $\sin\theta = r_N/f = D/2f$,

$$NA \cong \frac{\lambda}{2\Delta r} \ . \tag{2.24}$$

One measure of the resolution of a lens is the minimum discernible separation of two mutually incoherent point sources. This in turn depends on the so-called point-spread function (PSF) of the lens, that is, the image plane intensity distribution due to a distant point source. For an ideal lens, the PSF is an Airy pattern, whose lateral spread depends on both wavelength and lens numerical aperture. In general, Rayleigh resolution criterion is given by

$$Rayleigh \quad res. = \frac{0.610\lambda}{NA} = 1.22\Delta r \ . \tag{2.25}$$

The other important parameter, the depth of focus of a lens or system, is the permitted displacement, away from the focal or image plane, for which the intensity on axis is diminished by some permissible small amount, or image resolution is only slightly degraded. The depth of focus for the zone plate lens (i.e., the intensity decrease of only 20 %) can be expressed by

$$DOF = \pm \frac{1}{2} \frac{\lambda}{(NA)^2} = \pm \frac{2(\Delta r)^2}{\lambda} . \qquad (2.26)$$

The depth of focus is inversely proportional to the square of the numerical aperture. If the smallest focal spot (i.e., the largest NA) is potentially achieved, the depth of focus will be very short.

2.2 Surface-Enhanced Raman Scattering (SERS) and Its Substrate

The Raman scattering describes the inelastic scattering process between a photon and a molecule, mediated by a fundamental vibrational or rotational mode of the matter. Since the first reports on surface-enhanced Raman signals in the 1970s, the phenomenon of SERS is now well established. Since then, SERS has been proven to be a powerful analytical tool for analytical chemistry, life science, medical science, and the characterization of chemical agents. Although the exact enhancement mechanism of SERS is still on controversy, it is generally accepted that two enhancement mechanisms are operative: a) electromagnetic enhancement associated with a strong localized electric field due to the surface plasmon resonance (SPR) of metallic nanostructures and b) chemical enhancement that arises from dynamical charge-transfer between the energy levels of the molecule and Fermi levels of the metals.[19]

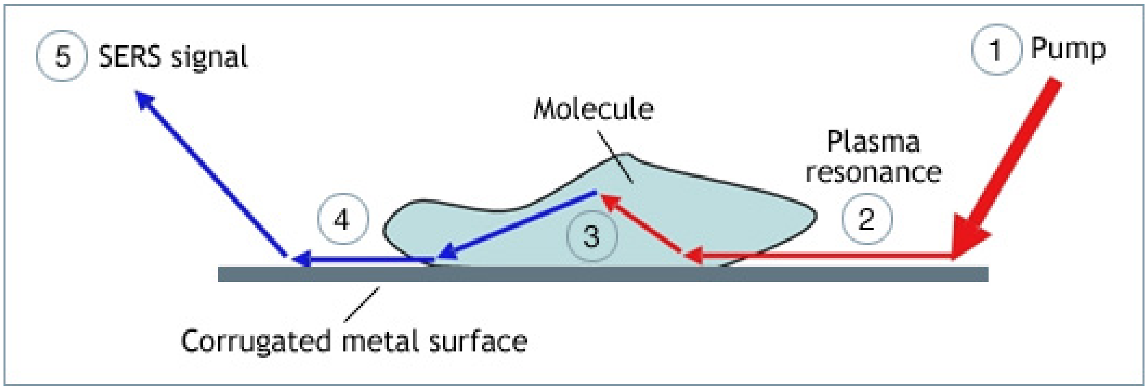

Figure 9 Schematic diagram for SERS process steps.[20]

The enhanced Raman scattering interaction between the incident laser light and the molecule can be mediated by the resonance effect of surface plasmons. In order to help the understanding of SERS mechanism, SERS process steps are presented in Figure 9. SERS process steps are as follows: (1) laser light incident on the metal substrate, (2) excitation of surface plasmons, (3) light scattered by the molecule, Raman scattered light (4) transferred back to surface plasmons and (5) scattered in air. From SERS process steps, surface plasmons can assist in coupling light into molecules close to the surface and couple out photons into specific directions. It is this enhanced coupling both into and out of the molecule that enhance the Raman signal.

2.2.1 Electromagnetic enhancement of SERS

The electromagnetic field enhancement of the noble metal is considered to mainly come from a geometrically defined SPR at metallic nanostructures. Among the metallic nanostructures, metallic nano-particles (NPs) are frequently used because they can support strong SPRs in visible wavelength range. At these wavelengths, metals that possess a negative real and small positive imaginary dielectric constant are capable of exhibiting a SPR. In general, light interacts with particles much smaller than the incident wavelength as shown in Figure 10, which leads to a plasmon that oscillates locally around the nano-particle with a frequency known as the localized surface plasmon (LSP) resonance.

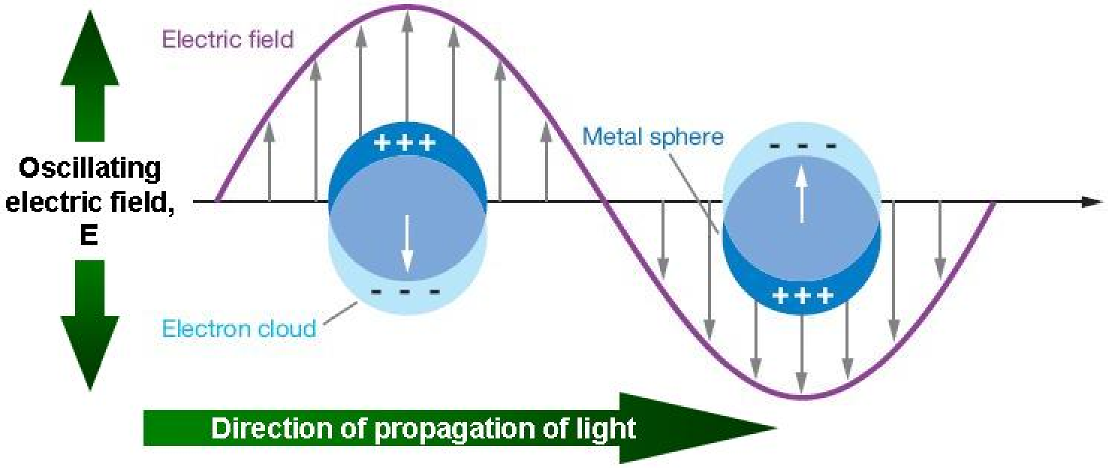

Figure 10 Schematic diagram for a localized surface plasmon.[21]

In other words, the conduction electrons inside the particle will all move in phase upon plane wave excitation. It leads to the build-up of polarization charges on the particle surface that will act as a restoring force, allowing a resonance to occur a specific frequency. A resonantly enhanced field builds up inside the NPs, which in the small particle limit is homogeneous throughout its volume, while a dipolar field is produced outside. This results in strong light scattering, the appearance of intense surface plasmon absorption bands, and the enhancement of the near-field in the immediate vicinity of the particle surface.[22] The LSP resonance depends on the particle material, size, and geometry and local dielectric environment.

Electromagnetic mechanism of SERS predicts that the SERS electromagnetic enhancement factor (EF) is given by[23]

$$EF = [E(\omega)]^2 [E(\omega')]^2 \tag{2.27}$$

Where ω is the incident laser frequency, ω′ is the Stokes-shifted frequency of the Raman scattered photon, and E is the amount of enhanced local electric field. The maximum enhancement of the normal Raman cross-section occurs when both the incident and Stokes scattered fields are equally enhanced.

In conventional SERS, E is averaged over the surface area of the particles where molecules can be adsorbed to generate observed enhancement factor <E>, while in single molecule SERS it is the maximum enhancement E_{max} that is of interest. Note that E_{max} can be orders of magnitude larger than <E>, so the distinction between these two enhancement estimates is important. Another point is that this $[E(\omega)]^2[E(\omega')]^2$ factors is often approximated by $EF = |E(\omega)|^4$ as the plasmon resonance peaks are broad enough that the change in $|E(\omega)|^2$ between the incident and Stokes-shifted frequency is small (typically less than a factor of three).[4]

2.2.2 Chemical enhancement of SERS

It has been generally accepted that there is a second enhancement mechanism which operates independently of the electromagnetic mechanism. The dynamical charge-transfer enhancement is well-known mechanism as a resonance-like SERS enhancement.

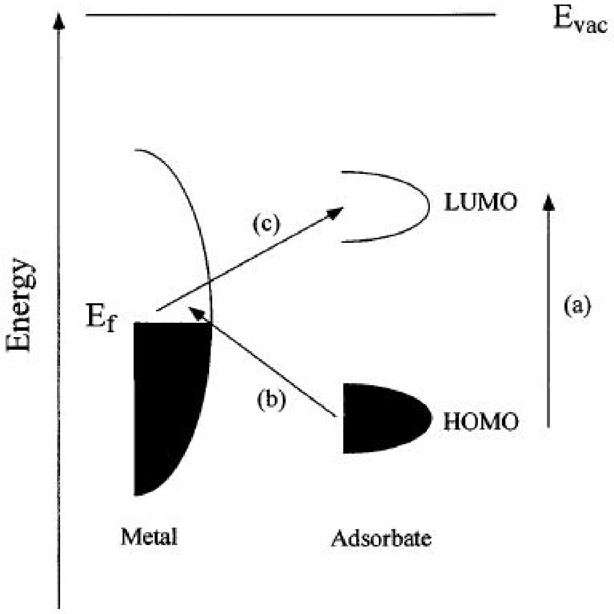

Figure 11 Energy level diagram for a molecule absorbed on a metal surface showing also possible resonance Raman processes involving molecular states (path (a)) and molecular and metallic states (paths (b), (c)).[24]

This dynamical charge-transfer can be described by the following four steps[25]: (a) photon annihilation, excitation of an electron into a hot-electron state, (b) transfer of the hot electron into the LUMO of the molecule, (c) transfer of the hot electron from the LUMO (with changed normal coordinates of some internal molecular vibrations) bask to the metal and (d) return of the electron to its initial state and Stokes photon creation.

Figure 11 shows a typical energy level diagram for a molecule absorbed on a metal surface, where the energies of the highest occupied molecular orbital (HOMO) and the lowest unoccupied molecular orbital (LUMO) are approximately symmetric relative to the Fermi level of the metal, together with possible resonant Raman processes involving molecular states (path (a)) and molecular and metallic states (paths (b), (c)). In general, the chemical SERS enhancement factor is considered to contribute enhancement factors on the order of $10 \sim 10^2$.

2.3 Infrared Optical Antennas

Although SERS is the best known and the most studied among the surface-enhanced properties, several other molecular properties are affected by the presence of a curved metal specimen. SEIRA is a surface-sensitive spectroscopic technique that has a great advantage of profiting from a vast body of the vibrational data, collected, understood and classified in libraries for all three state of matter. The enhanced electromagnetic field by resonance effect aids to surface-enhanced absorption that enable to more sensitive detection. In this section, surface phonon polaritons which is particularly amenable to frequencies in the mid-infrared are briefly presented on the physical origin of electromagnetic field confinement and enhancement.

2.3.1 Surface phonon polaritons (SPhPs)

Phonons are vibrations of the atoms in a crystal lattice, and have resonant frequencies in the infrared spectral region. This contrasts with the optical properties of bound electrons, which occur at visible and ultraviolet frequencies. When the atoms are displaced from their equilibrium positions, they experience restoring forces, and vibrate at characteristic frequencies. These vibrational frequencies are determined by the phonon modes of the crystal. The modes interact directly with light.[26]

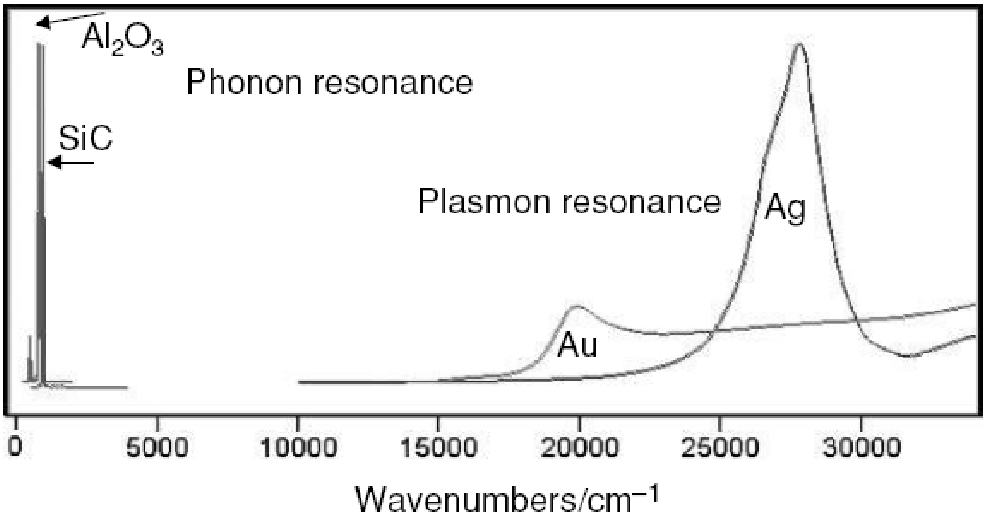

Figure 12 Phonon resonances of SiC and Al_2O_3 and surface plasmons in metal nano-particles.[27]

At low frequencies (i.e., infrared frequency), a strong localization of the electromagnetic field with metallic structures can only be achieved for corrugated surfaces in the forms of designer plasmons.[18] Surface phonon polaritons arise due to the coupling of the electromagnetic field to lattice vibrations of polar materials at infrared frequencies. The physics of this excitation is conceptually analogous to that of both propagation and localization of surface plasmons, and formulas derived in excitation of surface plasmon polaritons.

In Figure 12, the location of the resonance for a spherical particle of 40 nm diameter of Ag, Au, SiC and Al_2O_3 are depicted as function of wave numbers from the visible to the mid-infrared region. This suggests that surface phonon polaritons at mid-infrared frequencies is a promising route to sub-wavelength energy localization, in the same way as plasmonics at visible and near-infrared frequencies, with potentially smaller energy attenuation in waveguides and larger field enhancement in resonator structure. Recently, some development in the near-field may renew the interest in SEIRA using phonons rather than photon excitation. The origin of SEIRA is attributed to electromagnetic and chemical contributions responsible for the observed infrared enhancement. In other words, the mechanism of SEIRA is interpreted as being the result of the enhanced optical fields at the surface of the particles when illuminated at the surface phonon resonance frequencies. This phonon resonance effect is in analogue to plasmon resonance that is the basis of surface-enhanced absorption and surface-enhanced Raman scattering in metals.

2.4 Finite-difference Time-domain (FDTD)

The finite-difference time-domain method solves directly Maxwell's time-dependent curl equations

$$\nabla \times E = -\mu_0 \frac{\partial H}{\partial t}, \tag{2.28a}$$

$$\nabla \times H = \varepsilon_0 \varepsilon_r \frac{\partial E}{\partial t}, \qquad (2.28b)$$

so that both space and time have to be discretized. The standard FDTD is based on the Yee algorithm.[28]

In this dissertation, TEMPEST (version 6.0) – 'Time-domain Electromagnetic Massively Parallel Evaluation of Scattering from Topography' developed by Electronic Research Laboratory at University of California, Berkeley has been used to solve Maxwell's equations using a time-domain finite-difference algorithm, where the electric and magnetic field nodes are spatially and temporally staggered over a three-dimensional topography of interest.[29] TEMPEST analyzes topography information from an input file which can be checked for correctness. The input geometry is then simulated until the electromagnetic field reaches steady-state or, in the case of non-convergence; the simulation domain is excited for a user chosen number of wave cycles. Information on the simulation parameters is written to an output file. Topography and field data are written to files where they can be analyzed.

CHAPTER III

OPTICAL FOCUSING BEYOND DIFFRACTION LIMIT OF PLASMONIC ZONE PLATE LENS*

3.1 Introduction

Fresnel Zone Plate (FZP) lens has been employed in numerous applications ranging from lithography to confocal microscopy. In some wavelengths, such as x-rays, FZP is the only viable high-resolution imaging optics. The focusing properties of a Fresnel zone plate lens can be understood by considering the first order diffraction from a circular grating with the zonal periods adjusted so that at increasing radius from the optic axis the periods become shorter, and the diffraction angle becomes larger, thus permitting a real first order focus, as shown in Figure 13.

In the field of maskless lithography, Zone Plate Array Lithography (ZPAL) was proposed by Smith in 1996 whose resolution was estimated to be 25 nm using $\lambda = 4.5$ nm.[30] Sequent works have been successfully carried out and demonstrated in the UV region.[31] Immersion ZPAL (iZPAL) was further developed to improve resolution.[32] The same configuration can also work as a confocal microscope.

---

* Reprinted with permission from “Optical focusing of plasmonic Fresnel zone plate-based metallic structure covered with a dielectric layer” by Hyun Chul Kim, Hyungduk Ko, and Mosong Cheng, J. Vac. Sci. Technol., 26, 2197 (2008). Copyright by American Vacuum Society. (www.aip.org)

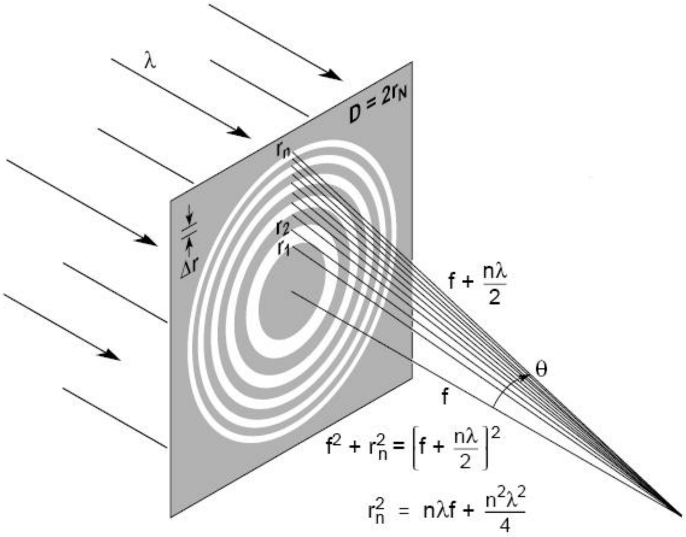

Figure 13 A Fresnel zone plate lens with plane wave illumination, showing only the convergent (+1st) order of diffraction.[33]

Although these techniques have demonstrated very promising capabilities, the fact that FZP is limited by diffraction somehow hinders their extension to higher resolution imaging.[34] Also based on scanning approach, Near-field Scanning Optical Microscopy (NSOM) uses a localized field to scan an object to generate a high resolution image. In general, the better the confinement of the source field is, the better the resolution of the images will be.[2] Until now, the majority of NSOM uses a nanometer scale circular or square shaped aperture to generate the localized field, which suffers from extremely low light transmission and poor contrast known as Bethe's limit.[35] A promising approach to overcome Bethe's limit is Extraordinary Optical Transmission (EOT), which occurs in a metallic film perforated with subwavelength hole arrays or slits, or a hole surrounded by corrugations, dimples or grooves.[17, 36-38]

It is believed that the process of EOT is excitation of surface plasmons (SPs) on both surfaces of the metallic film, coupling SPs into aperture, and conversion back into near-field at the exit side of the aperture. Recent works also showed the possibility of focusing surface plasmon polaritons (SPPs) on a planar metal film by guiding SPPs to the focal point of circular, elliptical and micro zone plate apertures.[39-42] Although EOT or SPP focusing can enhance the NSOM signal, the working distance (WD), namely the distance between the probe and the sample, is still a fraction of wavelength. Thus the scanning speed is severely limited. And in many cases, such as biological imaging or lithography, the interior of a sample can not be imaged.

3.2 Design for Plasmonic Zone Plate Lens

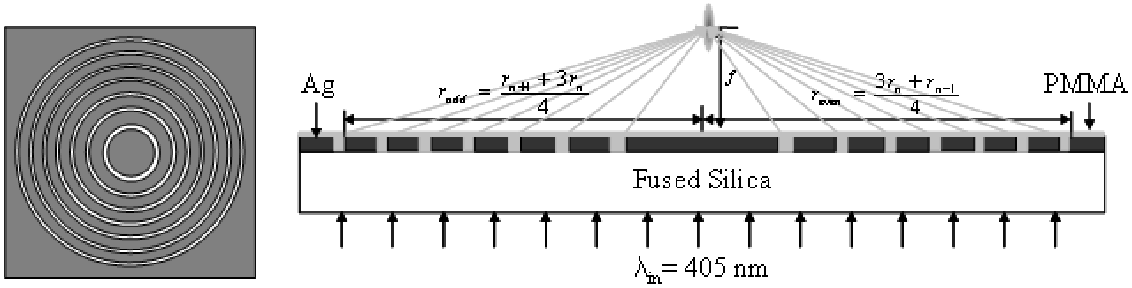

(a) (b)

Figure 14 Schematic diagrams for proposed design: (a) Top-down and (b) cross-section views of a MDA-PFZP design (drawings are not to scale).

To address the disadvantages of the devices mentioned above, we propose a modified FZP structure. As illustrated by Figure 14, this structure consists of a set of concentric ring apertures in a silver film deposited on a fused silica substrate. A dielectric film, e.g., PMMA, is spin-coated on the metal film so the apertures are filled with the dielectric. We name the device Metallic-Dielectric-Air (MDA) structured Plasmonic FZP (MDA-PFZP). It has several interesting characteristics. First, each ring aperture, corresponding to a transparent zone in a FZP, can be considered as a metal-dielectric-metal waveguide in the direction of light traveling. With SPP resonance, this waveguide significantly enhances the light transmission. Thus the modified FZP allows for higher diffraction efficiency. Second, each ring has half width of a transparent zone of a FZP, which means the wavelets transmitting through these rings are more “in-phase”, resulting in smaller focused spot. By doing so, the diffraction efficiency is reduced because of less transparent area, but it is compensated by the waveguide effect just discussed. Third, the focal length of the modified FZP is reduced to below 5λ, e.g., 0.5 μm, whereas conventional FZP typically has a focal length of tens to hundreds of μm. Note that the focal length is measured from the top of the metal surface to the axial maximum. To achieve a certain NA, a FZP with smaller focal length will have smaller diameter. Thus our MDA-PFZP will have smaller footprint than conventional FZP, helping increase packing density if many lenses need to be integrated on a chip.

The modified FZP device achieves a focused spot modestly smaller than diffraction limit. It is comparable to apodization technique, which uses alternating ring apertures in a pupil filter to reduce the size of the main lobe. Meanwhile, our proposed

FZP device takes advantage of the SPP waveguide effects to allow for light transmission higher than a FZP. In apodization or NSOM, on the contrary, the light transmission is fairly poor.

In a conventional FZP, the radius of the *n*-th zone is given by the Fresnel Zone Plate formula,[33]

$$r_n^2 = n\lambda f + \frac{n^2\lambda^2}{4} \tag{3.1}$$

where f is the focal length, and n an integer starting from 1. The Rayleigh resolution of a conventional FZP is given by $0.61\lambda/\mathrm{NA} = 1.22\Delta r$, where Δr is the outmost zone width.

To reduce the focused spot size, each zone width in the proposed MDA-PFZP is reduced and the device is covered by a dielectric layer. Meanwhile, the focal length of a MDA-PFZP is reduced to around $\lambda < f < 5\lambda$, i.e., in the mid-field region, partly because it has smaller footprint, considering that r_n decreases with f decreasing. For instance, at $f = 0.5$ μm and $\lambda = 405$ nm, the minimum saturation of the outmost zone width is obtained when the number of zones reaches 12, i.e., $N_{zone} = 12$, which means the FZP needs at least 12 transparent rings to achieve the highest resolution. Here a minimum saturation means that the outmost zone width approaches a constant even if N_{zone} is further increased. Note that when n is large, $r_n \sim n\lambda/2$. So the outmost zone width, given by $r_{n+1} - r_n$, tends to $\lambda/2$ when N_{zone} is large enough.

As in conventional optical systems, the light field distribution on the image plane is described by its point-spread-function (PSF) and the spot size can be evaluated by full width at half maximum (FWHM) and then translated into effective numerical aperture (NA_{eff}). The modeling and analysis throughout this article assume the illumination wavelength as 405 nm, which is close to the 400 nm wavelength used by ZPAL.[31]

3.3 Choice of Metal

Before starting main research, the reason why silver is chosen as the best metal to excite and propagate surface plasmon polaritons is introduced. In general, the choice of metal depends on the wavelength to be used because the dielectric constants of metals

Table 3 Comparison of SP dispersion relation both in propagation direction ($k_{sp,x}$) and in the perpendicular direction ($k_{z,d}$ and $k_{z,m}$) of the metal/air (ε_d = 1.0) interface for the selected metals at incident wavelength of 405 nm.

Metals	ε_m[a]	$k_{sp,x}$			$k_{z,d}$			$k_{z,m}$		
		|Re|	|Im|	$L_{sp,x}$ (μm)	|Re|	|Im|	$L_{z,d}$ (μm)	|Re|	|Im|	$L_{z,m}$ (μm)
Ti	-2.22+i6.67	15.76	0.07	0.45	3.82	0.30	0.11	22.04	2.29	0.014
Cr	-4.12+i11.65	15.69	0.04	0.81	2.72	0.23	0.14	30.09	2.98	0.011
Cu	-3.18+i5.16	16.09	0.08	0.41	3.62	0.35	0.09	16.67	2.33	0.014
Ag	-4.01+i0.70	17.80	0.03	1.01	1.00	0.57	0.06	2.09	2.31	0.014
Al	-23.96+i4.92	15.83	0.00	7.37	0.34	0.21	0.16	7.58	5.02	0.006
W	5.57+i16.36	15.35	0.03	1.21	3.06	0.13	0.24	50.90	2.49	0.013
Au	-1.08+i6.49	15.57	0.08	0.42	4.28	0.28	0.12	23.49	2.09	0.015

[a] Optical data are adapted from *'Handbook of Optical Constants of Solids'* edited by E. D. Palik

are wavelength dependent. Ideally speaking, the dielectric constant of the metal should have high absolute value for the real part and a small imaginary part that determines the absorption into the metal. This combination gives rise to high SP fields at the surface and minimizes the propagation losses.[43]

We compared the SP dispersion relation for the selected noble metals at the metal/air interface in Table 3. The SP dispersion relation for the wave in the propagation direction is given by

$$k_{sp,x} = \frac{\omega}{c}\sqrt{\frac{\varepsilon_m \varepsilon_d}{\varepsilon_m + \varepsilon_d}}, \tag{3.2}$$

with ε_m and ε_d the dielectric constants of both media at the interface. The wave vector in the direction perpendicular to the interface is given by

$$k_z = \frac{\omega}{c}\sqrt{\frac{\varepsilon_{m,d}^2}{\varepsilon_m + \varepsilon_d}}. \tag{3.3}$$

Moreover, propagation length of SPPs is provided by the imaginary part of the SP dispersion relation, the distance where the intensity falls to 1/*e* of its initial value is calculated by $L_{sp,x} = (2\mathrm{Im}(k_{sp,x}))^{-1}$. For perpendicular direction, the attenuation of intensity can also be calculated by identical equation (i.e., $L_z = (2\mathrm{Im}(k_z))^{-1}$).

As reported from many other literatures, silver is ideally suited to obtain high transmission through the excitation and propagation of high surface plasmon. Note that aluminum has the smallest imaginary part, and thus its propagation length ($L_{sp,x}$) of excited SPs is the longest, which can has useful applications such as waveguides.

Since proposed plasmonic device covered with PMMA is used, we also compared the SP dispersion relation for the selected noble metals at the metal/PMMA interface in Table 4. With approaching the resonant surface plasmon frequency (i.e., $\varepsilon_d = |\mathrm{Re}(\varepsilon_m)|$), the momentum value of surface plamon is increased but simultaneously the imaginary part of the SP wave vector increases rapidly and thereby the propagation length of SPPs decreases.

Table 4 Comparison of SP dispersion relation both in propagation direction ($k_{sp,x}$) and in the perpendicular direction ($k_{z,d}$ and $k_{z,m}$) of the metal/PMMA (ε_d = 2.34) interface for the selected metals at incident wavelength of 405 nm.

Metals	ε_m	$k_{sp,x}$			$k_{z,d}$			$k_{z,m}$		
		|Re|	|Im|	$L_{sp,x}$ (μm)	|Re|	|Im|	$L_{z,d}$ (μm)	|Re|	|Im|	$L_{z,m}$ (μm)
Ti	-2.22+i6.67	24.01	0.27	0.12	10.03	0.64	0.05	18.55	2.44	0.013
Cr	-4.12+i11.65	24.19	0.15	0.22	6.89	0.52	0.06	27.82	3.12	0.010
Cu	-3.18+i5.16	25.07	0.32	0.10	10.28	0.78	0.04	12.69	2.52	0.013
Ag	-4.01+i0.70	35.37	0.26	0.13	5.29	1.71	0.02	1.20	3.02	0.011
Al	-23.96+i4.92	24.92	0.02	1.89	0.86	0.49	0.07	7.30	5.17	0.006
W	5.57+i16.36	23.10	0.09	0.35	7.21	0.29	0.11	48.81	2.56	0.013
Au	-1.08+i6.49	23.30	0.27	0.12	10.90	0.58	0.06	19.88	2.21	0.015

Based on Table 3, silver and aluminum where silver has the highest $\mathrm{Re}(k_{sp,x})$ value and aluminum has the smallest $\mathrm{Im}(k_{sp,x})$ value can be selected to obtain high transmission through the excitation and propagation. Figure 15(a) and (b) show the distribution of the transmitted field intensity on the xz-plane for the zone plates of silver

(Ag-ZP) and aluminum (Al-ZP), respectively. The dimensions of the zone plate are obtained from the classical equation used in designing conventional Fresnel zone plate. The design parameters such as focal length $f = 1\mu$m and incident wavelength $\lambda = 405$ nm are chosen, where a zone plate has center being opaque. In addition, the thickness of metal layer being $t_m = 100$ nm and dielectric constants of metal layer being $\varepsilon_{Ag} = -4.01+i0.70$ and $\varepsilon_{Al} = -23.96+i4.92$, respectively, are mainly used.

In Figure 15(c), it is clear that at the focal point, the field enhancement of Ag-ZP is estimated to be about 5.3 times larger than that of Al-ZP. At the same time, full width at half maximum (FWHM) of Ag-ZP is much smaller than that of Al-ZP. It is well agreed to reporting from many other literatures that silver is ideally suited to obtain high transmission through the excitation and propagation of high surface plasmon. As a result, we choose silver as the simulation metal in our proposed device. In order to allow further well understanding for this research, optical properties, surface plasmon wave vectors and their propagation length for various metals are included in the Appendixes A and B.

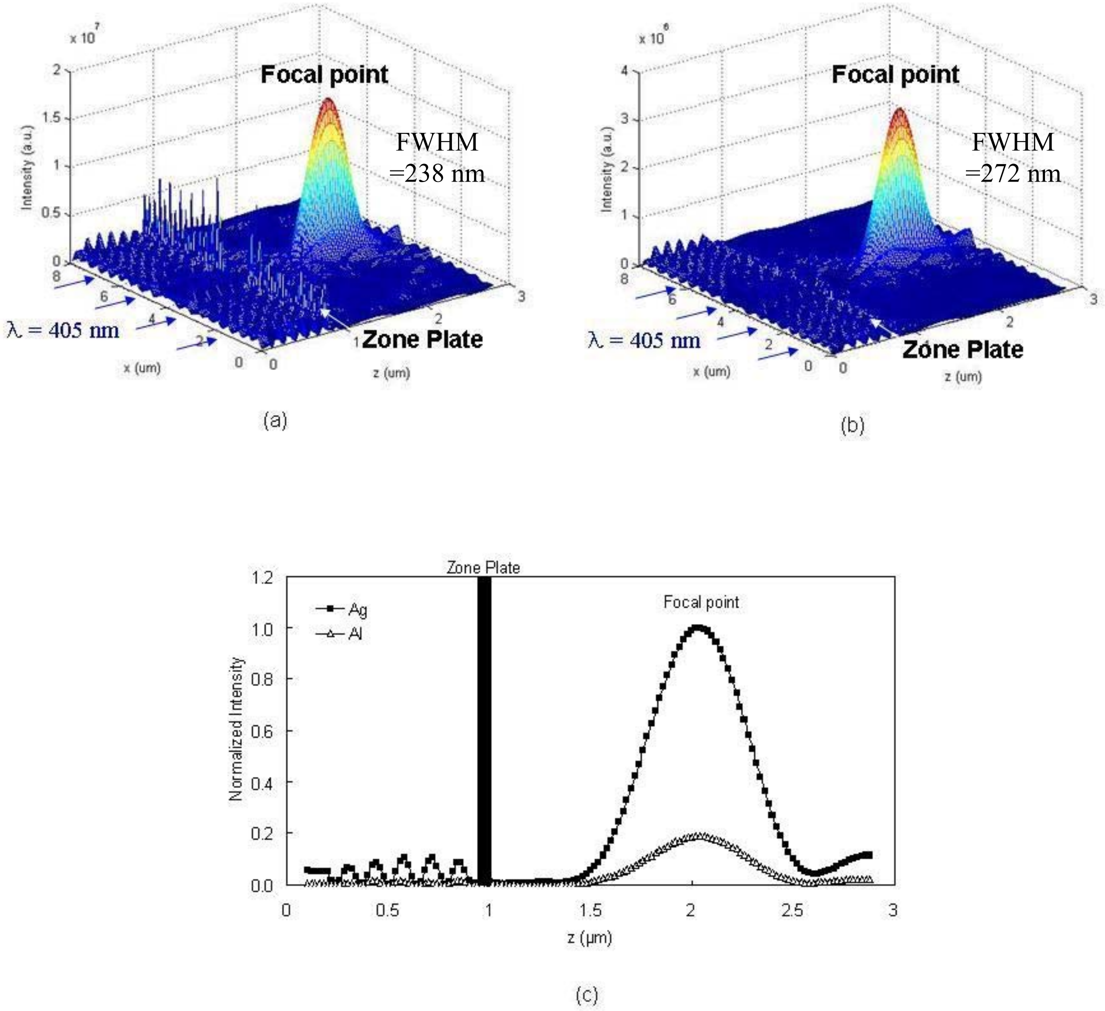

(a)

(b)

(c)

Figure 15 Field distribution of the transmitted field in the xz plane: (a) Ag-ZP and (b) Al-ZP, and (c) comparison of the normalized intensity for the Ag-ZP and Al–ZP, respectively, along z direction.

3.4 Modeling and Simulation Methodology

There are two types of FZP, Amplitude Zone Plate (AZP) in which either the odd or even zones are opaque, and Phase Zone Plate (PZP) in which the odd and even zones have different refractive indices or thicknesses to induce an alternating phase change. The main advantage of PZP is its higher diffraction efficiency. The maximum diffraction efficiencies of AZPs and PZPs are about 10% and 40%, respectively.[44] In this study, nevertheless, we modify an AZP composed of opaque metal zones that induce EOT, thus boosting the diffraction efficiency.

Figure 14 shows the schematic Figures of a proposed MDA-PFZP. A circularly polarized light is normally incident from the back of the fused silica. The reason of using circularly polarized incident light is that SPs for all azimuth can be uniformly excited, while the linearly polarized light only partially excite SPs with cosine dependence.[45] In our study, we chose $\lambda = 405$ nm and transparent $N_{zone} = 7$. The radii of each zone are calculated using Eq. (1.1). To construct a zone width decreased by half, the radii of the *n*-th zone are re-calculated by $\mathrm{r}'_n\ (n = 1,3,5\cdots) = (\mathrm{r}_{n+1} + 3\,\mathrm{r}_n)/4$ and $\mathrm{r}'_n\ (n = 2,4,6\cdots) = (3\,\mathrm{r}_n + \mathrm{r}_{n-1})/4$, respectively. The dielectric constant of the silver at $\lambda = 405$ nm is $\varepsilon_{Ag} = -4.01 + 0.70i$.[46] The dielectric constants of fused silica substrate and the Poly (methyl methacrylate) (PMMA) layer spun on the metal are set as $\varepsilon_{\text{fused silica}} = 2.16$ and $\varepsilon_{\text{PMMA}} = 2.34$, respectively. After trial-and-error, the thickness of the silver film was chosen as $t_{Ag} = 100$ nm.

TEMPEST, a finite-difference time-domain (FDTD) method-based Maxwell equation solver developed by University of California at Berkeley, was employed to conduct electromagnetic simulation of the MDA-PFZP structures. The simulation grid size was $\Delta x = 20$ nm, $\Delta y = 20$ nm, and $\Delta z = 20$ nm.

3.5 Results and Discussions

3.5.1 Calculation of effective refractive index

First of all, we discuss the physical origin of the extraordinary optical transmission in our structure. The free electron gas in a high conductivity metal gives rise to a unique dielectric response described by the Drude model

$$\varepsilon_m = 1 - \frac{\omega_p^2}{\omega(\omega + i\gamma)} \tag{3.4}$$

where ω_p is the bulk plasma frequency and γ is the scattering rate of the electrons.

Consider a lossless Drude metal ($\gamma = 0$). When $\omega > \omega_p$, the permittivity of metals is positive and the light can propagate through it. Conversely, when $\omega < \omega_p$, metals possess negative permittivity and the light propagation in the metal is forbidden. Interestingly, though, even when ε_m is negative or $\gamma > 0$ (lossy Drude model), the propagation of light may still be allowed in the form of a surface wave on the metal.[47] This occurs to metals such as Au and Ag in visible or UV light. Consider two closely placed parallel metallic plates and a dielectric filling in between them, the SPs on each surface will be coupled and propagate in a waveguide mode for TM-polarized light. The complex propagation constant ($\beta = \beta_r + \beta_i i$) can be calculated from the equation[48, 49]

$$\tanh\left(\sqrt{\beta^2 - k_0^2\varepsilon_d}\, w/2\right) = -\frac{\varepsilon_d \sqrt{\beta^2 - k_0^2\varepsilon_m}}{\varepsilon_m \sqrt{\beta^2 - k_0^2\varepsilon_d}} \tag{3.5}$$

where k_0 is the wave vector of light in free space, ε_m and ε_d are the relative dielectric constant for the metal and the dielectric in the slit, respectively, and w is the slit width. Then the effective refractive index n_{eff} is given by $n_{eff} = \beta/k_0$.

Figure 16(a) and (b) plot the real part of n_{eff} and propagation length of SPPs as a function of silt width *w,* assuming the slit is filled with PMMA or air. For example, at $\lambda = 405$ nm and slit width $w = 100$ nm, the effective refractive indices when the slit is filled with PMMA or air are 2.48 and 1.38, respectively. At the same condition, the propagation length of the slit filled with PMMA or air are 133 nm and 676 nm, respectively. Considering the silver thickness of proposed plasmonic zone plate lens (i.e., $t_{Ag} = 100$ nm) which is equal to the propagating length for incident light to transmit the proposed device, the minimum zone width need to be over 60 nm as shown in Figure 16(a). When filled with PMMA, Re(n_{eff}) is higher than that filled with air, indicating that the field in the slit is more localized and closer to SP resonance. Then the localization and SP resonance enhance the transmitted field.

Note that slit width is close to the outmost zone width of the proposed MDA-PFZP. Figure 16(c) plots the real part of n_{eff} and propagation length of SPPs as a function of ε_d at the slit width $w = 100$ nm. It can be seen clearly that Re(n_{eff}) grows steadily and the propagation length of SPPs decreases exponentially with ε_d increasing. Also, in order to overcome the thickness of proposed device, the propagation length of SPPs must have the value larger than 100 nm which is corresponding to $\varepsilon_d = 2.5$. The plot indicates that SP resonance in this parallel-plate configuration occurs $\varepsilon_d = 3.8$.

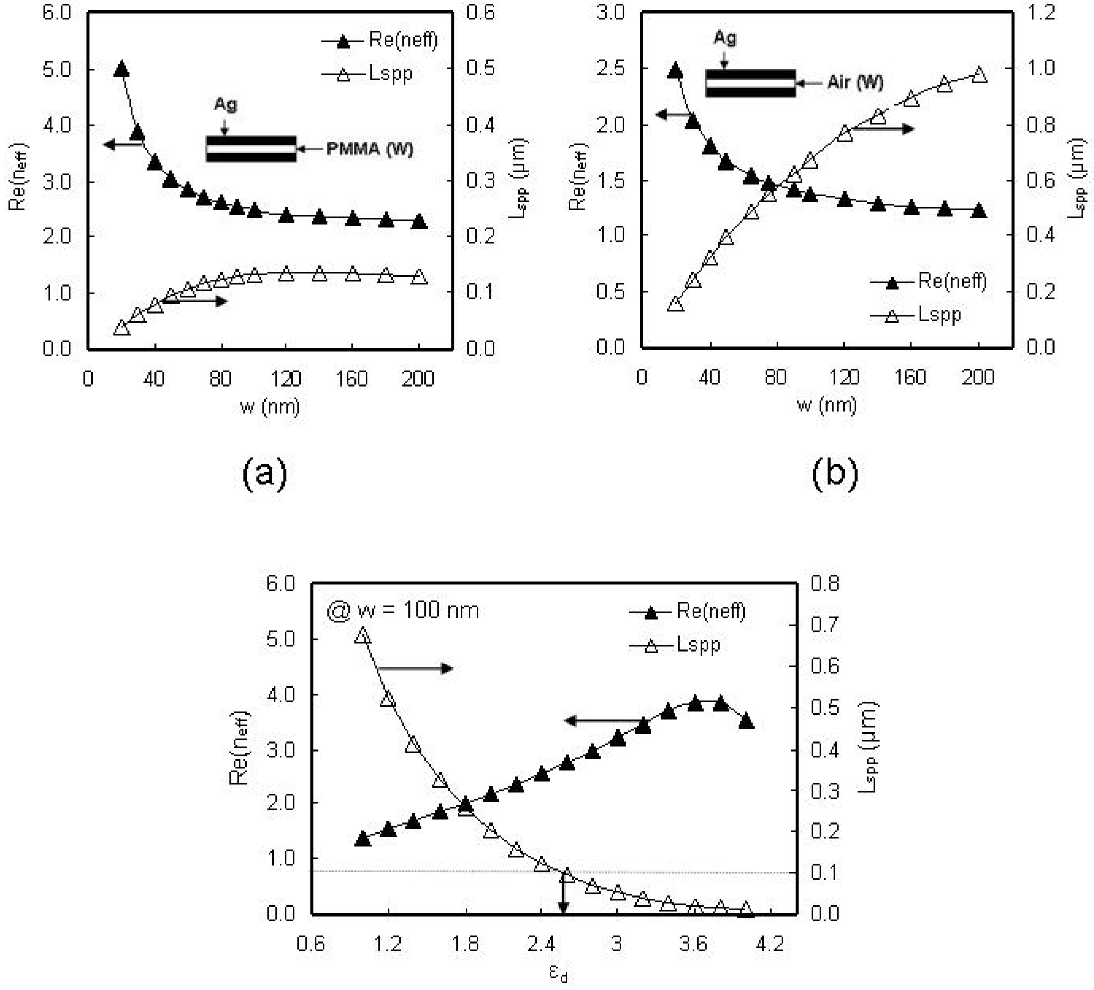

(a)

(b)

(c)

Figure 16 The effective refractive index Re(n_{eff}), $n_{eff} = \beta/k_0$, and propagation length of SPPs (L_{spp}) as a function of slit width w. The slit is filled with (a) PMMA and (b) air. The n_{eff} and L_{spp} vs. dielectric constant ε_d is shown in (c), when $w = 100$ nm.

3.5.2 Dependence of slit width at plasmonic zone plate lenses

Figure 17(a) plots the maximum intensity and FWHM vs. zone width. To compare with conventional FZP, the zone width in Figure 17(a) is expressed as the percentage of the zone widths of a conventional FZP with identical focal length. It is observed that the maximum intensity of the focal spot decreases with the zone width decreasing because of the decrease in transparent area. Meanwhile the focused spot size also decreases. When the zone width reaches half that of a conventional FZP, the spot size reaches minimum, and thereafter the spot size increases. The focused spot is the interference of the multiple beams from each zone. Smaller zones correspond to more coherent interference, helping increase the intensity at the focus. But this increased coherence also increases the intensity near the focus. When the zone width is 50% of conventional FZP, the ratio of the intensity at the focus to that at the side lobe reaches maximum, corresponding to the smallest focused spot. After that, the ratio decreases, although the intensity at the focus still increases, meaning that the spot size expands. From this plot, we chose 50% zone width for our proposed MDA-PFZP.

Figure 17(b) shows the light field focused by the MDA-PFZP to the focus f = 0.5 μm away from the interface between silver and PMMA. Figure 17(c) shows the PSF on the focal plane. Note that the outmost zone width has been reduced from 205 nm for conventional FZP to 102 nm for MDA-PFZP. As a result, the FWHM on the focal plane is measured to be 162 nm. In far-field optics, the FWHM focused by a diffraction-limited lens is given by FWHM = 0.52λ/NA. Thus the MDA-PFZP achieves an equivalent NA of 1.30, beyond the diffraction limit that may be achieved by a perfect lens (NA = 1). For conventional FZP, the height of the side lobe is considerably larger for small zone numbers (15% of the height of the principal maximum when the number of zones is 4).[50, 51] A zone plate is capable of bringing only certain amount of incident light into the focal plane and the unfocused light makes the minima of the intensity distribution non-zero, as shown in Figure 17(c).

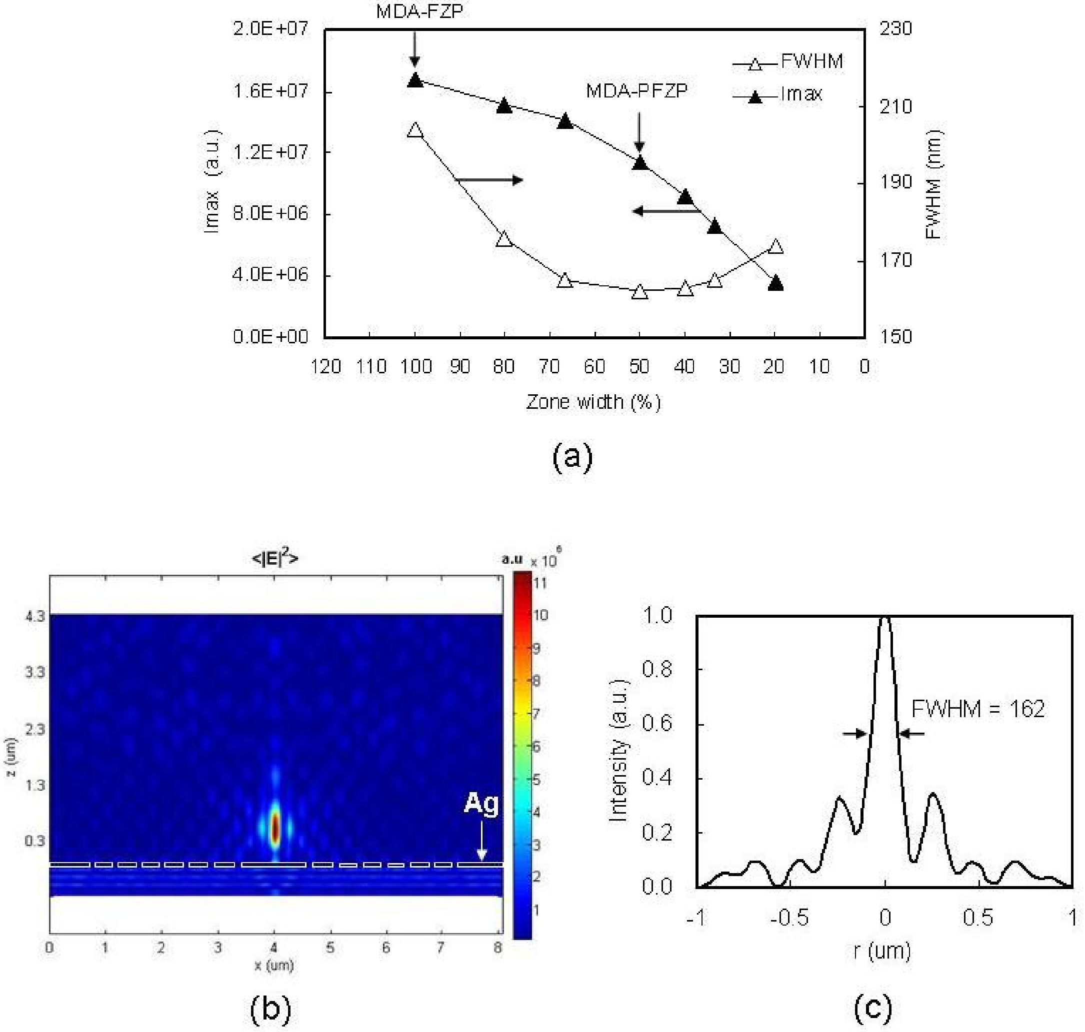

Figure 17 (a) Maximum intensity and spot size (FWHM) at focal plane as a function of zone width, assuming $f = 0.5$ μm. (b) Optical field emanating from MDA-PMZP and (c) the PSF at the focal plane.

Due to the limitation of memory size of our workstation, we used 7 transparent zones, but the side lobe can be lowered by increasing the number of zones. Note that Figure 17(c) shows nonsymmetrical side lobes, which is believed to result from numerical errors. TEMPEST progressively updates one grid by another in a computing cycle, which may cause progressive spread of numerical errors.

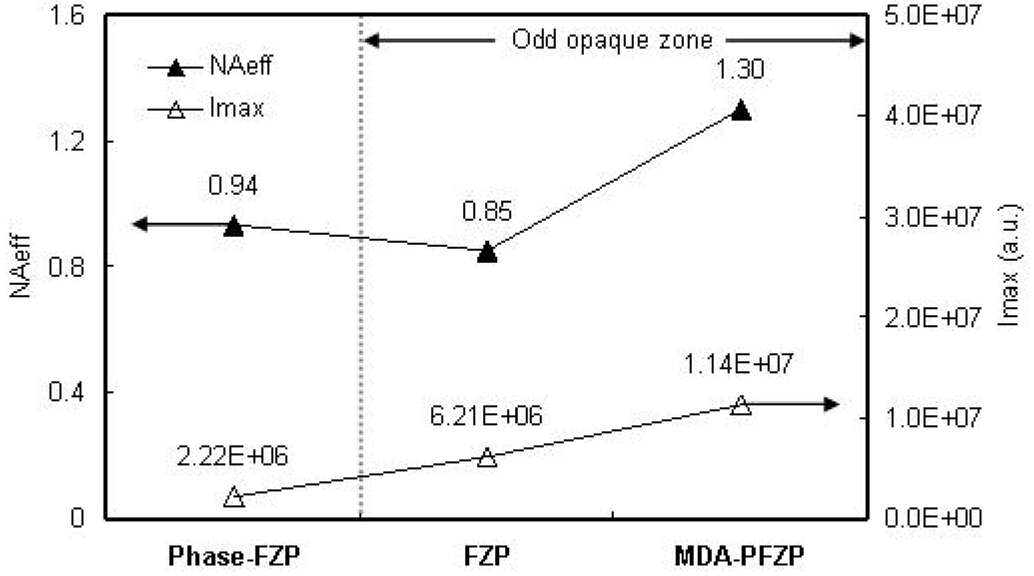

Figure 18 The comparison of the effective NA and maximum intensity (I_{max}) at the focal plane for different devices: phase FZP, amplitude FZP, and MDA-PFZP, all having $f = 0.5$ μm.

In Figure 18 we present the comparison of effective NA and maximum intensity. We include phase zone plate and positive zone plate (odd zones opaque) such as FZP and MDA-PFZP, all of which have 0.5 μm focal length. Both the positive FZP and the MDA-PFZP have a 100 nm thick silver film as the opaque area. For phase zone plate, the phase difference (ϕ) due to the thickness difference (*t*) can be expressed as $\phi = t(n_s - 1)2\pi/\lambda$, where n_s is the refractive index of substrate. In case of fused silica zone plate, the optimized value of *t* is approximately 430 nm for maximum intensity ($\phi = \pi$). The relatively low maximum intensity of the phase zone plate is due to its relatively uneven topography, which makes the diffracted evanescent fields undergo multiple scattering and couple with radiating fields.[52] The zone positions of FZP are given by the Fresnel Zone Plate formula (Eq. 3.1) so these zones have larger zone widths (typically 205 ~ 261 nm), larger than λ/2n. Therefore they can support propagation modes. Their transmittance mainly depends on the propagation modes. On the other hand, the zone widths of MDA-PFZP (102 ~ 130 nm) are reduced to half that of FZP, smaller than λ/2n. So there is difficulty in supporting propagation modes in these zones. But employing MDA structure can further support the propagation modes through increasing n_{eff}. As a result, we can achieve not only high intensity but also enhancement of effective NA.

3.5.3 Dependence of design parameters at plasmonic zone plate lens

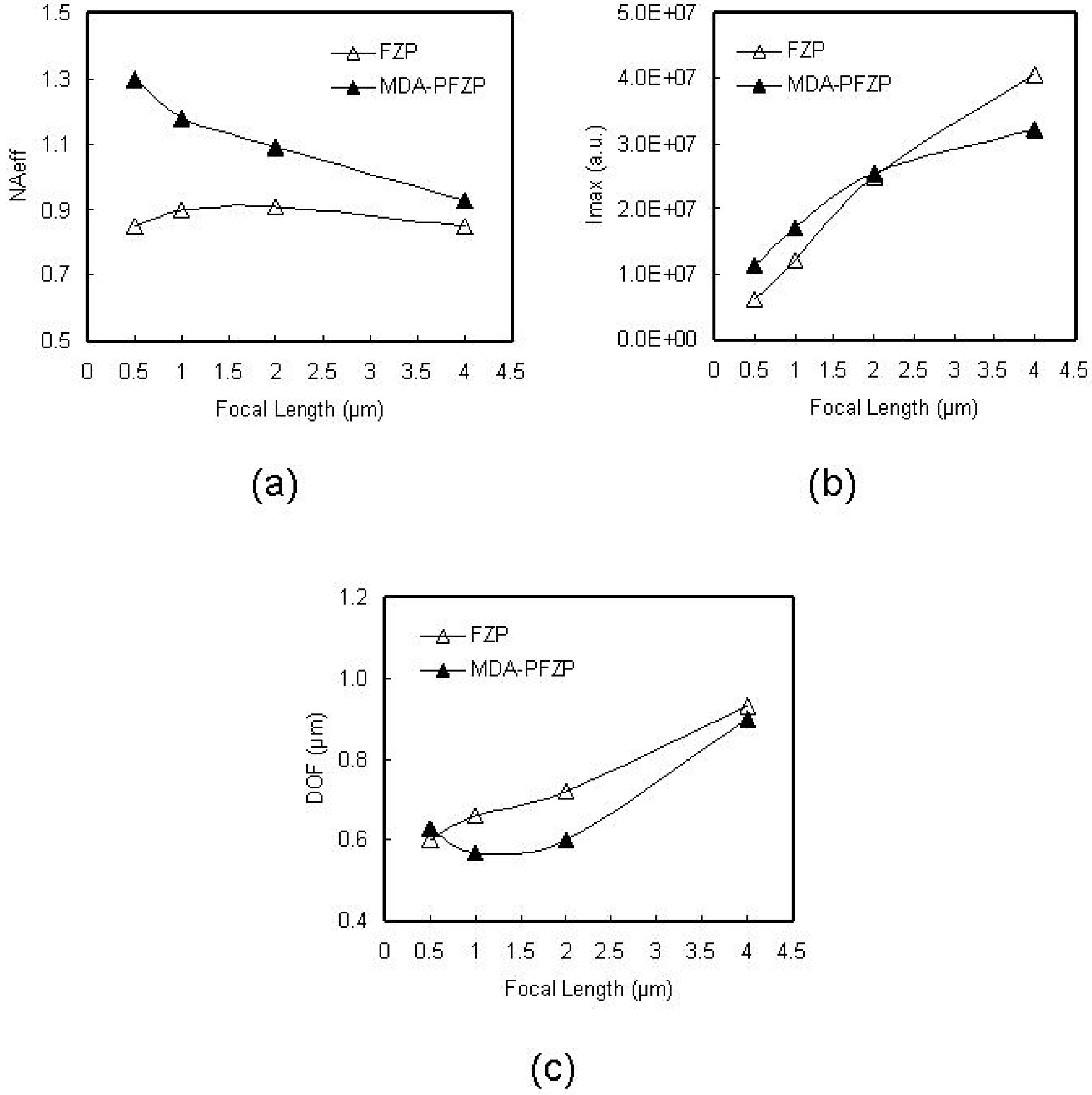

Figure 19 The comparison of (a) NA_{eff}, (b) I_{max}, and (c) DOF for amplitude FZP and MDA-PFZP, respectively, as a function of focal length.

Simulations are also performed to evaluate the effect of focal length. Figure 19 compares a FZP and a MDA-PFZP, both consisting of 7 transparent zones. Figure 19(a) shows a MDA-PFZP whose focal length is between λ and 10λ. This mid-field focusing device has $NA_{eff} = 1.30 \sim 0.93$. Figure 19(b) and (c) show that the depth of focus (DOF) of the MDA-PFZP is marginally smaller than amplitude FZP over most of the range, while the MDA-PFZP has slightly larger intensity at the region of less than 5λ. The smaller DOF is not surprising, given its larger NA. For most practical applications, higher intensity and larger DOF as well as smaller spot size are all desired particularly to boost throughput. The analysis in Figure 19 reveals that our proposed structure satisfies the needs.

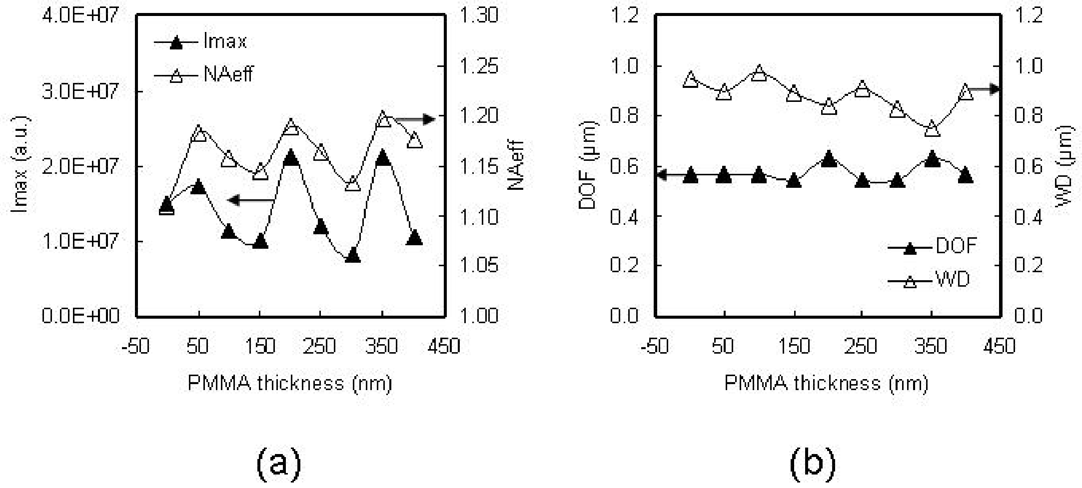

Figure 20 The comparison of (a) I_{max} and NA_{eff} and (b) DOF and working distance (WD) for MDA-PFZP as a function of PMMA thickness. Assume $f = 1$ μm, $t_{Ag} = 100$ nm.

To explore for better MDA structure, Figure 20 presents the effect of changing dielectric thickness, i.e., PMMA thickness on top of the metal. It assumes a MDA-PFZP with $f = 1.0\ \mu\text{m}$. We found that maximum intensity at focal plane can be modulated by changing dielectric thickness due to Total Internal Reflection (TIR) in the dielectric as shown in Figure 20(a). The phase matching between the scattered light beam from zones and the reflected light beam by TIR is believed to cause the "swing effect" in I_{max}. The DOF is essentially a constant regardless of the PMMA thickness, since DOF is usually governed , as in a conventional FZP, by[33]

$$\mathrm{DOF} = \pm\frac{1}{2}\frac{\lambda}{(\mathrm{NA})^2} = \pm\frac{2(\Delta \mathrm{r})^2}{\lambda}. \tag{3.6}$$

The WD, measured from the top of PMMA to the focused spot, is given by $f - t_{\mathrm{PMMA}}$. It varies with PMMA thickness t_{PMMA}, because t_{PMMA} changes the focal length, resulting in a "swing" manner. This may be due to the reflection in the PMMA layer.

3.6 Summary

In conclusion, a variety of applications, such as maskless lithography, scanning optical microscopy, optical data storage, optical antenna, etc., desire high intensity light beams narrower than diffraction limit. The use of FZP is limited by its resolution. Other works in near field optics, such as solid immersion lenses, bow-tie antennas, ridge waveguides, and tapered optical fibers, to name a few, have increased spatial resolution significantly. However, the aforementioned ways have suffered from very limited working distance of less than 100 nm or very low transmission efficiency.

As a trade-off between resolution and working distance, we designed and analyzed a metallic-dielectric-air structured plasmonic Fresnel zone plate which has a sub-diffraction-limit spot with high intensity. Our simulation predicts 162 nm FWHM (equivalent to NA 1.30) with high diffraction efficiency at focal length of 0.5 μm under 405 nm illumination. The small FWHM is mainly attributed to the narrow zone width, and the high transmission is related to extraordinary optical transmission. We calculated the complex propagation constant affected by the dielectrics filling the zones and surface plasmon resonance in the metal. This gives rise to the EOT in MDA-PFZP. Finally, we found that the maximum intensity at focal plane can be modulated by changing PMMA thickness due to TIR in the dielectric without affecting NA or DOF. The fabrication of MDA-PFZP is expected to be almost identical to amplitude-FZP, only an additional PMMA spin-coating being needed. While the fabrication of phase-FZP is more costly due to the difficulty in phase control. The proposed device, with its high NA (> 1), reasonable focal length (λ to 5λ), high transmission and low cost of fabrication, is expected to find promising applications in the fields mentioned above.

CHAPTER IV

HIGH EFFICIENT OPTICAL FOCUSING OF PLASMONIC ZONE PLATE LENS*

4.1 Introduction

Fresnel zone plate (FZP) is composed of a series of concentric zone rings, alternatively being opaque or transparent zone, with gradually decreasing period. It has been used for focusing and imaging of x rays and extreme-ultraviolet (EUV) radiation, which enables many applications such as nanolithography, spectroscopy, near-field or far-field optical microscopy, and optical antenna. Two major issues associated with FZP are its resolution which is limited to roughly the width of the smallest zone, namely λ/2, and the transmission efficiency which is often low (approximately from a few percent to 40%). Several approaches in the near-field region have been proposed to overcome the limit of resolution.[53, 54] However, the resulted diffraction efficiency of these devices was relatively low (typically less than a few percent), not comparable to far-field devices.

---

* Reprinted with permission from "High efficient optical focusing of a zone plate composed of metal/dielectric multilayer" by Hyun Chul Kim, Hyungduk Ko, and Mosong Cheng, Opt. Express, 17, 3078 (2009). Copyright by Optical Society of America. (www.opticsinfobase.org)

The development of electromagnetic simulation tools, nano-fabrication techniques, and physical analysis tools has enabled manipulation of ‘light’ on nano scale. Since Thomas Ebbessen and co-workers reported the extraordinary optical transmission (EOT) through 2D arrays of subwavelength holes perforated in metallic films in 1998,[17] many renewed attentions have been made to figure out the physical origin of this phenomenon theoretically and experimentally. However, there is still controversy on the enhanced transmission phenomenon. At present, it is widely accepted that the EOT can be explained by diffraction assisted by the enhanced fields associated with surface plasmons (SPs).[55] Moreover, there have been many efforts to further enhance the transmission geometrically. Tang and his co-workers demonstrated that the enhancement of optical transmission in the Ag/SiO_2 multilayer with a periodic array of subwavelength holes originates not only from SPs but also from the coupling of SPs with nanostructures which is multiple scatterings and the coupling of electromagnetic waves on the interface of the multilayer.[56]

4.2 Modeling and Simulation Methodology

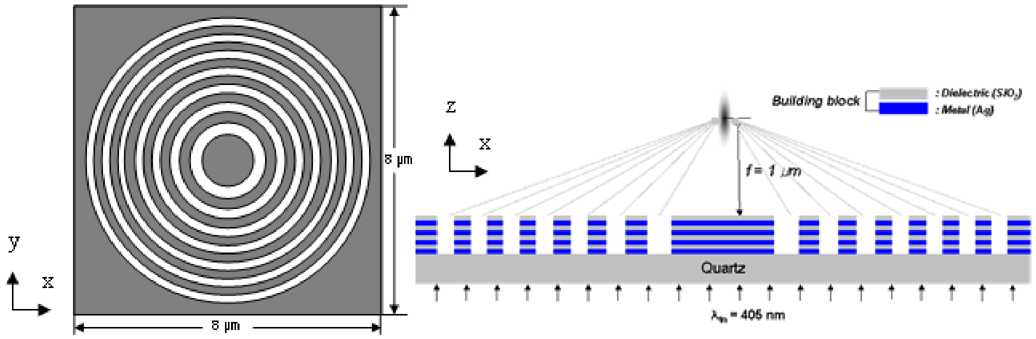

(a) (b)

Figure 21 Schematic figures of the proposed multilayered zone plate structure: (a) Top down view in xy plane, and (b) cross-sectional view in xz plane (y = 4.0 µm).

Figure 21 illustrates the schematic diagrams of the proposed structure, where a zone plate, center being opaque, has sandwich structure with building block (N) of silver and silicon dioxide. The dimensions of the zone plate are obtained from the classical equation used in designing conventional FZP. By comparing the transmission efficiency between a multilayered zone plate (Multi-ZP) and a conventional monolayered zone plate (Mono-ZP), the relative enhancement in the field intensity can be evaluated. The thickness of the silver film in the Mono-ZP is comparable to total thickness of Multi-ZP. Each building block of Multi-ZP has identical focal length (f = 1 µm), which makes it easy to fabricate, the thickness of metal layer being t_m = 30 nm, and the thickness of dielectric layer t_d = 30 nm. In addition, we mainly use λ = 405 nm, ε_{Ag} = -4.01+0.70i, and ε_{siO2} = 2.16, respectively,[46] and the light used to excite the surface plasmon polaritons (SPPs) in the zone plate is a circularly polarized wave normally incident from the bottom of the quartz wafer. The focusing properties of the proposed zone plate are simulated and analyzed by TEMPEST, a Maxwell equation solver based on 3D finite-difference time-domain (FDTD) method.

4.3 Numerical Experiment and Discussions

4.3.1 Comparison between Mono_ZP and Multi_ZP

Near-field focusing or beaming properties of FZP and plasmonic lens (PL) have been investigated in the visible regime.[39-41, 57, 58] The results have showed the subwavelength focusing or beaming characteristics in the near field are attributed to the interference of diffracted evanescent waves from a large numerical aperture. However, those structures still suffer from lower transmission efficiency (η) even though optical field enhancement by EOT phenomenon is introduced. In this article, by modulating the effective refractive index (n_{eff}) of the dielectric layer in building blocks, in which SPPs propagate transversally, we demonstrate a metal/dielectric multilayered zone plate with high transmission efficiency.

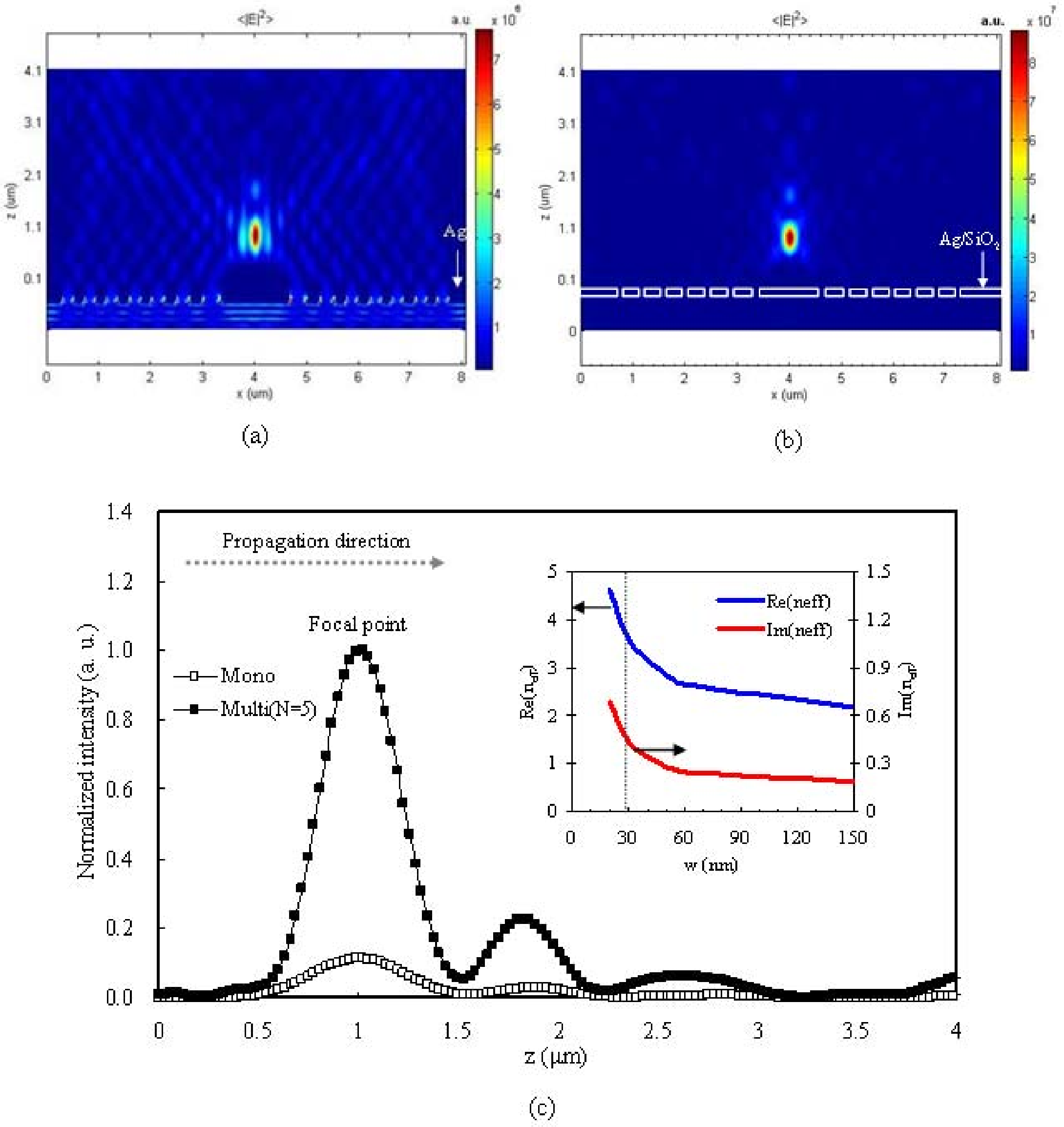

(a)

(b)

(c)

Figure 22 Field distributions of the transmitted field in xz plane: (a) monolayered zone plate (Mono-ZP) and (b) multilayered zone plate (Multi-ZP) with N = 5, and (c) comparison of the normalized intensity for the Mono-ZP and Multi-ZP, respectively, along z direction. The inset shows real part and imaginary part of effective refractive index as a function of the width of two metal plates.

Figure 22(a) and (b) show the distributions of the transmitted field intensity on the xz-plane for Mono-ZP and Multi-ZP, respectively, with N = 5. In the Mono-ZP, the energy flow in the vicinity of the silver/air interface in the zone rings is remarkably strong, and its intensity attenuates with distance from the interface to both the silver and the air. These are the essential features of the excited surface plasmon on the metal surface.[59] In Figure 22(c), it is clear that at the focal point, the field enhancement of Multi-ZP is estimated to be about 9.0 times that of Mono-ZP. It is well known that a light wave tends to localize itself mostly in a medium with higher refractive index than its adjacent ones and thereby the light prefers to propagate with low phase velocity.[60] Thus the incident light can propagate along the dielectric layer included in building blocks, generating SPPs in the interface. We can count the dielectric layer in the building blocks as a metal-insulator-metal (MIM) waveguide. Therefore, considering two closely placed parallel metallic plates filled with higher refractive index dielectric layer, the complex propagation constant ($\beta = \beta_r + \beta_i i$) with slit width can be calculated as[48, 49]

$$\tanh\left(\sqrt{\beta^2 - k_0^2\varepsilon_d}\, w/2\right) = -\frac{\varepsilon_d\sqrt{\beta^2 - k_0^2\varepsilon_m}}{\varepsilon_m\sqrt{\beta^2 - k_0^2\varepsilon_d}} \tag{4.1}$$

where k_0 is the wave vector in free space, ε_m and ε_d are the relative dielectric permittivity of the metal and the dielectric, respectively, and w is the width of two metallic plates. The effective refractive index ($n_{eff} = n'_{eff} + n''_{eff} i$) of the dielectric layer is given by $n_{eff} = \beta/k_0$. The inset of Figure 22(c) plots the effective refractive index as a function of slit width where metal and dielectric films are Ag and SiO_2 films, respectively. In obtained effective refractive index, the real part of the effective refractive index increases rapidly with slit width decreasing. The coupling of SPs in the Ag/SiO$_2$ multilayer can be excited even in small slit width due to the tendency of the light to be localized in the higher effective refractive index.

Simulations are also performed to evaluate the effect of the number of building blocks as shown in Figure 23. It is noted that transmission efficiency is calculated by the maximum intensity at the focal point divided by the integral of incident field intensity given from area within the outmost radius of zone plate. The transmission efficiency is found to be maximized when the number of building block approaches six, but the focal spot size is found to be increased, as shown in Figure 23(a). Since each building block is designed to have an identical focal length, they contribute differently to the focal spot in the z direction. As a result, the resultant focal spot will be smeared because the focal planes of each building block do not coincide. In the case of Mono-ZP, on the other hand, it is observed that after the metal layer thickness is approximately one order thicker than skin-depth (corresponding to t_{Ag} = 120 nm), the transmission efficiency decreases with the thickness increasing. Note that the metal layer thickness in a Mono-ZP corresponds to the total building block in a Multi-ZP. Moreover, its transmission efficiency is much smaller than that of Multi-ZP. As illustrated in Figure 23(b), when the focal planes of each building block coincide, the transmission efficiency increases and approaches the maximum value (i.e., approximately 40%) with the number of building blocks increasing. Simultaneously, the spot size decreases and approaches the minimum value (i.e., FWHM = 195 nm).

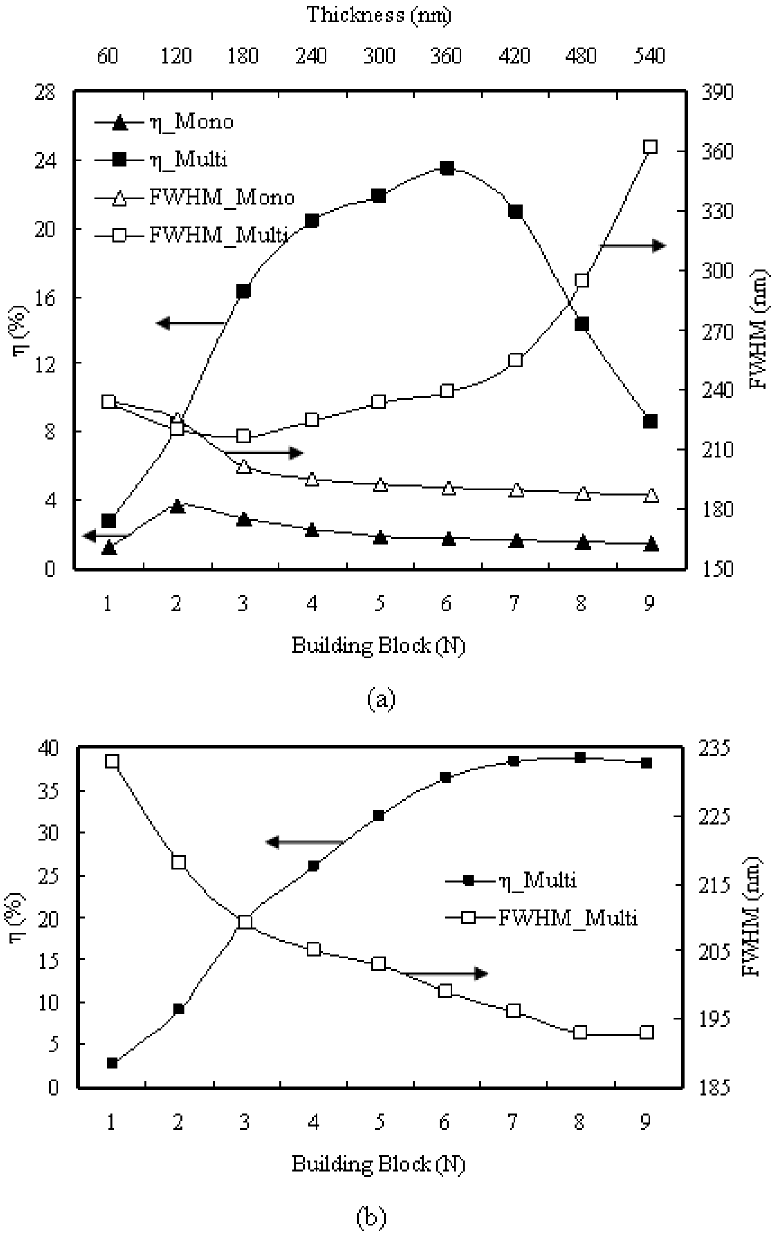

(a)

(b)

Figure 23 (a) Comparison of transmission efficiency (η) and spot size (FWHM) as a function of the building block for the Multi-ZP and corresponding thickness for the Mono-ZP, respectively. (b) The transmission efficiency and spot size when the focal planes of each building block coincide.

When the incident light impinges on the surface of metal, SPPs can be excited and propagate along the surface. When the SPPs arrive at a slit in the metal, most of them is scattered by slit edge, leaks into the slit and radiates new bulk waves and surface waves.[61] These new bulk waves and surface waves excite new SPPs on the slit walls. The new SPPs propagate along the metal-dielectric building block. It can support another path for incident light to transmit the device. In other words, the SPPs convert the incident light to surface wave. And the surface wave is then injected to the slit and then travel to the exit surface. The field intensity in the slit is higher than at other positions on the metal by orders of magnitude. Although the metal films are absorptive to the 405 nm wavelength, the metal/dielectric multilayer does not absorb the incident light. Most of the light energy is converted to SPP, traveling along the surface to the slit with minimal decay. The zones in the multilayer then provide channels for SPP to exit the ZP. So most of the incident light energy can transmit through the Multi-ZP, even though the multilayer is absorptive. As a result, the transmission of a Multi-ZP can approach the theoretical limit of about 40.5% set by a perfect phase FZP, in which all zones are transparent and have alternating 0/π phase shift.

4.3.2 Dependence of dielectric materials at Multi_ZP

Figure 24 shows the normalized intensity of different dielectric materials with N = 5. Maximum normalized intensity is achieved at Al_2O_3 ($\varepsilon = 3.20$) Multi-ZP. The inset of Figure 24 depicts real and imaginary part of the effective refractive index and the propagation length (L_{spp}) of SPPs at w = 30 nm as a function of dielectric permittivity (ε_d).

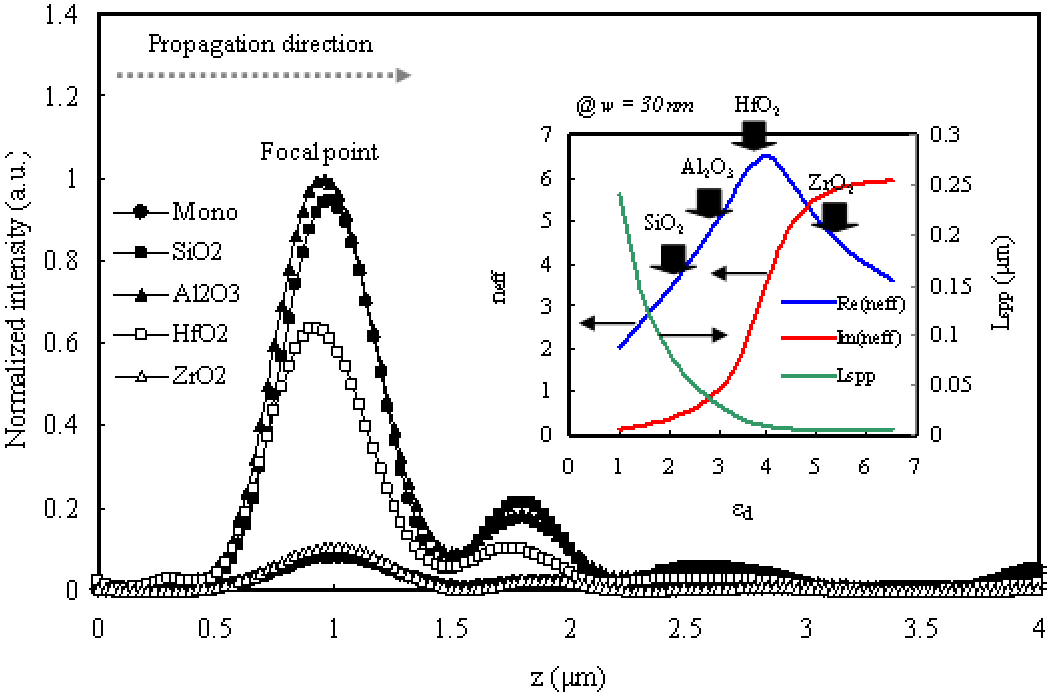

Figure 24 Comparison of the normalized intensity for the various dielectric materials along z direction: SiO_2 (ε = 2.16), Al_2O_3 (ε = 3.20), HfO_2 (ε = 3.92), and ZrO_2 (ε = 5.15), respectively, with N = 5. The inset shows real part ($Re(n_{eff})$) and imaginary part ($Im(n_{eff})$) of effective refractive indices, and propagation lengths (L_{spp}) of SPPs as a function of the dielectric permittivity (ε_d) at w = 30 nm.

The complex propagation constant and thereby effective refractive index of SPPs increases until ε_d approaches $|Re(\varepsilon_m)|$. The frequency at which $\varepsilon_d = |Re(\varepsilon_m)|$ is called the resonant surface plasmon frequency. In our simulations, given by $|Re(\varepsilon_m)|$ = 4.01, HfO_2 (ε = 3.92) layer is predicted to achieve the closest resonance condition.

However, much higher transmittances are achieved at SiO_2 and Al_2O_3 layers than HfO_2. Therefore, we also need to take the propagation length of SPPs into account. In general, propagation length of SPPs is provided by the imaginary part of the complex propagation constant, the distance where the intensity falls to 1/*e* of its initial value is given by $L_{spp} = (2\,\mathrm{Im}(\beta))^{-1}$. Notice that there is a trade-off between the real part and imaginary part of effective refractive index. Although HfO_2 layer approaches the closest resonance condition, simultaneously the imaginary part of the complex propagation constant increases rapidly and thereby the propagation length of SPPs decreases. As a result, it is evident that the imaginary part of the complex propagation constant and thereby propagation length of SPPs have an important role to the propagation for the coupled electromagnetic wave on the interface of the multilayer. For ZrO_2 layer ($\varepsilon_d > |\mathrm{Re}(\varepsilon_m)|$), both upper and lower interfaces cannot support a SPP mode, which is under cut-off condition.[62] Hence, its field enhancement is similar to that of Mono-ZP.

In addition, Table 5 shows summary for the dependence of dielectric materials in Multi-ZP to help understanding. It is clearly seen that in order to obtain the maximum transmission efficiency in the Multi-ZP, the imaginary part of the calculated complex propagation constant, governing the decay length of surface plasmons in the multilayered zone plate, should be considered.

Table 5 Dependence of dielectric materials in Multi-ZP.

	Air	SiO_2	Al_2O_3	HfO_2	ZrO_2
ε_d @ λ = 405 nm	1.0	2.16	3.20	3.92	5.15
$Re(n_{eff})$ @ w = 30 nm	2.04	3.62	5.44	6.50	4.83
$Im(n_{eff})$ @ w = 30 nm	0.13	0.45	1.34	3.28	5.63
L_{spp} (μm) @ w = 30 nm	0.240	0.072	0.024	0.010	0.006
I_{nor} @ focal point	0.08 (@ Mono)	0.94	1.00	0.64	0.10

4.4 Summary

In conclusion, a method to obtain high optical field enhancement in the zone plate was proposed. By using metal/dielectric multilayered zone plate, optical field enhancement originates not only from SPPs-assisted diffraction along the propagation direction of incident light, but also from the coupling and multiple scattering of SPs in the multilayer. The imaginary part of the effective refractive index, governing the decay of SP in the multilayer, also has an important role to the propagation of the coupled electromagnetic wave. The proposed Multi-ZP can achieve transmission efficiency close to the theoretical limit of 40.5% set by an ideal alternating phase FZP. Meanwhile it can achieve a FWHM noticeably less than $\lambda/2$, the theoretical limit of a conventional far-field FZP. The achieved optical field enhancement, as high as 9 times that of conventional FZP, is expected to offer significant potentials in many applications such as FZP microscopy, optical antennas, optical sensors, and nano-optics devices.

CHAPTER V

SERS-ACTIVE SUBSTRATE ENHANCED BY GAP SURFACE PLASMON POLARITONS

5.1 Introduction

Since the first observation of single-molecule surface-enhanced Raman scattering (SERS) from aggregates of colloidal particles and deposited metallic nanoparticles,[63, 64] SERS has become a powerful and sensitive technique for the detection of chemical and biological agents. Two main mechanisms are generally attributed to the strong SERS enhancement – the electromagnetic enhancement and the chemical enhancement. Metallic nanoparticles and roughened electrodes have been used as SERS-active substrates in which the enhancement factor (EF) can be 10^6 (average value for conventional SERS) and around 10^{12} (maximum value for single-molecule SERS).[65] It is well established that the electromagnetic enhancement arises from optical excitation of surface plasmon resonances at the metal nanoparticles, which leads to a gigantic increase in the electromagnetic field strength at the particle surface. The origin of the chemical enhancement is believed to be the formation of charge-transfer states by molecules adsorbed at certain surface sites.[66] Its contribution was estimated to be up to 10^2 times on the enhancement factor.[67] Although chemical enhancement can contribute significantly, the majority of the enhancement of Raman scattering intensity is related to the electromagnetic field strength on the surface of the metallic substrate.

For practical applications, it is indispensable to produce SERS-active substrate with reproducible and tunable SERS enhancement. The key to obtain strong and robust SERS enhancement is to excite the localized surface plasmon (LSP) resonance in nanostructured substrate, which is determined by the properties of the metals, the size and shape of the nanostructures, the inter-particle spacing, and the dielectric environment. Most SERS-active substrates consist of disordered metal surface such as metallic nanoparticles, nanorods, nanowires, nanosphere arrays, nanodisks, and nanostrips.[63, 64, 68-72] Recently, there has considerable attention on the electromagnetic field enhancement in gap surface plasmon polaritons (GSPPs),[73-76] which is excited at the narrow gap of the dielectric layer between two metal surfaces. Furthermore, it has been demonstrated that resonators formed by introducing a narrow gap between metal surfaces can support slow SPP modes in the gap region, resulting in strongly enhanced local fields. Those strong enhancements are attractive for important applications such as optical spectroscopy, molecular sensing and detection, and manipulation of light at the nanoscale.

In 2004, the SERS EFs for particle nanostructures were analyzed by Hao and Schatz.[65] In their calculations, it was found that the SERS EFs vary rapidly with the gap size of the dimer structure, and it is only for gaps on the order of 1 nm to 2 nm that can provide exceptionally large EF values such as $|E|^4 = 10^{11}$. For practical applications, however, it is very difficult to control the gap size on the order of 1 nm to 2 nm to reproducibly achieve the predicted results. However, in microelectronic fabrication, it is easy to control the thickness of a deposited film to a high resolution. This makes it straightforward to reproducibly fabricate metal-thin dielectric-metal structures that support GSPPs for SERS applications. In this study, we numerically investigate the optical field enhancement in a silver nanostructure formed on a thin SiO_2 spacer and a thick bottom silver layer.

5.2 Modeling and Simulation Methodology

Manipulation of the light on the nanometer length scale has been explored in a variety of configurations. In addition to metallic nanoparticle substrate, other configurations used for SERS experimentation can be found in Ref.[65, 77-79].

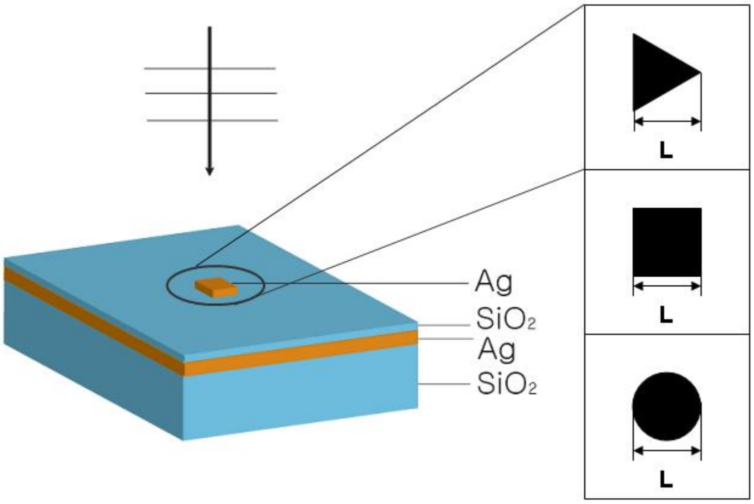

Figure 25 Schematics of the proposed structures for gap surface plasmon polaritons.

Figure 25 illustrates the schematic diagrams of our proposed structures, where an isolated structure, including equilateral triangle, square, and cylinder, is formed on a thin dielectric spacer layer (i.e., SiO_2) on a thick silver substrate. The thickness of the isolated silver nanostructure, the SiO_2 spacer layer and the thick silver layer is fixed at 40 nm, 20 nm and 100 nm, respectively. In our simulation, we use the excitation wavelengths of 785 nm and 633 nm, both are commonly used in Raman spectrometers. The dielectric constants at those wavelengths are: ε_{Ag} = -26.7+1.48i for 785 nm and -15.88+1.077i for 633 nm, and ε_{SiO2} = 2.10 for 785 nm and 2.13 for 633 nm.[46] The light used to excite the GSPPs in the thin spacer region is a circularly polarized wave with normal incidence from the top of the isolated nanostructures. Silver and gold are the most widely used materials for SERS enhancement. It is generally accepted that silver has higher EFs than gold.[70] The field confinement properties of the proposed structures are simulated and analyzed by TEMPEST, a Maxwell equation solver based on 3D finite-difference time-domain (FDTD) method.

5.3 Results and Discussions

5.3.1 Calculation of effective refractive index and propagation length

As shown in the schematic diagram of Figure 25, we can regard the structure as a metal-insulator-metal (MIM) waveguide in which a thin dielectric layer with a thickness t is sandwiched between two metal layers. It is the SPP modes in the symmetric MIM waveguide that lead to strong field enhancement. The gap surface plasmon (GSP) propagation constant (k_{gsp}) can be written as: [73]

$$\tanh(\alpha_d t / 2) = \frac{-(\varepsilon_d \alpha_m)}{\varepsilon_m \alpha_d} \quad \text{with} \quad \alpha_{m,d} = \sqrt{k_{gsp}^2 - \varepsilon_{m,d} k_0^2} \qquad (5.1)$$

where k_0 is the wave vector in free space, ε_d and ε_m are the dielectric constant of dielectric layer and metal layer, respectively. Then the effective refractive index n_{eff} is given by $n_{eff} = k_{gsp} / k_0 = \left(k'_{gsp} + ik''_{gsp}\right)/ k_0 = n'_{eff} + in''_{eff}$.

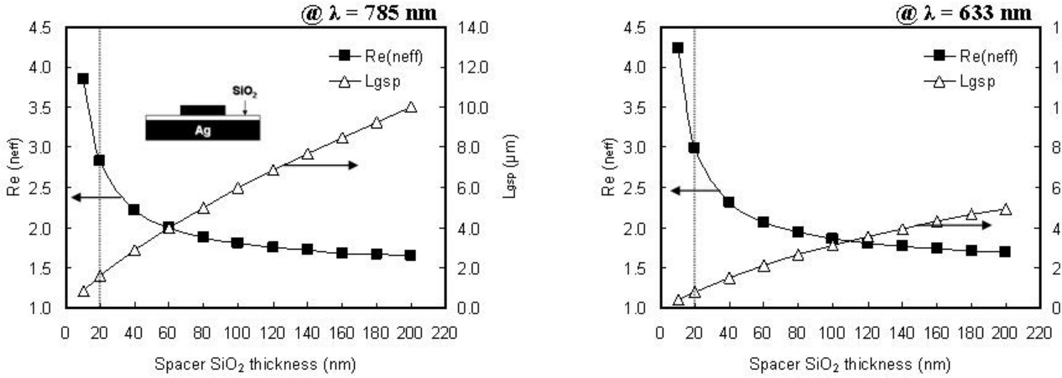

(a) (b)

Figure 26 Calculated effective refractive index Re(n_{eff}), $n_{eff} = k_{gsp}/k_0$, and GSP propagation constant L_{gsp}, $L_{gsp} = (2\mathrm{Im}(k_{gsp}))^{-1}$, as function of SiO_2 spacer thickness. The incident wavelengths are 785 nm in (a) and 633 nm in (b).

Figure 26(a) and (b) plot the real part of the effective refractive index and the GSP propagation length as a function of the SiO_2 spacer thickness. Notice that there is trade-off between the real parts of the effective refractive indices and the GSP propagation lengths. The real parts of the effective refractive indices decrease as the spacer thickness increases, while the GSP propagation lengths increase. It is also observed that the real parts of the effective refractive indices vary rapidly but the GSP propagation lengths change quasi-linearly with the thickness of the SiO_2 spacer. It is noteworthy that even in a very thin SiO_2 spacer, the GSP propagation length can be moderately long. For instance, at λ = 785 nm and t_{SiO2} = 20 nm, the real part of the effective refractive index and the GSP propagation length are 2.82 and 1.6 μm, respectively. At λ = 633 nm and t_{SiO2} = 20 nm, the real part of the effective refractive index and the GSP propagation length are 3.0 and 0.8 μm, respectively.

Table 6 Comparison of effective refractive indices and propagation lengths induced by gap surface plasmons for various metals.

Metals	λ = 785 nm			λ = 633 nm		
	ε_m	$Re(n_{eff})$	L_{gsp} (μm)	ε_m	$Re(n_{gsp})$	L_{gsp} (μm)
Cu	-24.01 +i2.39	2.89	0.82	-11.58 + i1.70	3.32	0.27
Ag	-26.7 + i1.48	2.82	1.60	-15.9 + i1.07	3.00	0.80
Al	-65.65 + i46.08	2.41	0.24	-56.6 + i21.3	2.23	0.39
W	5.86 + i19.6	2.34	0.07	4.8 + i21.3	2.23	0.06
Au	-24.57 + i1.76	2.88	1.16	-9.55 + i1.13	3.61	0.26

In Table 6, effective refractive indices ($Re(n_{eff})$) and propagation lengths (L_{gsp}) induced by gap surface plasmons are elucidated. Considering two parameters such as $Re(n_{eff})$ and L_{gsp}, we choose silver metal as best metal because it has relatively higher effective refractive index and reasonable propagation length. Notice that due to positive dielectric constant of tungsten, its propagation lengths by gap surface plasmons are very small, which is under cut-off condition. Effective refractive indices and propagation lengths by gap surface plasmos for various metals are included in Appendix D.

5.3.2 SERS EFs for various nanostructures

The understanding that localized surface plasmons (LSPs) play a crucial role in the Raman signal enhancement for molecules at a metal surface has triggered a great amount of research into the design and fabrication of SERS-active substrates with controlled surface nanostructure for field enhancement. In our study, we focus on the field intensity distribution as defined in terms of the square of the local electric field, $|E_{Loc}|^2$. Local field EF can be simply given by $|E_{Loc}|^2 = |E_{max}|^2/|E_0|^2$. The SERS EF due to electromagnetic mechanism is usually expressed as $|E_{Loc}|^4$. As mentioned previously, the EF in a conventional SERS experiment is around 10^6 and the EF in a single-molecule SERS experiment is around 10^{12}. In order to directly compare the SERS EFs, we calculate the $|E_{Loc}|^4$ as the SERS EF in our structures.

Figure 27 shows the distribution of the field intensity on the xy-plane at the bottom and the top region (indicated by the red lines in Figure 27(a) and (b)) of the various nanostructures. It shows that stronger field confinement can be obtained for sharper geometries such as the triangular nanostructure. In practical SERS applications, the region where molecules contact directly on the substrate is the top region of the metallic nanostructure. To account for this, we compare the field intensity at the top region and the bottom region of the nanostructures. Because the bottom region of the metallic nanostructure is in contact with SiO_2 layer while the top region is in contact with air, the bottom region has locally higher effective refractive index. It is well known that a light wave tends to localize itself mostly in a medium with higher refractive index and thereby the light prefers to propagate with lower phase velocity.[60] The simulation

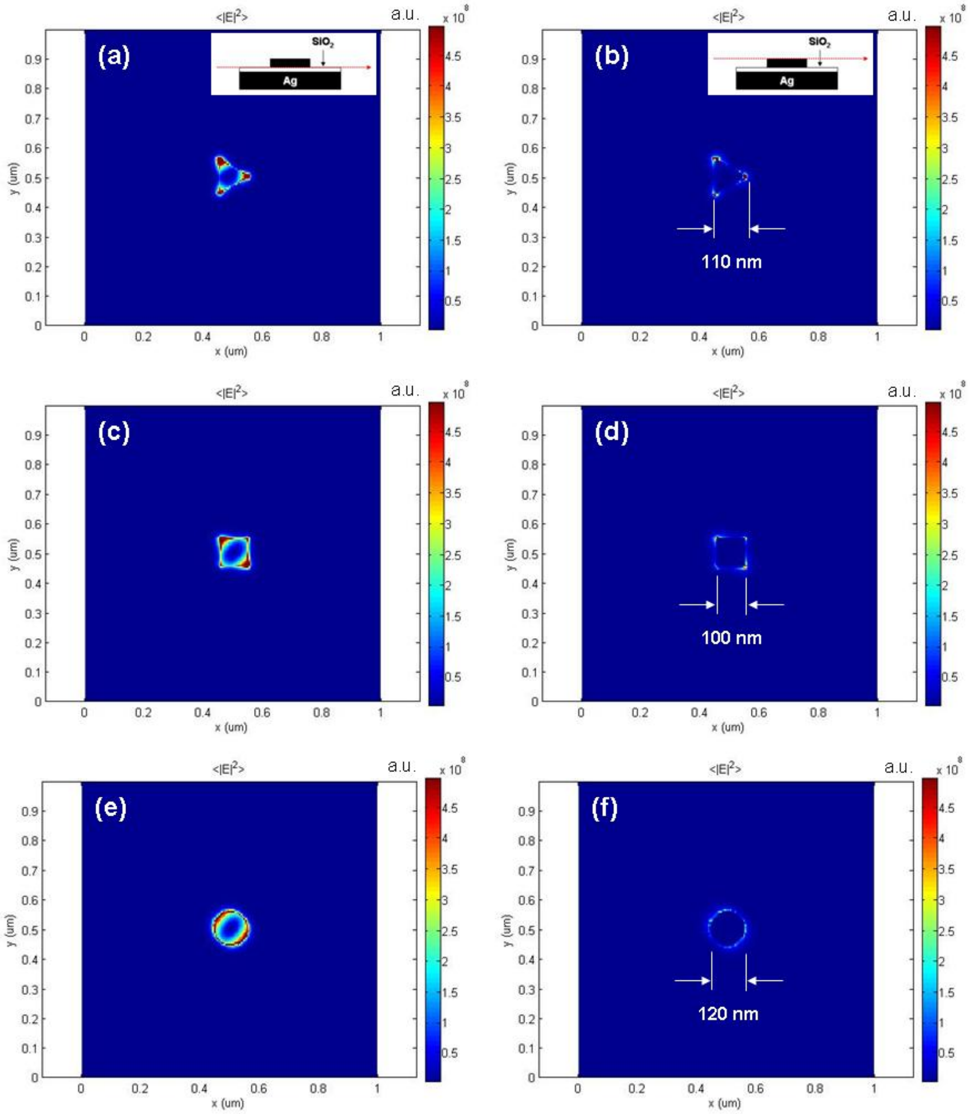

Figure 27 Intensity distribution of the triangular ((a) and (b)), square ((c) and (d)), and circular ((e) and (f)) nanostructures in xy plane. (a), (c) and (e) corresponds to the intensity distribution at the bottom region of the nanostructures (indicated by the red line in (a)) and (b), (d), and (f) corresponds to the intensity distribution at the top region of the nanostructures (indicated by the red line in (b)). The incident wavelength is 785 nm.

results are in agreement with this, showing stronger field intensity at the bottom region than that at the top region.

In general there are two SERS EFs defined for a given SERS-active substrate: the average SERS EF and the maximum SERS EF.[14] The average SERS EF is the one averaged over all possible positions on the surface of the metallic nanostructures. Typically, the SERS EFs for optimized configurations are in the range of 10^5 to 10^6, and are easily achievable with standard substrates. The maximum SERS EF typically occurs at specific positions known as hot spots on the substrate and only molecules absorbed there can benefit from it.

To evaluate the effect of the geometrical parameters on SERS EFs, simulations are performed by varying the length of the nanostructures in various shapes. The results are shown in Figure 28. In general, the maximum SERS EF at the top region is about an order of magnitude smaller than that at the bottom region. It can be explained by the localization of the light to the spacer region which has a locally higher effective refractive index. For smaller structures, extinction is mainly dominated by absorption, with little scattering. This trend is reversed as the size of the structure increases. For larger structures, they emit radiation so efficiently that it is difficult to induce a large polarization in them.[4]

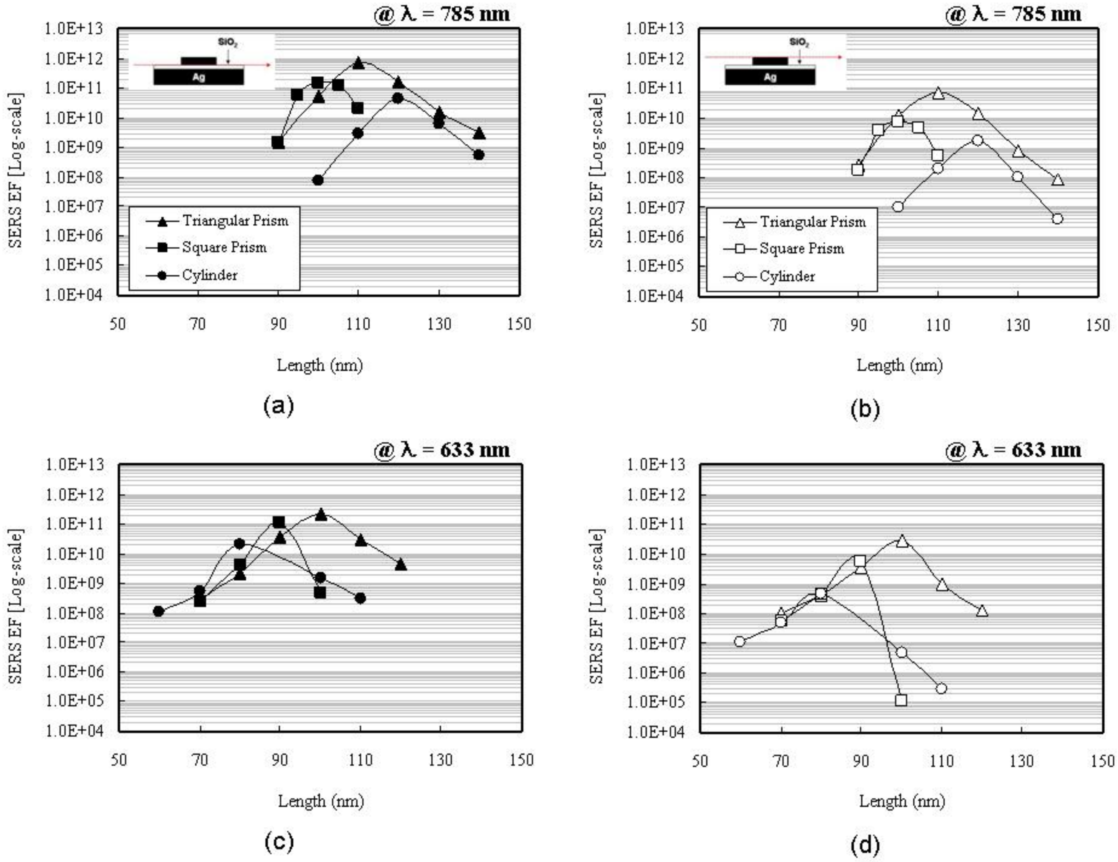

(a) (b)

(c) (d)

Figure 28 Comparison of SERS EFs for different incident wavelengths and nanostructure dimensions. The incident wavelength is 785 nm in (a) and (b), and 633 nm in (c) and (d). (a) and (c) show the EFs at the bottom region of the nanostructure and (b) and (d) show the EFs at the top region of the nanostructure.

In Figure 28(a) and (c), it is clear that at the edge of the equilateral triangular nanostructure, the maximum SERS EFs are estimated to be about 7.0×10^{11} at $\lambda = 785$ nm and $L = 110$ nm, and about 2.1×10^{11} at $\lambda = 633$ nm and $L = 100$ nm. In the case of equilateral triangular nanostructure on a pure SiO_2 substrate, the maximum SERS EFs are estimated to be about 3.0×10^8 at $\lambda = 785$ nm and $L = 110$ nm, and about 1.1×10^8 at

λ = 633 nm and L = 100 nm. Recently, Bozhevolnyi and Sondergaard reported that a metal nanostrip can serve as an optical resonator at the ultrathin metal thickness.[80] They predicted that this nanostrip is capable of a significant field enhancement under resonant excitation when the resonance length is precisely tuned to the resonance scattering peak. In this study, the GSPPs exhibit substantially enhanced effective refractive index and strong field confinement at the spacer region that is much thinner than the wavelength of light. When we compare simulation results at λ = 785 nm and at λ = 633 nm, it is clearly observed that, as the incident wavelength decreases, the size of the nanostructure at the resonance decreases. In other words, if the size of the nanostructure increases, the resonance is red-shifted to longer wavelengths. For SERS applications, in addition to large field enhancement, the resonances must be broad enough to encompass both the exciting laser and the Stokes frequencies. In all simulated nanostructure shapes, the maximum SERS EF is achieved in equilateral triangular nanostructure. In addition, this equilateral triangular nanostructure exhibits a wide range of resonant lengths in which the SERS EF is greater than 10^{11}. Since the lengths of the nanostructures are on the order of 100 nm, all structures simulated in this work can be easily fabricated by electron-beam lithography (EBL), which has precise control of the nanostructure size and shape as well as their arrangement on the substrate.[81] Furthermore, some shapes may also be achieved by low-cost nanosphere lithography (NSL), which has been pioneered by Van Duyne's group to prepare efficient SERS-active substrate.[82, 83]

5.3.3 Dependence of spacer thickness and surrounding medium

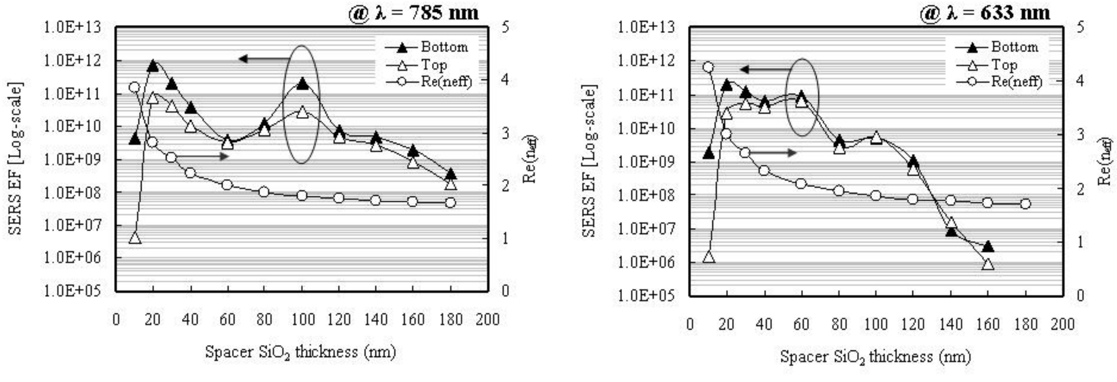

(a) (b)

Figure 29 Comparison of SERS EFs at the bottom region and top region of the nanostructures and the real parts of effective refractive indices as a function of the thickness of the SiO_2 spacer. The incident wavelengths are 785 nm in (a) and 633 nm in (b). The simulated structure is the equilateral triangular nanostructure with a resonant length of 110 nm for 785 nm and 100 nm for 633 nm, respectively.

Because the maximum SERS EFs are induced from LSP resonance based on GSPPs, simulations are carried out to evaluate the influence of the thickness of the SiO_2 spacer layer. Figure 29(a) and (b) show the maximum SERS EFs and the real part of the effective refractive index in equilateral triangular nanostructures for incident wavelengths of 785 nm and 633 nm, respectively, as a function of the thickness of the SiO_2 spacer. At both wavelengths, the nanostructure exhibits a general trend of decreasing in the maximum SERS EFs when the thickness of the SiO_2 spacer increases. To explain this, we can regard the top equilateral triangular nanostructure as a resonant optical antenna on a substrate. The optical properties of an optical antenna are strongly influenced by the substrate material as well as the geometry of the antenna. When the SiO_2 layer thickness increases, the effective refractive index of the substrate decreases as shown in Figure 29(a) and (b), thus the field enhancement in the equilateral triangular nanostructure decreases. The resonant wavelength of an optical antenna can also be shifted by the refractive index of the substrate. This may explain the faster drop in EFs in Figure 29(a) at 60 nm thick SiO_2 and in Figure 29(b) at 40 and 80 nm thick SiO_2 because at those points the incident wavelength is off-resonance with the equilateral triangular nanostructure. Notice that the EFs in the nanostructure with ultrathin spacer layer (i.e., t_{SiO2} = 10 nm) is much lower. This is due to stronger damping by the metal and shorter propagation length of GSPPs supported by an ultrathin SiO_2 spacer.

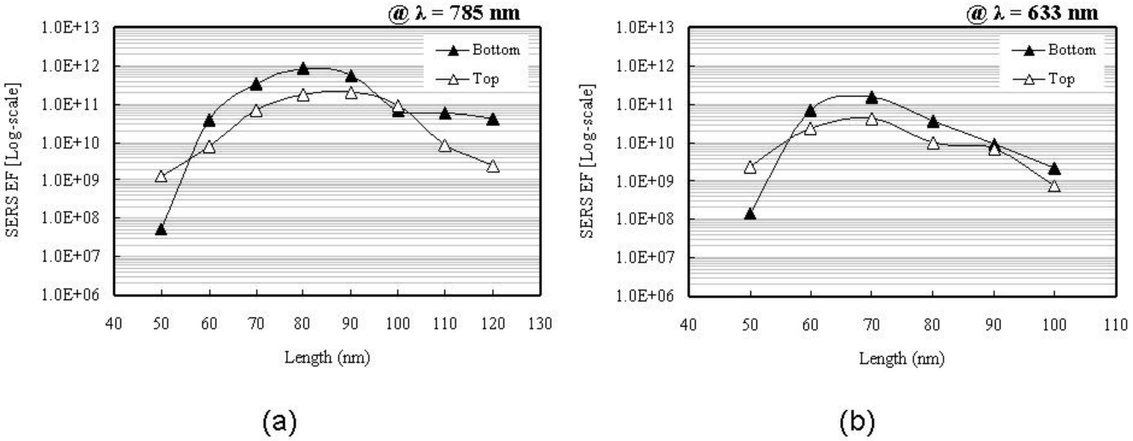

Figure 30 Comparison of SERS EFs of equilateral triangular nanostructures in water as a function of the length (L) of the nanostructures. The incident wavelengths are 785 nm in (a) and 633 nm in (b).

In many practical SERS experiments for molecular detection, the SERS-acitve substrates are immerged in a liquid environment. In order to gain insight on how surrounding medium affects the SERS-active substrates, we calculate the SERS EFs for equilateral triangular nanostructures of various sizes in water at both λ = 785 nm and λ = 633 nm (Figure 30). The dielectric constant of water is 1.77. As shown in Figure 30, similar trends in the maximum SERS EFs are observed as those nanostructures in air (Figure 28). The maximum SERS EFs in liquid solution are similar to those in air. When compared to the nanostructures in air, the resonant lengths of the nanostructures in water are smaller for both incident wavelengths. Because of the higher refractive index of water, the effective wavelengths in the liquid solution decrease from 785 nm and 633 nm to 590 nm and 476 nm, respectively. Hence, the resonance peaks are shifted from 110 nm (in air at 785 nm) and 100 nm (in air at 633 nm) to 80 nm (in water at 785 nm) and 70 nm (in water at 633 nm), respectively. Furthermore, the maximum SERS EFs of the nanostructures in liquid solution are less sensitive to the length of the nanostructures. This is manifested by the broader peaks in Figure 30 than those in Figure 28.

5.4 Summary

In conclusion, we have numerically investigated the SERS EFs in MIM structures with various geometrical shapes and sizes. Due to higher effective refractive index for the GSPPs in the SiO_2 spacer region, incident light tends to localize itself mostly in higher index region and thereby the light can be confined with a large optical field enhancement. By utilizing the GSPPs, we attained SERS EFs up to 10^{11} by the electromagnetic mechanism in the proposed nanostructure. Moreover, the nanostructures exhibit drop in SERS EFs when the thickness of the SiO_2 spacer increases. When the nanostructures are immersed in an aqueous solution, the maximum SERS EFs are achieved in smaller structures. In solution, very large ($> 10^{11}$) EFs can be attained over a broad range of size distribution in the nanostructures. The nanostructures investigated in this work can be easily fabricated by microelectronic fabrication techniques such as EBL, NSL and nanoimprint lithography. By utilizing GSPPs, we can achieve SERS hot spots with very large EFs at pre-determined locations on a substrate. Such nanostructures, with reproducible and low-cost fabrication, and large SERS EFs, are expected to be widely used as SERS-active substrates for optical sensing.

CHAPTER VI

INFRARED DIPOLE ANTENNA ENHANCED BY SURFACE PHONON POLARITONS

6.1 Introduction

The infrared (IR) detector is a photodetector that responds to infrared radiation, used in detecting fires, or overheating in machinery, planes, vehicles, and people, and in controlling temperature-sensitive industrial processes.[84] There have been two types of detectors such as thermal type and photon type.[85] Thermal type detects the infrared energy as heat and its photo sensitivity is independent of wavelength. It does not require cooling system but has slow response time and low detection capability. In contrast, photon type has high detection performance and fast response time but its sensitivity is dependent on wavelength. In addition, to achieve accurate measurement, temperatures much lower than room temperature provided by cryogenic cooling are required. The photon type IR detector systems allowing widespread usage can be simplified as well as reduced the cost and weight through avoiding cryogenic cooling. In general, the performance of IR detectors is limited by statistical nature of generation and recombination of charge carriers in the semiconductor. Cryogenic cooling has been used to suppress thermal generation to the lowest level possible. For practical purposes, the thermal generation must be reduced below the optical generation of electron and hole pairs. The detection of mid-infrared radiation, which is characterized by low photo energy, requires the electron transitions to be free-charge carriers of energy lower than the photon energy. Therefore, at room temperature, the thermal energy *kT* is comparable to the transition energy. As a result, this is a very high rate of thermal generation by the charge carriers.[86] A number of ways to improve detector's performance at near room temperature have been proposed.[87] Among the proposed ways a possible way is to use a suitable concentrator which compresses impinging infrared radiation.[88-91] Until now, an efficient possible way to obtain an effective concentration of IR radiation is to immerse the IR detector to the hemispherical or hyper-hemispherical lenses. However, fatal factors such as mechanical matching between detector and lens materials, and the small acceptable angle, have been limited to use immersion technology.

Surface plasmon polaritons (SPPs) are longitudinal surface charge waves accompanying electromagnetic fields localized an interface between a metal and a dielectric at the visible and near infrared region.[16] Most recently, metal nanostructures have received considerable attention for their ability to guide and manipulate SPPs at the nano-meter scale.[92] They have also offered many potential applications such as nanolithography, near field scanning optical microscopy (NSOM), spectroscopy, data storage, and bio-sensing. At lower frequencies (i.e., mid-infrared range), the plasmonic response of metal is either far weaker or nonexistent and SPP propagation constant is close to free space wave vector (k_0) at the light line. Recently, it has been introduced that SPPs have a counterpart in the infrared spectral region which is so-called surface phonon polaritons (SPhPs),[18] which has attracted much less attention than SPPs. SPhPs arise due to the coupling of the electromagnetic field to lattice vibrations of polar dielectrics at infrared frequencies. The physics of these excitations is conceptually in analogy to that of both propagation and localization of SPPs.

6.2 Optical Properties and Dispersion Relation of Silicon Carbide

Silicon carbide (SiC) is a material that has attracted interest due to its applications as a wide bandgap semiconductor used for high-temperature and high-power microelectronics.[93] Another interesting property of the material is its negative dielectric permittivity in the mid-infrared region of the spectrum between typically 10.3 and 12.6 μm as shown in Figure 31(a).[94] Here, Re(ε) is negative in the so-called *reststrahlen* band between the transverse (TO) and longitudinal (LO) optical-phonon frequencies, which gives rise to the excitation of SPhPs. Note that their damping characteristics given by Im(ε) can be much smaller than those for SPPs.

The dispersion relation for the wave vector of the SPhPs at the interface between SiC and air can be given by[95]

$$k_{SPhP}(\omega) = \frac{\omega}{c}\sqrt{\frac{\varepsilon_1(\omega)\varepsilon_2}{\varepsilon_1(\omega)+\varepsilon_2}} \tag{6.1}$$

where $k_{SPhP}(\omega)$ is the wave vector of surface phonon polaritons, $\varepsilon_1(\omega)$ and ε_2 are dielectric constants for SiC and air, respectively. As shown in Figure 31(b), we calculated dispersion relations of SPhPs and their propagation lengths at the SiC/air interface. SPhPs can only propagate close to the interface between two different media, and the amplitude of the fields decay exponentially with the distance from interface.

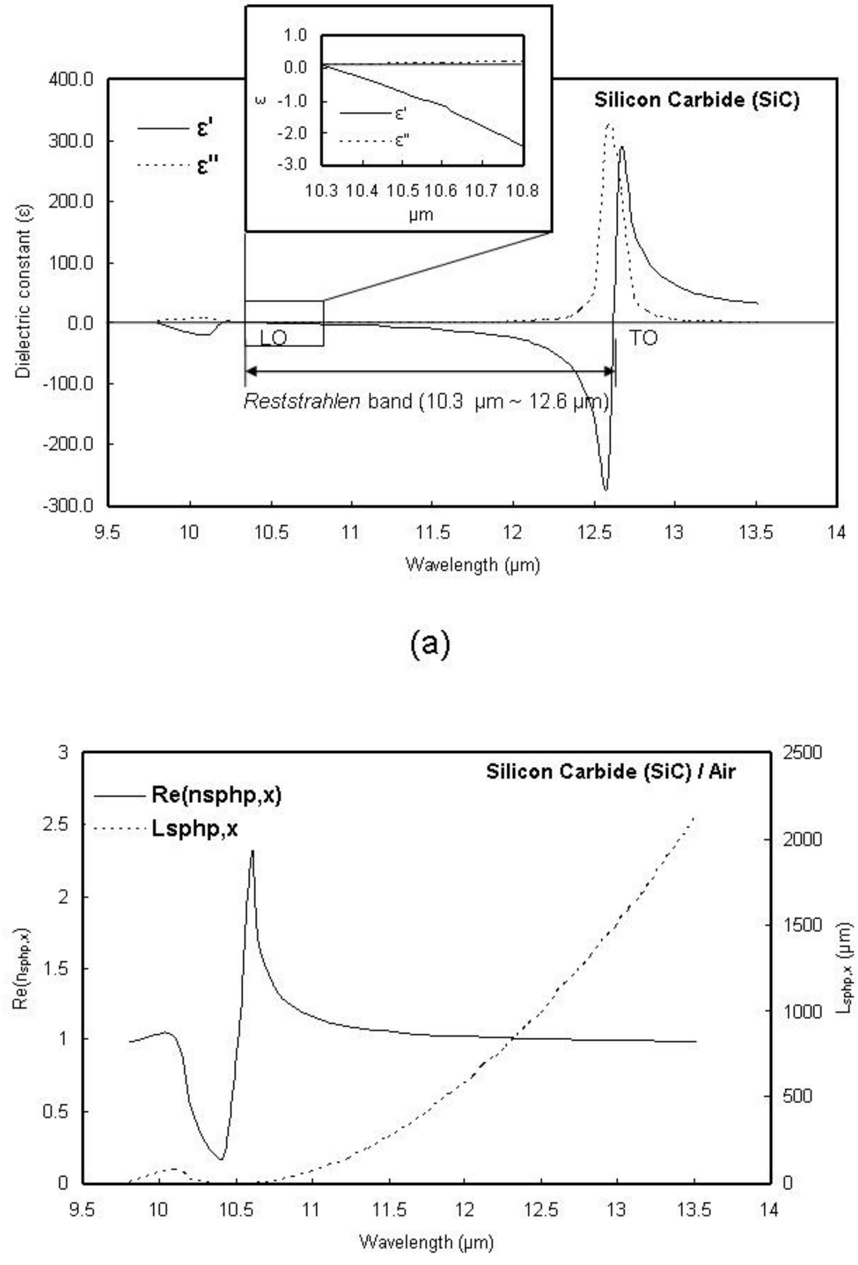

(a)

(b)

Figure 31 (a) Real and imaginary parts of the dielectric constant for SiC. (b) Real part of effective refractive index, Re($n_{sphp,x}$) and its propagation length, $L_{sphp,x}$ for surface phonon polaritons on the SiC/air interface calculated according to equation (6.1).

It is seen that resonant condition between two media is when Re[$\varepsilon_1(\omega)$]= – ε_2, and thus the maximum Re[n_{SPhP}] is at 10.55 μm, so-called resonant wavelength. It is also noted that the propagation length of SPhPs given by (2Im[k_{SPhP}])$^{-1}$ decreases with Re[n_{SPhP}] increasing. Here, effective refractive index of SPhPs is given by $n_{SPhP} = k_{SPhP} / k_0 = \left(k'_{SPhP} + ik''_{SPhP}\right) / k_0 = n'_{SPhP} + in''_{SPhP}$. Especially, real part of dielectric permittivity of SiC at wavelength of 10.6 μm used for all simulations in this study is Re(ε) = -1.15, which is close to resonance condition with air.[96]

6.3 Comparison with Other Polar Materials

Table 7 Comparison of real part of effective refractive index and propagation length of SPhPs at the interface between polar materials and air.

Materials	λ (μm)	ε	Re($n_{sphp,x}$)	$L_{sphp,x}$ (μm)
SiC	10.6	-1.15+i0.13	2.31	1.18
Al_2O_3	12.2	-1.06+i0.24	1.78	0.88
GaAs	34.6	-1.71+i0.78	1.31	10.28
CdTe	62.5	-3.31+i1.92	1.12	52.65
PbSe	50.0	-5.28+i4.78	1.05	72.09

As mentioned in the part of the SPPs, the best material for the excitation and propagation of the SPhPs should have the higher real part of effective refractive index and longer propagation length of the SPhPs at the interface between the polar material and dielectric. The effective refractive indices and propagation lengths of representative polar materials are shown in Table 7. Since SiC has the highest real part of the effective refractive index with reasonable propagation length, we select SiC as main material in our research. Further details are included in the Appendixes E and F.

6.4 Modeling and Simulation Methodology

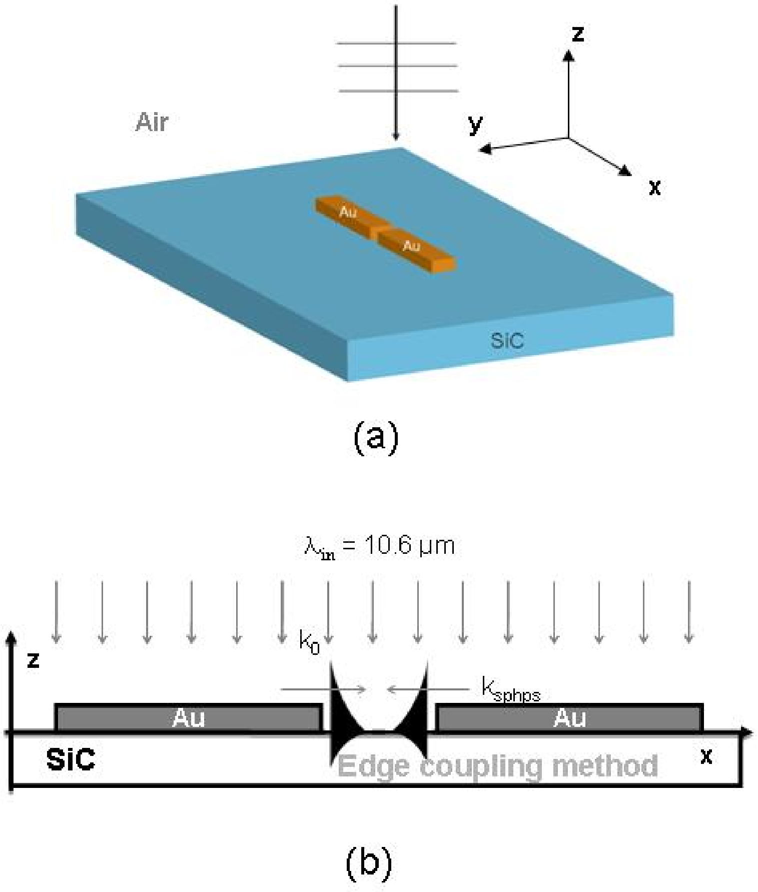

Figure 32 (a) Schematic diagram and (b) Field enhancement mechanism of an infrared dipole antenna enhanced by surface phonon polaritons.

The schematic diagram is presented in Figure 32(a). In order to utilize special optical properties of SPhPs in the mid-infrared region, we choose SiC as a substrate. Moreover, to account for a practical environment the antennas should be supported by a substrate. Optical energy can be coupled into surface polariton modes at discontinuities in the material.[97, 98] In this study, as shown in Figure 32(b), the edge of the gold dipole on the SiC substrate can excite SPhPs, which is so-called as the edge coupling method.[98, 99] In other word, when illuminated by mid-infrared radiation (i.e., 10.6 μm), the gold dipole antenna can support the conventional dipole antenna coupling and thereby at the end of dipole antenna edge, SPhPs can be excited. Hence, two coupling mechanism can give rise to large field enhancement.

We used 10.6 μm (fixed) as incident infrared radiation obtained from CO_2 lasers. The dielectric permittivity of gold and SiC at this wavelength is $\varepsilon_{Au} = -3128.7 + 1558.5i$ and $\varepsilon_{SiC} = -1.15 + 0.13i$, respectively,[46] and the infrared radiation to excite the SPhPs is a circularly polarized wave normally incident to the top of the dipole antenna. The intensity enhancement in the gap region of gold dipole antenna on various substrates, particularly SiC substrate at 10.2 μm (no SPhPs excitation), is simulated and analyzed by a 3D finite-difference time-domain (FDTD) method. Additionally, by modulating the geometrical parameters of dipole antenna, polarization of incident light and incident angles, the localized field confinement properties provided by resonant excitation of SPhPs are presented. The grid size used in this study is approximately 1/200λ, which can ensure the accuracy of the numerical study.

6.5 Results and Discussions

6.5.1 Dependence of substrates and incident wavelengths

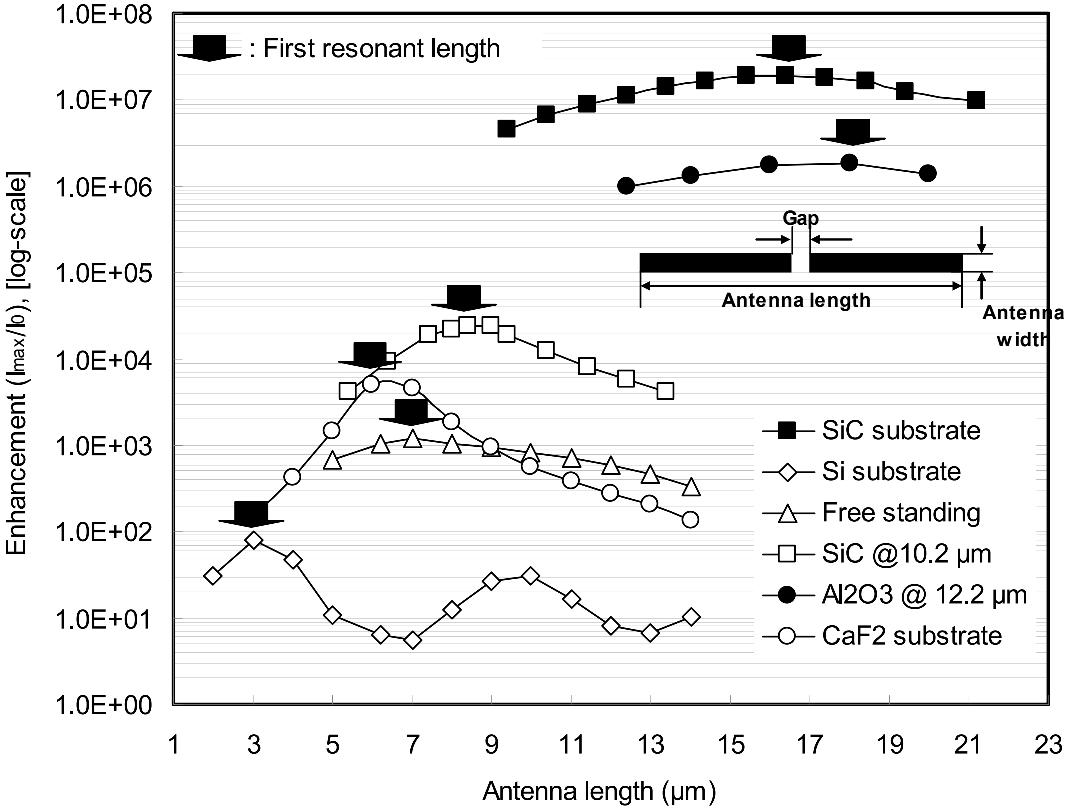

Figure 33 Intensity enhancement in free standing infrared antenna and infrared antennas on SiC, CaF_2 and Si substrates at 10.6 μm, and Al_2O_3 substrate at 12.2 μm. Intensity enhancement in infrared antenna on SiC substrate at 10.2 μm is much lower because no SPhPs can be excited at this wavelength.

An antenna is a device that establishes efficient coupling between the near-field and the far-field by use of impedance matching. Resonantly optical antennas can confine strongly optical near field in a subwavelength volume, which is recently demonstrated for dipole antennas and bow-tie antennas at the visible region.[100, 101] The geometry of the antenna strongly influences its optical properties, particularly at the field confinement.

Figure 33 shows the intensity enhancement in the gap region of the gold dipole antennas on SiC substrate as a function of antenna length. The corresponding dipole antennas have 100 nm in gap dimension, 100 nm in antenna thickness, and 400 nm in antenna width. When the antenna length increases, the dipole antenna clearly exhibits a linear increase of the field intensity until antenna length reaches the first resonant length. After that, the field intensity decreases gradually. The physical origin of this effect is connected to the coupling strength of the two antenna arms and excitation of SPhPs. The strong field enhancement is achieved by about 2×10^7 times at resonant antenna length of about 16.4 μm. Al_2O_3 substrate as another polar material exhibits analogous tendency and the maximum field enhancement is obtained by about 1.8×10^6 times at resonant antenna length of 18 μm. Since used incident wavelength of 12.2 μm to excite SPhPs, the resonance peak is shifted to the longer antenna length. Additionally, since Al_2O_3 has smaller real part of effective refractive index and shorter propagation length than those of SiC as shown in Table 7, the result of field enhancement is about an order of magnitude smaller than that of SiC. To verify the effect on the resonant excitation of SPhPs, the simulations are performed for the cases of dipole antenna on Si and CaF_2 substrate, free standing infrared antenna and dipole antenna on SiC substrate at 10.2 μm (no SPhPs excitation region) as shown in Figure 33. All parameters are identical with aforementioned gold dipole antenna on the SiC substrate. The maximum field enhancement of dipole antenna on SiC substrate at 10.2 μm in which SiC substrate has positive dielectric permittivity and does not support SPhPs is obtained by about 2×10^4 times at resonant antenna length. Likewise, the maximum field enhancements of dipole antenna on Si, CaF_2 and free standing infrared antenna are achieved by approximately 80, 5100 and 1200 times, respectively, at the resonant length. It is clearly seen that due to synergistic action of the dipole antenna and the resonant excitation of SPhPs, field enhancement in the gap region can reach more than four orders of magnitude higher than that of free standing dipole antenna. It is also noted that Si substrate (n_{Si} = 3.42 at 10.6 μm) antenna has much smaller the first resonant length than CaF_2 substrate (n_{CaF2} = 1.29 at 10.6 μm) and free standing antenna due to the substrate effect of higher refractive index.[102] Recent studies have shown that the resonant length of optical dipole antenna is 20% shorter than the value predicted by antenna theory. The antenna length of the optical antennas scales with the effective wavelength of the incident light.[103] Both Si substrate antenna and free standing antenna have the resonant lengths close to predicted values. Dipole antenna on SiC substrate, however, has the resonant length larger than predicted value. In our view, it appears that the field enhancement originates not only from dipole antenna coupling but also from the resonant excitation of SPhPs between the incident infrared radiation and electromagnetic surface modes when negative dielectric permittivity provided by lattice vibrations in polar crystals.

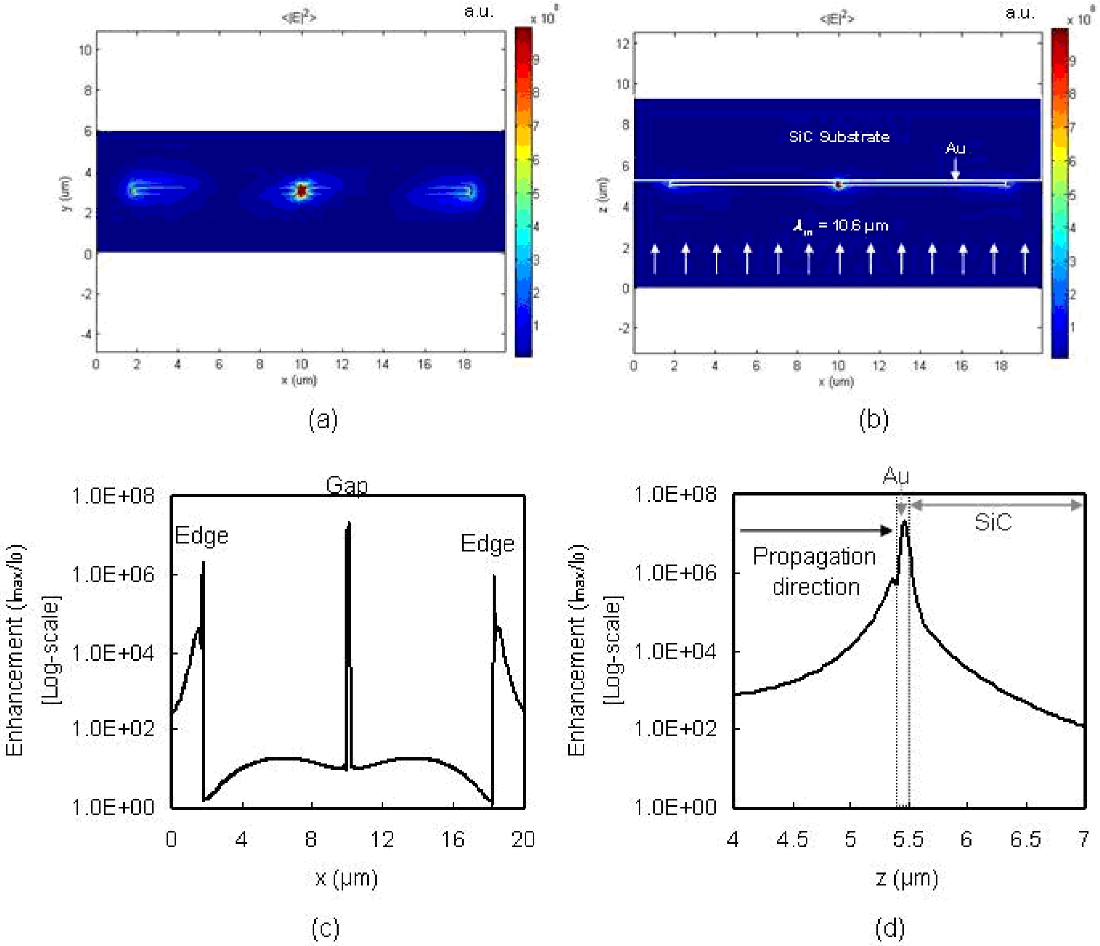

Figure 34 Field distribution in (a) xy-plane, (b) xz-plane, (c) along x-direction, and (d) along z-direction.

To illustrate the strong field confinement in the antenna gap at the condition of maximum field enhancement, Figure 34(a) and (b) show field distributions in the xy- and xz-planes through the gap for a gold dipole antenna on the SiC substrate. It is clearly seen that the field intensity is strongly localized across the antenna, especially at the gap and edges of the antenna as shown in Figure 34(c). The intensity in the gap region of the dipole antenna is over an order higher than at the edges of the antenna. The dipole antenna can provide optical field confinement of λ/60 (i.e., FWHM (full width at half maximum) = 175 nm). In Figure 34(d), the plot shows that the enhanced field is bound in the gold gap region, which is related to the property of surface polaritons. As described above, the electromagnetic energy density of surface polaritons falls off evanescently with distance from the surface.

6.5.2 Influence of geometrical parameters of dipole antenna

Simulations are also performed to evaluate the effect of geometrical parameters as shown in Figure 35. The corresponding dipole antenna has 16.4 μm in antenna length and all other parameters used are identical with when maximum field enhancement was achieved. Among them, the field enhancement of the dipole antenna obviously depends on its gap dimension: decreasing the gap dimension increases rapidly the antenna intensity, particularly at narrower gap dimension, as shown in Figure 35(a).[104]

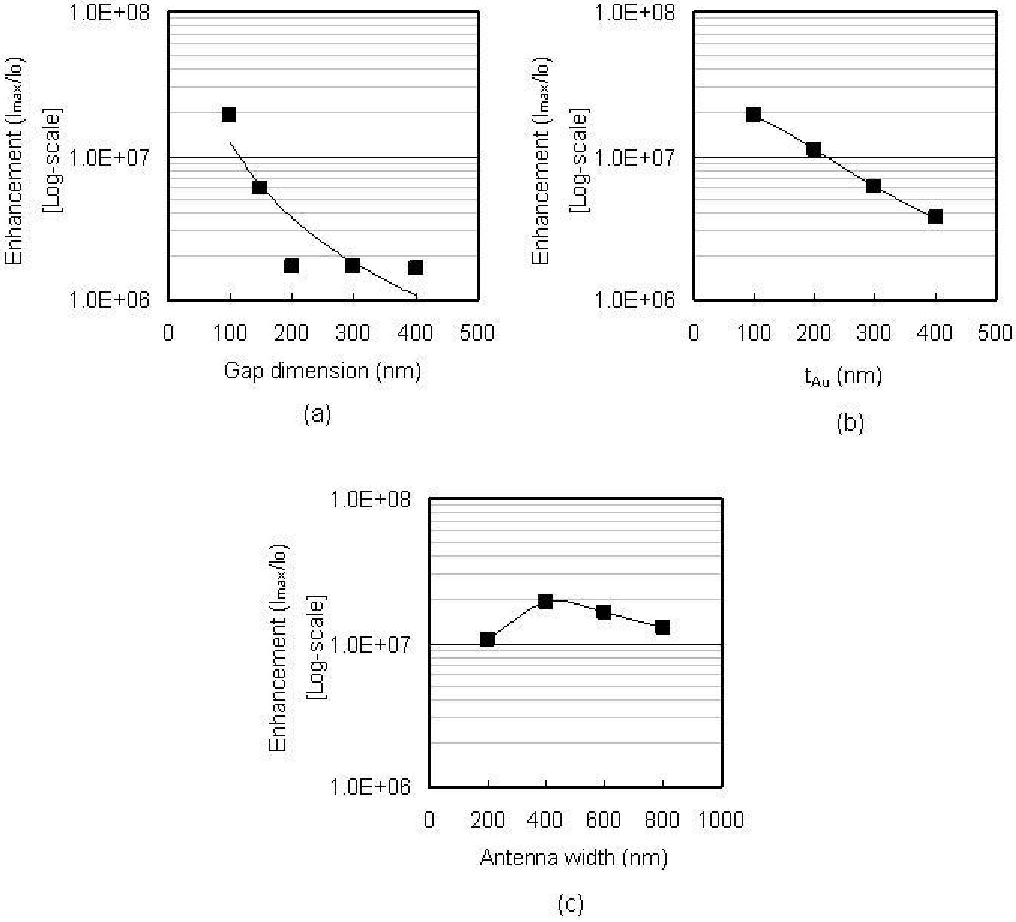

Figure 35 Field enhancement as a function of (a) gap dimension, (b) antenna thickness, and (c) antenna width.

Recently, Novotny demonstrated that among the antenna parameters the antenna thickness affects the effective wavelength that provides the resonant length of optical dipole antenna.[103] The effective wavelength is linearly proportional to the thickness of the antenna. Figure 35(b) shows the antenna thickness vs. field enhancement. The field enhancement decreases steadily with the antenna thickness increasing due to fixed resonant length. The effect of antenna width is also verified as shown in Figure 35(c). The filed enhancement is not significantly varied with the antenna width changing. The maximum field enhancement is achieved at 400 nm of antenna width.

6.5.3 Dependence of polarizations and angles of incident light

It is well known that the p-polarized incident wave can only provide the excitation of the SPPs. The dependency of polarized illumination is shown in Figure 36. Excitation of SPhPs in the p-polarized incident wave is observed. However, since no excitation of SPhPs in the s-polarized incident wave, significant field enhancement in the gap region of gold dipole antenna is not observed. It is evident that the physics of excitations of SPhPs is conceptually in analogy to that of SPPs.

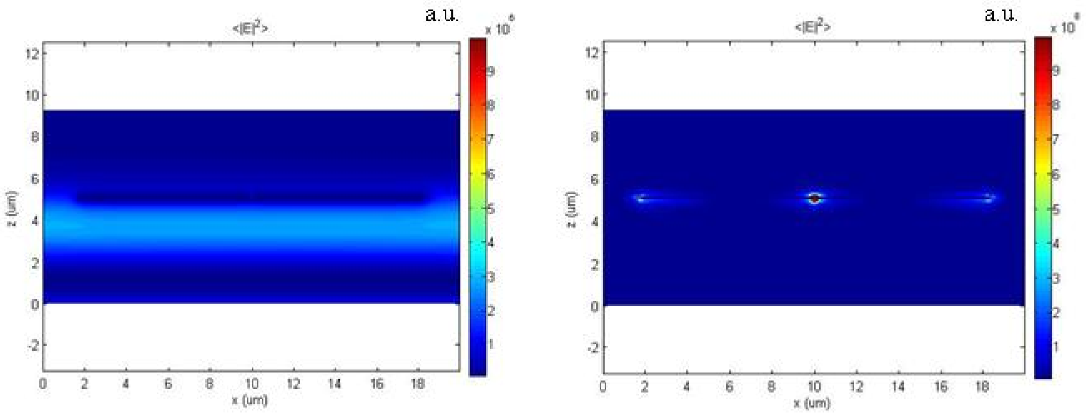

(a)

(b)

Figure 36 Field distribution in xz-plane as function of polarization of incident infrared radiation: (a) s-polarization and (b) p-polarization.

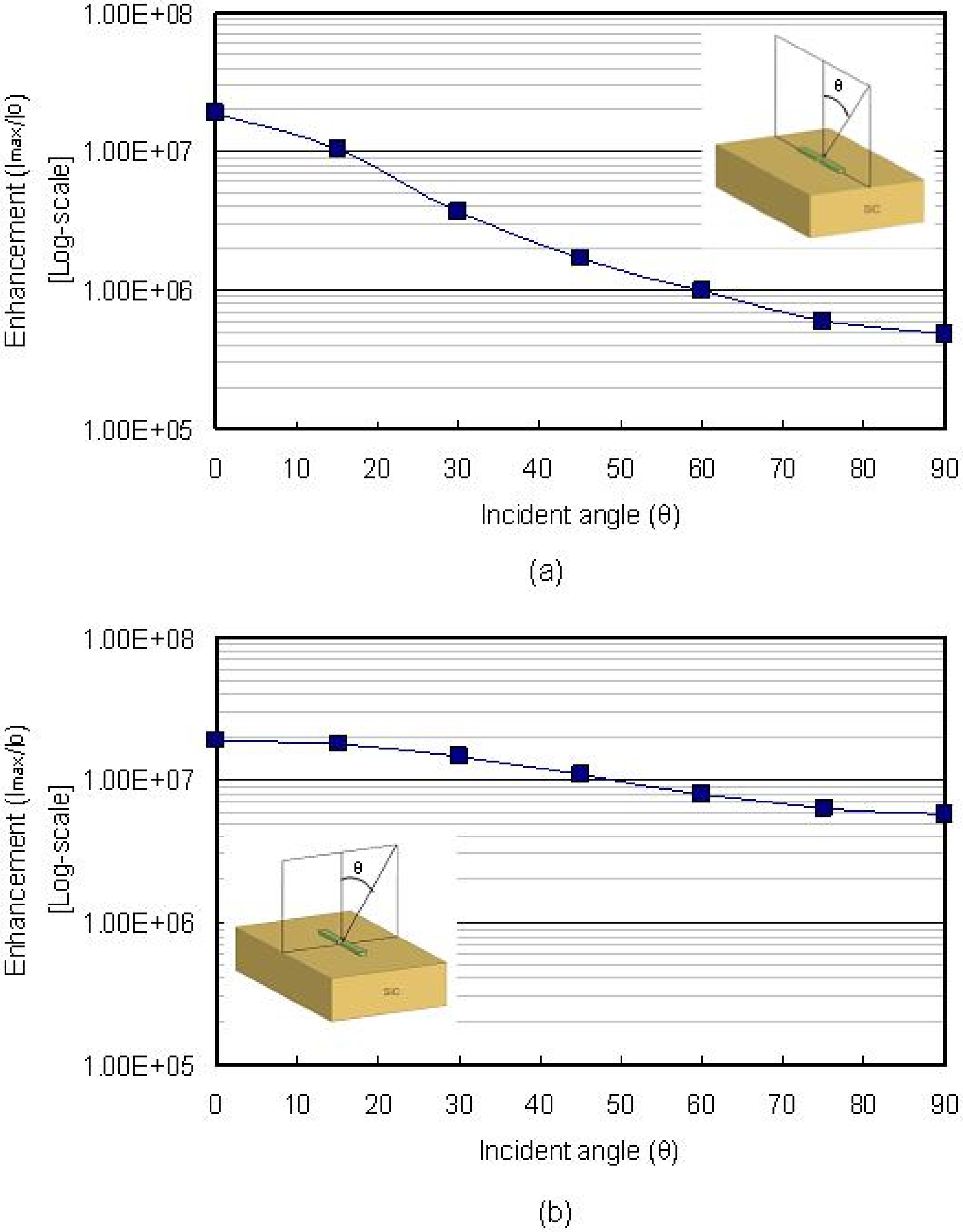

(a)

(b)

Figure 37 Field enhancement as a function of incident angle: (a) along the antenna length, and (b) along the antenna width.

Figure 37(a) and (b) show the field enhancement in the gap region of gold dipole antenna at the different incident angles from θ = 0° to θ = 90°, along antenna width and along antenna length, respectively. The field enhancement decreases with an increasing value of θ. The lowest field enhancement is achieved at the illumination of θ = 90° along antenna length. The value is about 4.8×10^5 which is much higher than those of above-mentioned dipole antennas having no SPhPs excitation. Therefore, this device can be used to the independent applications for incident angles.

6.6 Summary

We have numerically investigated the optical field enhancement by utilizing SPhPs phenomenon in the mid-infrared region. SPhPs on the SiC substrate are the coupling between incident radiation and lattice vibrations that can be resonantly excited in the mid-infrared wavelengths between 10.3 to 12.6 μm. Due to the synergistic action of the dipole antenna and the resonant excitation of SPhPs, strong field enhancement in the gap region of the gold dipole antenna on the SiC substrate reaches a value that is more than four orders of magnitude higher than that of free standing infrared dipole antenna. Among the geometrical parameters, the field enhancement relies strongly on the gap dimension and the resonant length depends significantly on the antenna thickness. Additionally, the dependence of incident polarization and angles was investigated. The p-polarized incident wave could only support SPhPs and strong field enhancement was achieved even in parallel illumination to the SiC substrate. This strong field confinement is expected to find promising applications in bio-molecular sensing and highly sensitive photo-detectors.

CHAPTER VII

CONCLUSION

Surface plasmon polaritons, which is the collective oscillation of electron density on metallic surfaces, have attracted great interest because they exhibit the novel properties such as extraordinary optical transmission (good for superlensing), smaller wavelength than the incident light (good for high resolution near-field scanning optical microscopy and subwavelength imaging), higher electric field confinement on the metal surface (good for surface-enhanced Raman spectroscopy), plasmonic chips by merging photonics and electronics (good for high data rate processing and effective sensing applications), and two-dimensional waves (good for plasmonic waveguides).

As one of the applications using extraordinary optical transmission, we have investigated a plasmonic zone plate lens. A variety of applications, such as maskless lithography, scanning optical microscopy, optical data storage, and optical antenna, desire high intensity light beams narrower than diffraction limit. As a trade-off between resolution and working distance, we designed and analyzed a metallic-dielectric-air structured plasmonic zone plate lens which has a sub-diffraction limit spot with high intensity. The smaller spot size is mainly attributed to the narrower zone width, and the higher transmission is related to extraordinary optical transmission. In order to interpret the phenomenon of extraordinary optical transmission, we calculated the complex propagation constant affected by the dielectric filling in the zones and surface plasmon resonance in the metal. The increased complex propagation constant in the narrower zone widths gives rise to the extraordinary optical transmission. Finally, our proposed device, with its high NA (> 1), reasonable focal length (λ - 5λ), high transmission, and low cost of fabrication, is expected to find promising applications.

On the other hand, even though the uncommon property of extraordinary optical transmission is applied to the proposed device above, the resulted diffraction efficiency of this device is relatively low (typically less than a few percent), not comparable to far-field devices. Therefore, a method to obtain further higher optical field enhancement in the plasmonic zone plate lens has been proposed. By using metal/dielectric multilayered zone plate, optical field enhancement at the focal point originates not only from SPPs-assisted diffraction along the traveling direction of incident light, but also from the coupling and multiple scattering of surface plasmons in the multilayered zone plate. In order to obtain the maximum transmission efficiency in the multilayered zone plate, the imaginary part of the calculated complex propagation constant, governing the decay length of surface plasmons in the multilayered zone plate, should be considered. This optical field enhancement, about an order of magnitude higher than that of conventional zone plate, is expected to offer significant potentials in many applications such as zone plate microscopy, optical antenna, optical sensors, and nano-optics devices.

Surface plasmons are often categorized into two classes such as propagating surface plasmons and localized surface plamons. Propagating surface plasmons are propagating surface electromagnetic waves bound to the interface between a metal and a dielectric. On the other hand, localized surface plasmons are non-propagating excitations of the electrons in metal nano-particles which are much smaller than the incident light.

We have demonstrated enhanced localized surface plasmons coupled with gap surface plasmon polaritons. Due to higher effective refractive index generated by tiny dielectric gap underneath metal nano-particle, incident lights tend to localize itself mostly in the medium with higher refractive index than its adjacent ones and thereby the lights can confine with larger optical field enhancement. By utilizing gap surface plamson polaritons, the hot-spots to be created at pre-determined locations as well as higher maximum SERS EF can be also controlled. Attained larger SERS EF is expected to be used in promising applications such as SERS-active substrates and optical biosensors.

Optical antennas allow for efficient conversion of propagating light into sub-wavelength volume confined and strongly enhanced optical fields. The local field enhancement can be significantly increased by optical near-field coupling with nano-structures. In the mid-infrared region, surface phonon polarions excited on the surface of polar materials such as SiC and Al_2O_3 are the coupling between incident radiation and lattice vibrations that can be resonantly excited in the *reststrahlen* band of negative Re(ε).

Due to the synergistic action of the dipole antenna and the resonant excitation of surface phonon polaritons, strong field enhancement in the gap region of the gold dipole antenna formed on the SiC substrate reaches a value that is more than four orders of magnitude higher than that of free standing gold dipole antenna. This strongly localized electromagnetic field, resonantly coupled to the molecular vibrations, provides sufficient enhancement to be used as a sensitive spectroscopic tool (i.e., surface-enhanced infrared absorption spectroscopy) for straightforward identification of molecular species and also it can be used highly sensitive photo-detectors.

REFERENCES

1. R. Zia, J. A. Schuller, A. Chandran, and M. L. Brongersma, "Plasmonics: The next chip-scale technology," Mater. Today **9**, 20-27 (2006).

2. L. Novotny and B. Hecht, *Principles of nano-optics* (Cambridge University Press, Cambridge, England, 2006).

3. E. Abbe, "Beitrage zur theorie des mikroskops und der mikroskopichen warrnehmung," Archiv. f. Mikroscopische Anat. **9**, 413-468 (1873).

4. K. Kneipp, M. Moskovits, and H. Kneipp, *Surface-enhanced Raman scattering physics and applications* (Springer, New York, 2006).

5. R. A. Tripp, R. A. Dluhy, and Y. Zhao, "Novel nanostructures for SERS biosensing," Nano Today **3**, 31-37 (2008).

6. E. Johnson and R. Aroca, "Surface-enhanced infrared spectroscopy of monolayers," J. Phys. Chem. **99**, 9325-9330 (1995).

7. M. S. Anderson, "Enhanced infrared absorption with dielectric nanoparticles," Appl. Phys. Lett. **83**, 2964-2966 (2003).

8. A. Rasmussen and V. Deckert, "New dimension in nano-imaging: breaking through the diffraction limit with scanning near-field optical microscopy," Anal. Bioanal. Chem. **381**, 165-172 (2005).

9. E. H. Synge, "A suggested method for extending microscopic resolution into ultramicroscopic region," Philos. Mag. **6**, 356-362 (1928).

10. P. R. H. Stark, A. E. Halleck, and D. N. Larson, "Breaking the diffraction barrier outside of the optical near-field with bright, collimated light from nanometric apertures," Prod. Natl. Acad. Sci. USA **104**, 18902-18906 (2007).

11. D. W. Pohl, W. Denk, and M. Lanz, "Optical stethoscopy: Image recording with resolution lambda/20," Appl. Phys. Lett. **44**, 651-653 (1984).

12. E. Betzig and J. K. Trautman, "Near-field optics: Microscopy, spectroscopy, and surface modification beyond the diffraction limit," Science **257**, 189-195 (1992).

13. M. Ohtsu and K. Kobayashi, *Optical near fields* (Springer, New York, 2006).

14. E. C. L. Ru and P. G. Etchegoin, *Principles of surface-enhanced Raman spectroscopy and related plasmonic effects* (Elsevier, Oxford, 2009).

15. M. Dragoman and D. Dragoman, "Plasmonics: Applications to nanoscale terahertz and optical devices," Prog. Quant. Electon. **32**, 1-41 (2008).

16. H. Raether, *Surface plasmons on smooth and rough surfaces and on gratings* (Springer-Verlag, Berlin, 1988).

17. T. W. Ebbesen, H. J. Lezec, H. F. Ghaemi, T. Thio, and P. A. Wolff, "Extraordinary optical transmission through sub-wavelength hole arrays," Nature (London) **391**, 667-669 (1998).

18. S. A. Maier, *Plasmonics: Fundamentals and applications* (Springer, New York, 2007).

19. Q. Zhou, Y. Chao, Y. Li, W. Xu, Y. Wu, and J. Zheng, "Contribution of charge-transfer mechanisms to surface-enhanced Raman scattering with near-IR excitation," ChemPhysChem **8**, 921-925 (2007).

20. D3 Technologies Ltd. accessed on http://www.d3technologies.co.uk and therein What is SERS?

21. K. A. Willets and R. P. Van Duyne, "Localized surface plasmon resonance spectroscopy and sensing," Annu. Rev. Phys. Chem. **58**, 267-297 (2007).

22. M. E. Stewart, C. R. Anderton, L. B. Thompson, J. Maria, S. K. Gray, J. A. Rogers, and R. G. Nuzzo, "Nanostructured plasmonic sensors," Chem. Rev. **108**, 494-521 (2008).

23. J. P. Camden, J. A. Dieringer, J. Zhao, and R. P. Van Duyne, "Controlled plasmonic nanostructures for surface-enhanced spectroscopy and sensing," Acc. Chem. Res. **41**, 1653-1661 (2008).

24. A. Campion and P. Kambhampati, "Surface-enhanced Raman scattering," Chem. Soc. Rev. **27**, 241-250 (1998).

25. K. Kneipp, H. Kneipp, I. Itzkan, R. R. Dasari, and M. S. Feld, "Surface-enhanced Raman scattering and biophysics," J. Phys.: Condens. Matter. **14**, R597-R624 (2002).

26. M. Fox, *Optical properties of solids* (Oxford University Press, Oxford, 2001).

27. R. Aroca, *Surface-enhanced vibrational spectroscopy* (Wiley, Chichester, UK, 2006).

28. Y. Kane, "Numerical solution of initial boundary value problems involving Maxwell's equations in isotropic media," Antennas and Propagation, IEEE Transactions on **14**, 302-307 (1966).

29. A. Wong and T. Pistor, *TEMPEST version 6.0 user guide* (Electronics Research Laboratory, University of California, Berkeley, 2000).

30. H. I. Smith, "A proposal for maskless, zone-plate-array nanolithography," J. Vac. Sci. Technol. B **14**, 4318-4322 (1996).

31. I. J. Djomehri, T. A. Savas, and H. I. Smith, "Zone-plate-array lithography in the deep ultraviolet," J. Vac. Sci. Technol. B **16**, 3426-3429 (1998).

32. D. Chao, A. Patel, T. Barwicz, H. I. Smith, and R. Menon, "Immersion zone-plate-array lithography," J. Vac. Sci. Technol. B **23**, 2657-2661 (2005).

33. D. T. Attwood, *Soft X-rays and extreme ultraviolet radiation, principles and applications* (Cambridge U. Press, Cambridge, N.Y., 1999), pp. 337-394.

34. A. N. Kurokhtin and A. V. Popov, "Simulation of high-resolution x-ray zone plates," J. Opt. Soc. Am. A **19**, 315-324 (2002).

35. H. A. Bethe, "Theory of diffraction by small holes," Phys. Rev. **66**, 163-182 (1944).

36. J. A. Porto, F. J. Garcia-Vidal, and J. B. Pendry, "Transmission resonances on metallic gratings with very narrow slits," Phys. Rev. Lett. **83**, 2845-2848 (1999).

37. H. J. Lezec, A. Degiron, E. Devaux, R. A. Linke, L. Martin-Moreno, F. J. Garcia-Vidal, and T. W. Ebbesen, "Beaming light from a subwavelength aperture," Science **297**, 820-822 (2002).

38. P. Lalanne, J. P. Hugonin, and J. C. Rodier, "Theory of surface plasmon generation at nanoslit apertures," Phys. Rev. Lett. **95**, 263902-263904 (2005).

39. S. Seo, H. C. Kim, H. Ko, and M. Cheng, "Subwavelength proximity nanolithography using a plasmonic lens," J. Vac. Sci. Technol. B **25**, 2271-2276 (2007).

40. Z. Liu, J. M. Steele, W. Srituravanich, Y. Pikus, C. Sun, and X. Zhang, "Focusing surface plasmons with a plasmonic lens," Nano Lett. **5**, 1726-1729 (2005).

41. Y. Fu, W. Zhou, L. E. N. Lim, C. L. Du, and X. G. Luo, "Plasmonic microzone plate: Superfocusing at visible regime," Appl. Phys. Lett. **91**, 061124-061123 (2007).

42. E. Popov, M. Neviere, A.-L. Fehrembach, and N. Bonod, "Enhanced transmission of light through a circularly structured aperture," Appl. Opt. **44**, 6898-6904 (2005).

43. C. Genet and T. W. Ebbesen, "Light in tiny holes," Nature (London) **445**, 39-46 (2007).

44. M. H. Horman, "Efficiences of zone plates and phase zone plates," Appl. Opt. **6**, 2011-2013 (1967).

45. H. X. Yuan, B. X. Xu, H. F. Wang, and T. C. Chong, "Field enhancement of nano-sized metal aperture with and without surrounding corrugations through resonant surface plasmons," Jpn. J. Appl. Phys. **45**, 787-791 (2006).

46. E. D. Palik, *Handbook of optical constants of solids* (Academic, New York, 1985).

47. C.-P. Huang and Y.-Y. Zhu, "Plasmonics: Manipulation light at the subwavelength scale," Active Passive Electron. Compon. **2007**, 1-13 (2007).

48. R. Gordon and A. Brolo, "Increased cut-off wavelength for a subwavelength hole in a real metal," Opt. Express **13**, 1933-1938 (2005).

49. H. Shi, C. Wang, C. Du, X. Luo, X. Dong, and H. Gao, "Beam manipulating by metallic nano-slits with variant widths," Opt. Express **13**, 6815-6820 (2005).

50. J. D. J. Stigliani, R. Mittra, and R. G. Semonin, "Resolving power of a zone plate," J. Opt. Soc. Am. **57**, 610-613 (1967).

51. J.-A. Sun and A. Cai, "Archaic focusing properties of Fresnel zone plates," J. Opt. Soc. Am. A **8**, 33-35 (1991).

52. R. G. Mote, S. F. Yu, B. K. Ng, W. Zhou, and S. P. Lau, "Near-field focusing properties of zone plates in visible regime - New insights," Opt. Express **16**, 9554-9564 (2008).

53. Y. Fu, W. Zhou, and L. E. N. Lim, "Near-field behavior of zone-plate-like plasmonic nanostructures," J. Opt. Soc. Am. A **25**, 238-249 (2008).

54. H. C. Kim, H. Ko, and M. Cheng, "Optical focusing of plasmonic Fresnel zone plate-based metallic structure covered with a dielectric layer," J. Vac. Sci. Technol. B **26**, 2197-2203 (2008).

55. E. Ozbay, "Plasmonics: Merging photonics and electronics at nanoscale dimensions," Science **311**, 189-193 (2006).

56. Z. H. Tang, R. W. Peng, Z. Wang, X. Wu, Y. J. Bao, Q. J. Wang, Z. J. Zhang, W. H. Sun, and M. Wang, "Coupling of surface plasmons in nanostructured metal/dielectric multilayers with subwavelength hole arrays," Phys. Rev. B **76**, 195405-195408 (2007).

57. J. M. Steele, Z. Liu, Y. Wang, and X. Zhang, "Resonant and non-resonant generation and focusing of surface plasmons with circular gratings," Opt. Express **14**, 5664-5670 (2006).

58. D.-Z. Lin, C.-H. Chen, C.-K. Chang, T.-D. Cheng, C.-S. Yeh, and C.-K. Lee, "Subwavelength nondiffraction beam generated by a plasmonic lens," Appl. Phys. Lett. **92**, 233106-233103 (2008).

59. C. Liu, N. Chen, and C. Sheppard, "Nanoillumination based on self-focus and field enhancement inside a subwavelength metallic structure," Appl. Phys. Lett. **90**, 011501-011503 (2007).

60. P. K. Tien, "Integrated optics and new wave phenomena in optical waveguides," Rev. Mod. Phys. **49**, 361-420 (1977).

61. B. Ung and Y. Sheng, "Mechanism of coupling and interference in nano-slit," Proc. SPIE **6832**, 68320E-68328 (2007).

62. J. Park, H. Kim, I.-M. Lee, S. Kim, J. Jung, and B. Lee, "Resonant tunneling of surface plasmon polariton in the plasmonic nano-cavity," Opt. Express **16**, 16903-16915 (2008).

63. K. Kneipp, Y. Wang, H. Kneipp, L. T. Perelman, I. Itzkan, R. R. Dasari, and M. S. Feld, "Single molecule detection using surface-enhanced Raman scattering (SERS)," Phys. Rev. Lett. **78**, 1667-1670 (1997).

64. S. Nie and S. R. Emory, "Probing single molecules and single nanoparticles by surface-enhanced Raman scattering," Science **275**, 1102-1106 (1997).

65. E. Hao and G. C. Schatz, "Electromagnetic fields around silver nanoparticles and dimers," J. Chem. Phys. **120**, 357-366 (2004).

66. X. M. Qian and S. M. Nie, "Single-molecule and single-nanoparticle SERS: From fundamental mechanisms to biomedical applications," Chem. Soc. Rev. **37**, 912-920 (2008).

67. P. L. Stiles, J. A. Dieringer, N. C. Shah, and R. P. Van Duyne, "Surface-enhanced Raman spectroscopy," Annu. Rev. Anal. Chem. **1**, 601-626 (2008).

68. S. B. Chaney, S. Shanmukh, R. A. Dluhy, and Y. P. Zhao, "Aligned silver nanorod arrays produce high sensitivity surface-enhanced Raman spectroscopy substrates," Appl. Phys. Lett. **87**, 031908-031903 (2005).

69. A. Tao, F. Kim, C. Hess, J. Goldberger, R. He, Y. Sun, Y. Xia, and P. Yang, "Langmuir-Blodgett silver nanowire monolayers for molecular sensing using surface-enhanced Raman spectroscopy," Nano Lett. **3**, 1229-1233 (2003).

70. D. A. Genov, A. K. Sarychev, V. M. Shalaev, and A. Wei, "Resonant field enhancements from metal nanoparticle arrays," Nano Lett. **4**, 153-158 (2004).

71. G. Gantzounis, N. Stefanou, and N. Papanikolaou, "Optical properties of periodic structures of metallic nanodisks," Phys. Rev. B **77**, 035101-035107 (2008).

72. J. Beermann, S. M. Novikov, T. Sodergaard, A. Boltasseva, and S. I. Bozhevolnyi, "Two-photon mapping of localized field enhancements in thin nanostrip antennas," Opt. Express **16**, 17302-17309 (2008).

73. S. I. Bozhevolnyi and T. Sodergaard, "General properties of slow-plasmon resonant nanostructures: nano-antennas and resonators," Opt. Express **15**, 10869-10877 (2007).

74. J. Jung, T. Sondergaard, and S. I. Bozhevolnyi, "Gap plasmon-polariton nanoresonators: Scattering enhancement and launching of surface plasmon polaritons," Phys. Rev. B **79**, 035401-035408 (2009).

75. Y. Chu and K. B. Crozier, "Experimental study of the interaction between localized and propagating surface plasmons," Opt. Lett. **34**, 244-246 (2009).

76. H. C. Kim, H. Ko, and M. Cheng, "High efficient optical focusing of a zone platecomposed of metal/dielectric multilayer," Opt. Express **17**, 3078-3083 (2009).

77. S. O. Kucheyev, J. R. Hayes, J. Biener, T. Huser, C. E. Talley, and A. V. Hamza, "Surface-enhanced Raman scattering on nanoporous Au," Appl. Phys. Lett. **89**, 053102-053103 (2006).

78. L. H. Qian, A. Inoue, and M. W. Chen, "Large surface enhanced Raman scattering enhancements from fracture surfaces of nanoporous gold," Appl. Phys. Lett. **92**, 093113-093113 (2008).

79. J. Fang, Y. Yi, B. Ding, and X. Song, "A route to increase the enhancement factor of surface enhanced Raman scattering (SERS) via a high density Ag flower-like pattern," Appl. Phys. Lett. **92**, 131115-131113 (2008).

80. G. Della Valle, T. Sondergaard, and S. I. Bozhevolnyi, "Plasmon-polariton nano-stripresonators: From visible to infra-red," Opt. Express **16**, 6867-6876 (2008).

81. C. L. Haynes, A. D. McFarland, L. Zhao, R. P. Van Duyne, G. C. Schatz, L. Gunnarsson, J. Prikulis, B. Kasemo, and M. Kall, "Nanoparticle optics: The importance of radiative dipole coupling in two-dimensional nanoparticle arrays," J. Phys. Chem. B **107**, 7337-7342 (2003).

82. C. L. Haynes and R. P. Van Duyne, "Plasmon-sampled surface-enhanced Raman excitation spectroscopy," J. Phys. Chem. B **107**, 7426-7433 (2003).

83. M. Futamata, "Single molecule sensitivity in SERS: importance of junction of adjacent Ag nanoparticles," Faraday Discuss. **132**, 45-61 (2006).

84. D. I. Promish, "Photodetecting apparatus having cryo-genic cooling and flushing means," U.S. Patent No. 3,258,602 (1968).

85. A. Rogalski, "Infrared detectors: Status and trends," Prog. Quant. Electon. **27**, 59-210 (2003).

86. J. Piotrowski and A. Rogalski, *High-operating-temperature infrared photodetectors* (SPIE, Bellingham, 2007).

87. J. Piotrowski and A. Rogalski, "Uncooled long wavelength infrared photon detectors," Infrared Phys. Technol. **46**, 115-131 (2004).

88. J. E. Slawek Jr and H. H. Randall, "Optical immersion of HgCdTe photoconductive detectors," Infrared Phys. **15**, 339-340 (1975).

89. N. T. Gordon, "Design of Hg1-xCdxTe infrared detector arrays using optical immersion with microlenses to achieve a higher operating temperature," Semicon. Sci. Technol. **6**, C106-C109 (1991).

90. M. E. Motamedi, W. E. Tennant, H. O. Sankur, R. Melendes, N. S. Gluck, S. Park, J. M. Arias, J. Bajaj, J. G. Pasko, W. V. McLevige, M. Zandian, R. L. Hall, and P. D. Richardson, "Micro-optic integration with focal plane arrays," Opt. Eng. **36**, 1374-1381 (1997).

91. J. Piotrowski, W. Galus, and M. Grudzien, "Near room-temperature IR photo-detectors," Infrared Phys. **31**, 1-48 (1991).

92. W. L. Barnes, A. Dereux, and T. W. Ebbesen, "Surface plasmon subwavelength optics," Nature (London) **424**, 824-830 (2003).

93. C. Rockstuhl, M. G. Salt, and H. P. Herzig, "Analysis of the phonon-polariton response of silicon carbide microparticles and nanoparticles by use of the boundary element method," J. Opt. Soc. Am. B **22**, 481-487 (2005).

94. N. Ocelic and R. Hillenbrand, "Subwavelength-scale tailoring of surface phonon polaritons by focused ion-beam implantation," Nat. Mater. **3**, 606-609 (2004).

95. P. B. Catrysse and S. Fan, "Near-complete transmission through subwavelength hole arrays in phonon-polaritonic thin films," Phys. Rev. B **75**, 075422-075425 (2007).

96. J. Renger, S. Grafstrom, L. M. Eng, and R. Hillenbrand, "Resonant light scattering by near-field-induced phonon polaritons," Phys. Rev. B **71**, 075410-075417 (2005).

97. A. V. Zayats, I. I. Smolyaninov, and A. A. Maradudin, "Nano-optics of surface plasmon polaritons," Phys. Rep. **408**, 131-314 (2005).

98. A. J. Huber, B. Deutsch, L. Novotny, and R. Hillenbrand, "Focusing of surface phonon polaritons," Appl. Phys. Lett. **92**, 203104-203103 (2008).

99. A. Huber, N. Ocelic, D. Kazantsev, and R. Hillenbrand, "Near-field imaging of mid-infrared surface phonon polariton propagation," Appl. Phys. Lett. **87**, 081103-081103 (2005).

100. P. Muhlschlegel, H. J. Eisler, O. J. F. Martin, B. Hecht, and D. W. Pohl, "Resonant optical antennas," Science **308**, 1607-1609 (2005).

101. A. Sundaramurthy, P. J. Schuck, N. R. Conley, D. P. Fromm, G. S. Kino, and W. E. Moerner, "Toward nanometer-scale optical photolithography: Utilizing the near-field of bowtie optical nanoantennas," Nano Lett. **6**, 355-360 (2006).

102. K. B. Crozier, A. Sundaramurthy, G. S. Kino, and C. F. Quate, "Optical antennas: Resonators for local field enhancement," J. Appl. Phys. **94**, 4632-4642 (2003).

103. L. Novotny, "Effective wavelength scaling for optical antennas," Phys. Rev. Lett. **98**, 266802-266804 (2007).

104. H. Fischer and O. J. F. Martin, "Engineering the optical response of plasmonic nanoantennas," Opt. Express **16**, 9144-9154 (2008).

APPENDIX A

OPTICAL PROPERTIES OF HIGHLY CONDUCTIVE METALS

A.1. Copper (Cu)

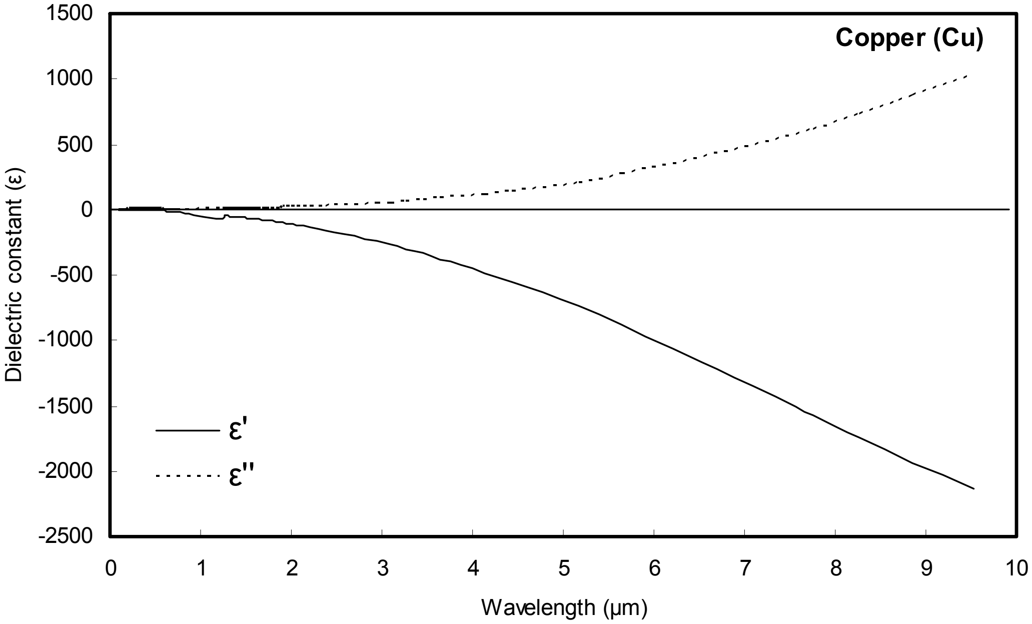

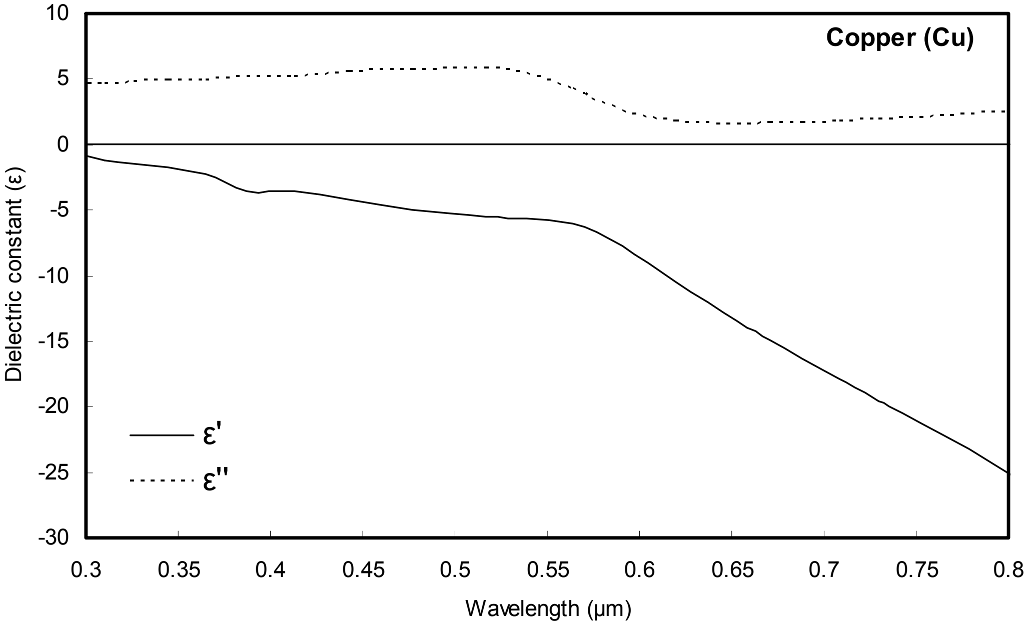

A.2. Silver (Ag)

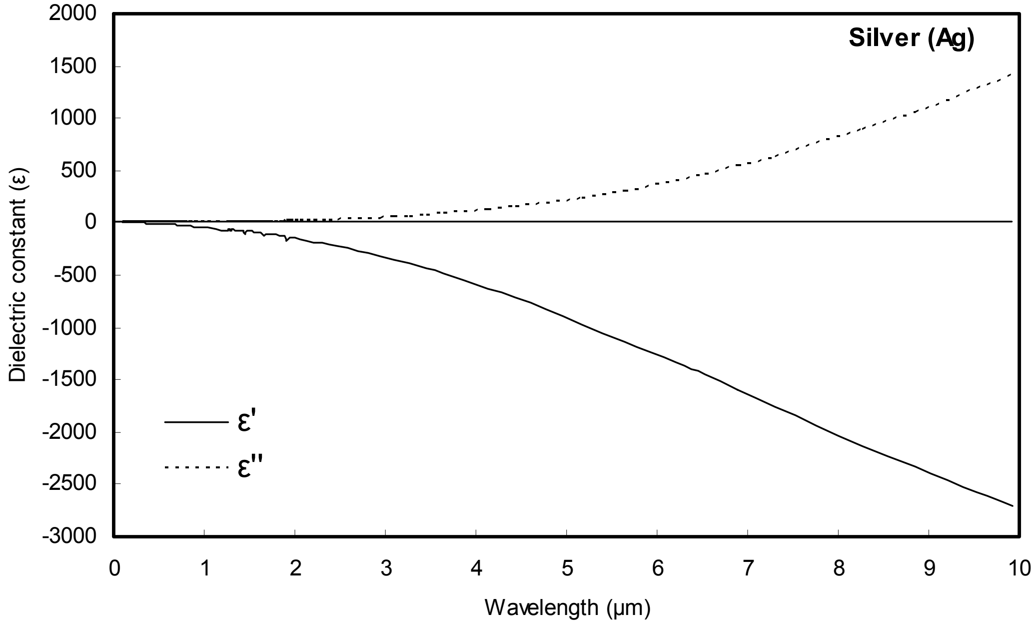
Silver (Ag)
Dielectric constant (ε)
2000
1500
1000
500
0
-500
-1000
-1500
-2000
-2500
-3000
0
1
2
3
4
5
6
7
8
9
10
Wavelength (μm)
ε'
ε''

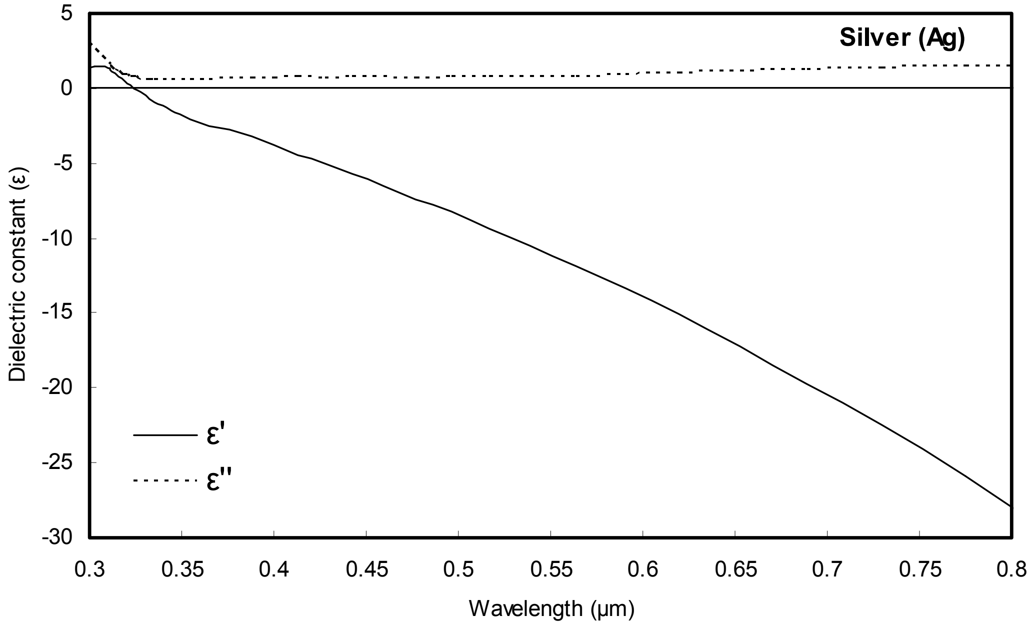
Silver (Ag)
Dielectric constant (ε)
5
0
-5
-10
-15
-20
-25
-30
0.3
0.35
0.4
0.45
0.5
0.55
0.6
0.65
0.7
0.75
0.8
Wavelength (μm)
ε'
ε''

A.3. Aluminum (Al)

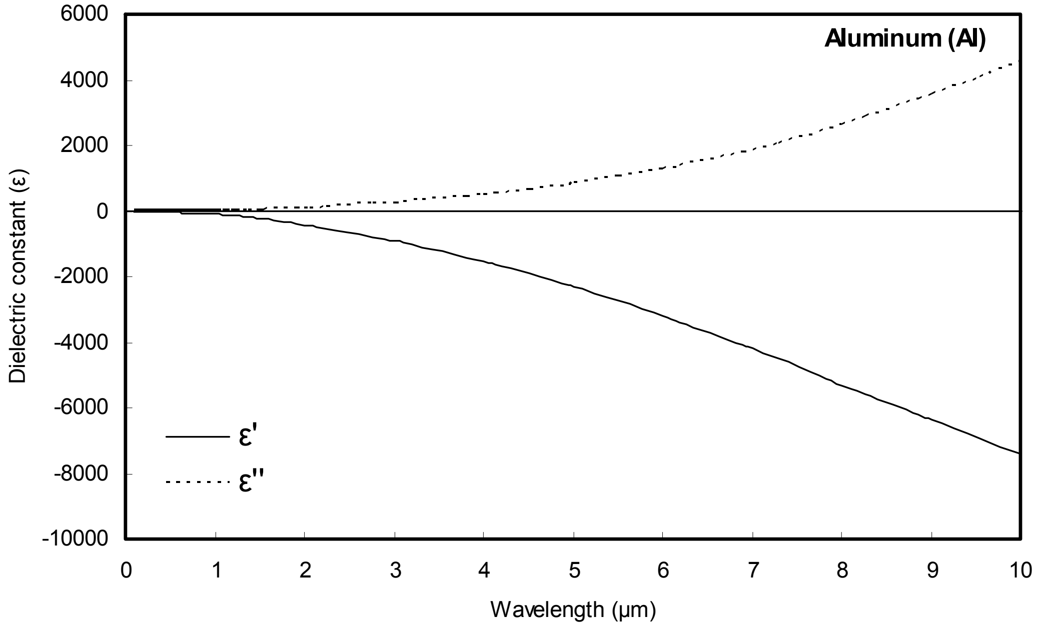

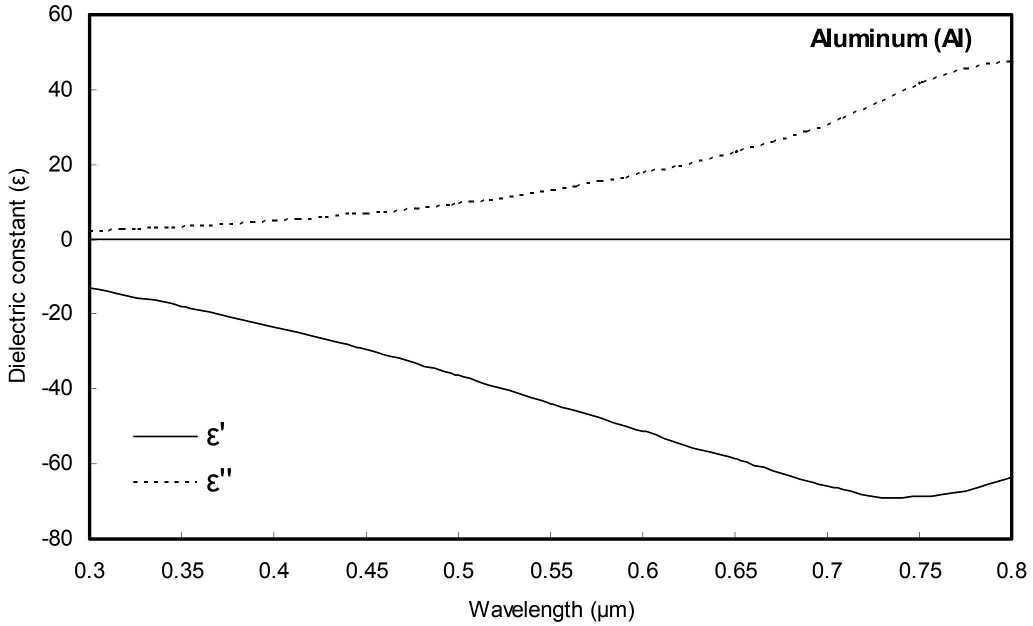

A.4. Tungsten (W)

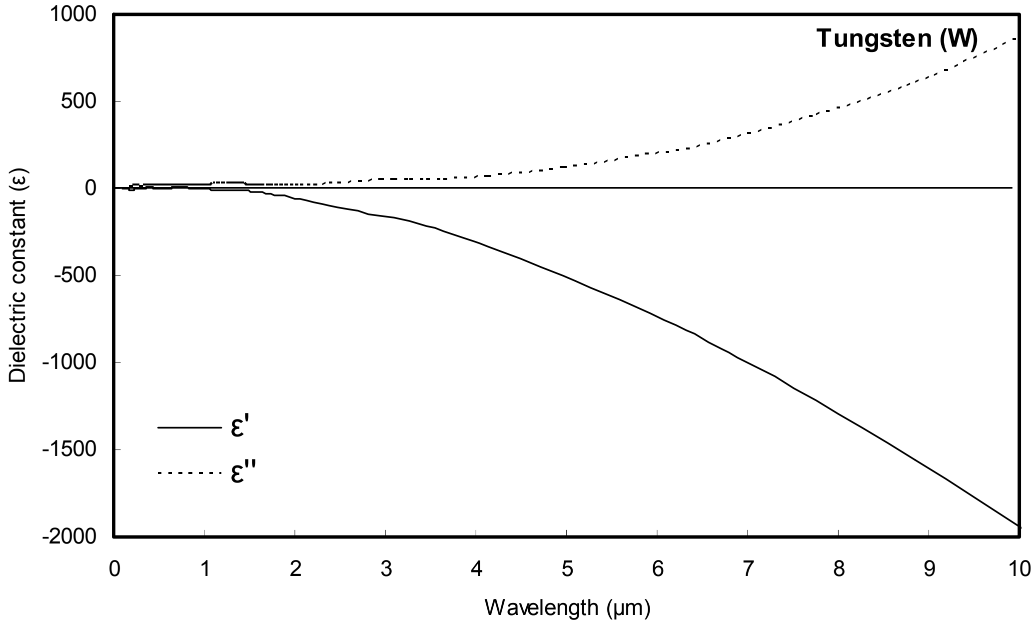

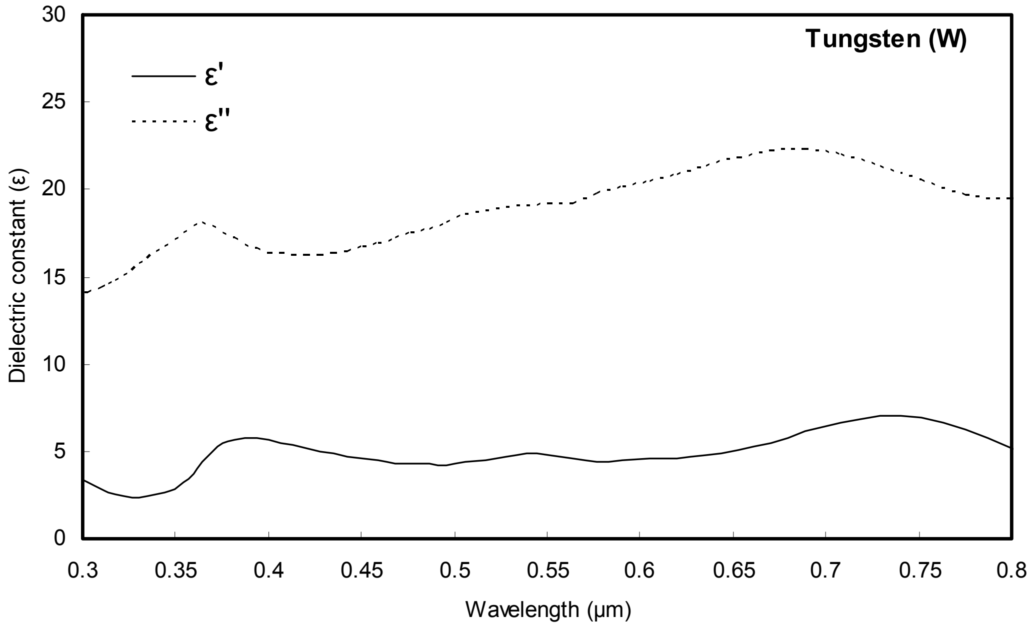

A.5. Gold (Au)

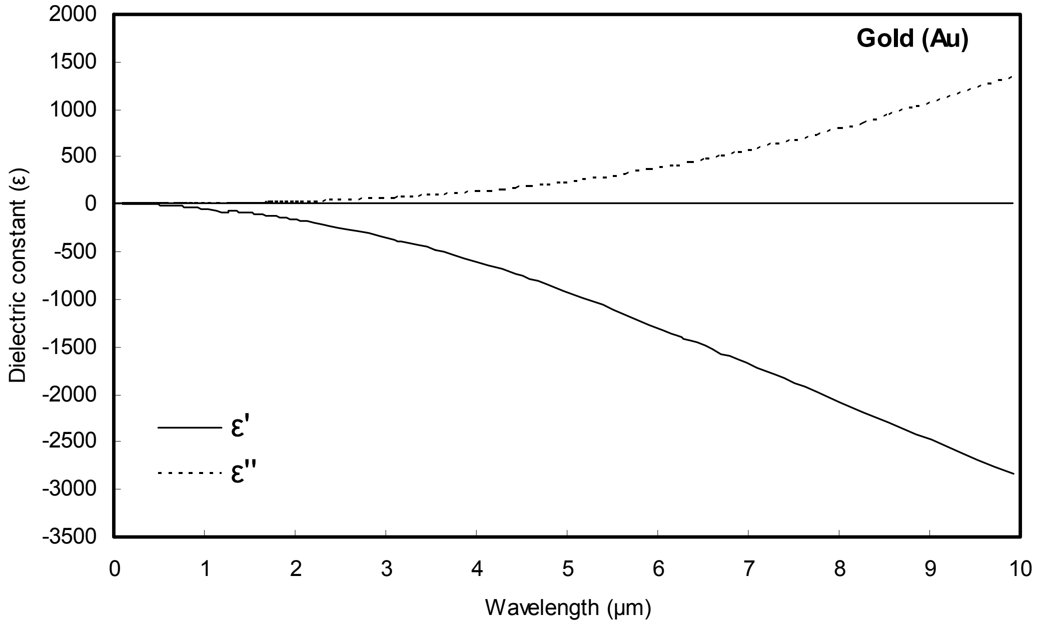
Gold (Au)
Dielectric constant (ε)
2000
1500
1000
500
0
-500
-1000
-1500
-2000
-2500
-3000
-3500
ε'
ε''
0
1
2
3
4
5
6
7
8
9
10
Wavelength (μm)

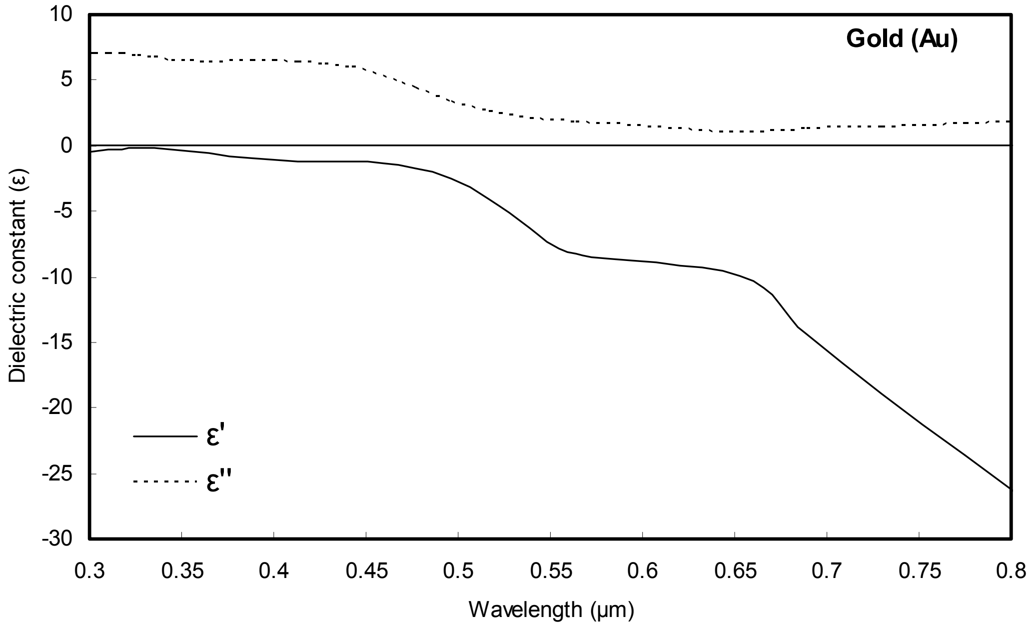
Gold (Au)
Dielectric constant (ε)
10
5
0
-5
-10
-15
-20
-25
-30
ε'
ε''
0.3
0.35
0.4
0.45
0.5
0.55
0.6
0.65
0.7
0.75
0.8
Wavelength (μm)

APPENDIX B

SURFACE PLASMON WAVEVECTORS AND PROPAGATION LENGTHS AT THE INTERFACE BETWEEN METALS AND AIR OR SILICON OXIDE

B.1. Copper (Cu)

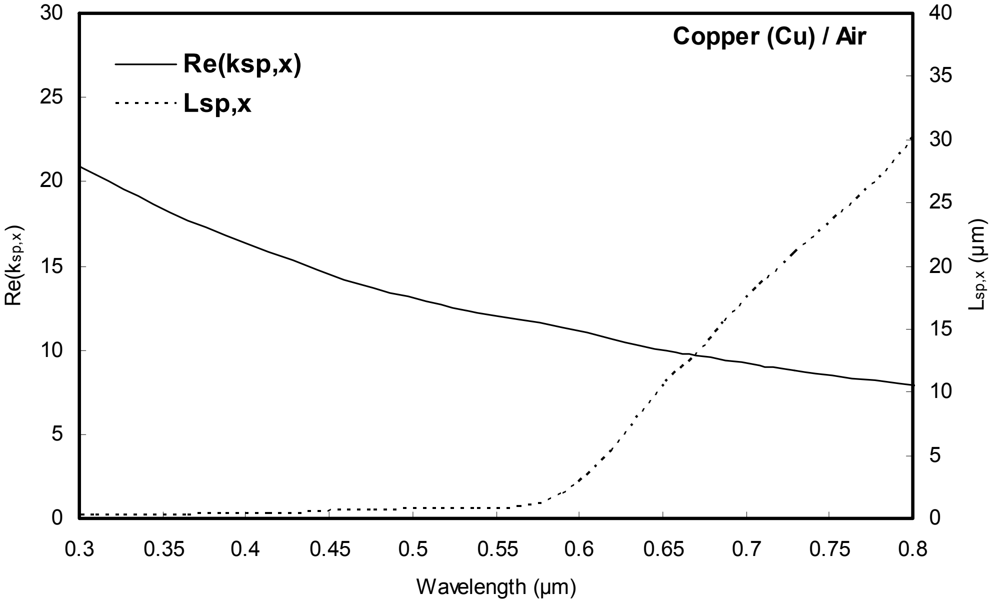

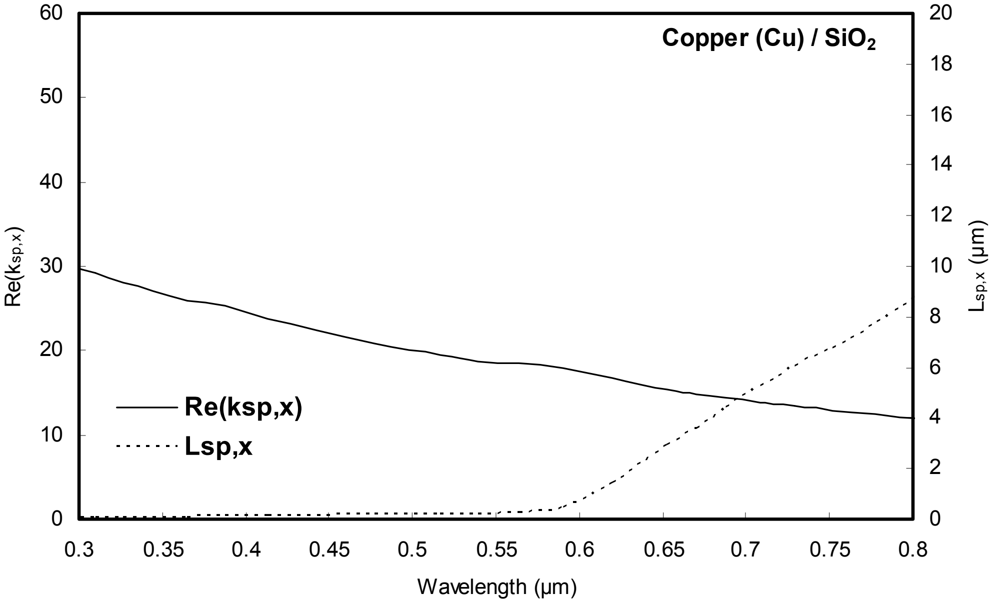

B.2. Silver (Ag)

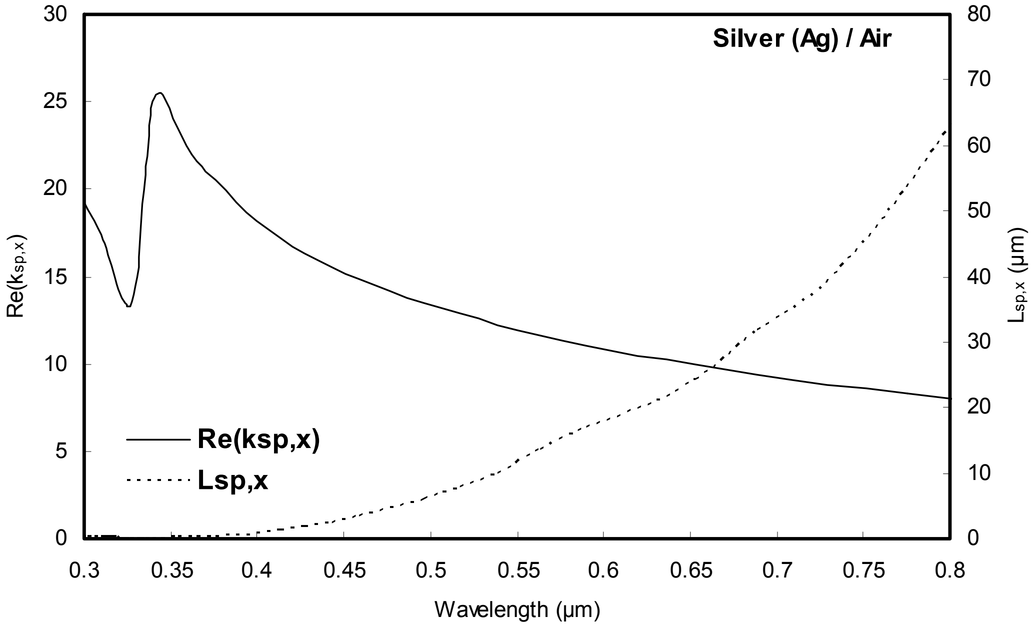

Silver (Ag) / Air
Re(ksp,x)
Lsp,x
Re($k_{sp,x}$)
$L_{sp,x}$ (µm)
Wavelength (µm)
0
5
10
15
20
25
30
0
10
20
30
40
50
60
70
80
0.3
0.35
0.4
0.45
0.5
0.55
0.6
0.65
0.7
0.75
0.8

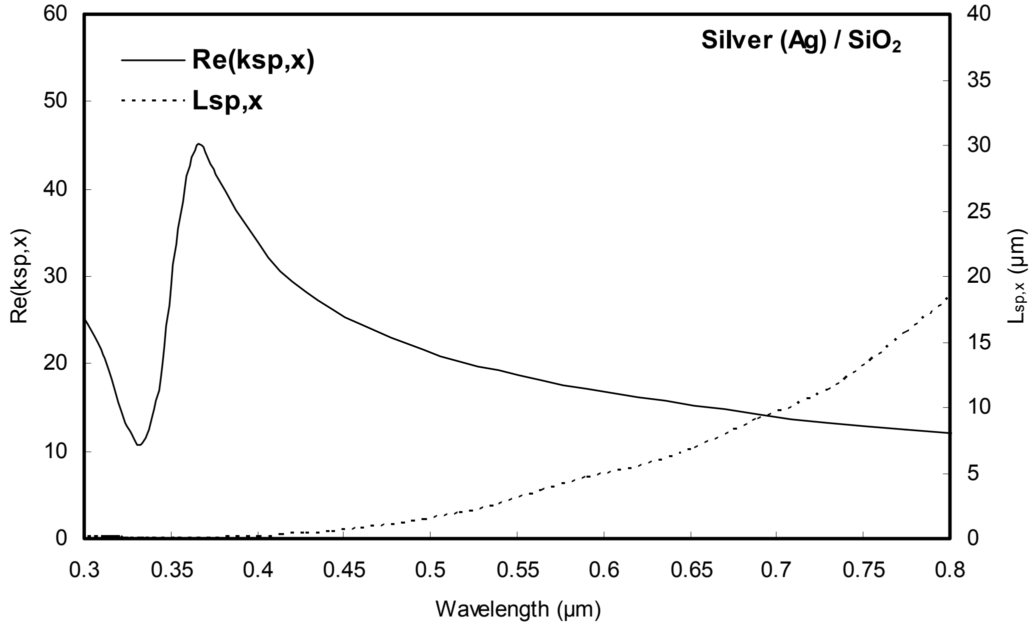

Silver (Ag) / SiO$_2$
Re(ksp,x)
Lsp,x
Re(ksp,x)
$L_{sp,x}$ (µm)
Wavelength (µm)
0
10
20
30
40
50
60
0
5
10
15
20
25
30
35
40
0.3
0.35
0.4
0.45
0.5
0.55
0.6
0.65
0.7
0.75
0.8

B.3. Aluminum (Al)

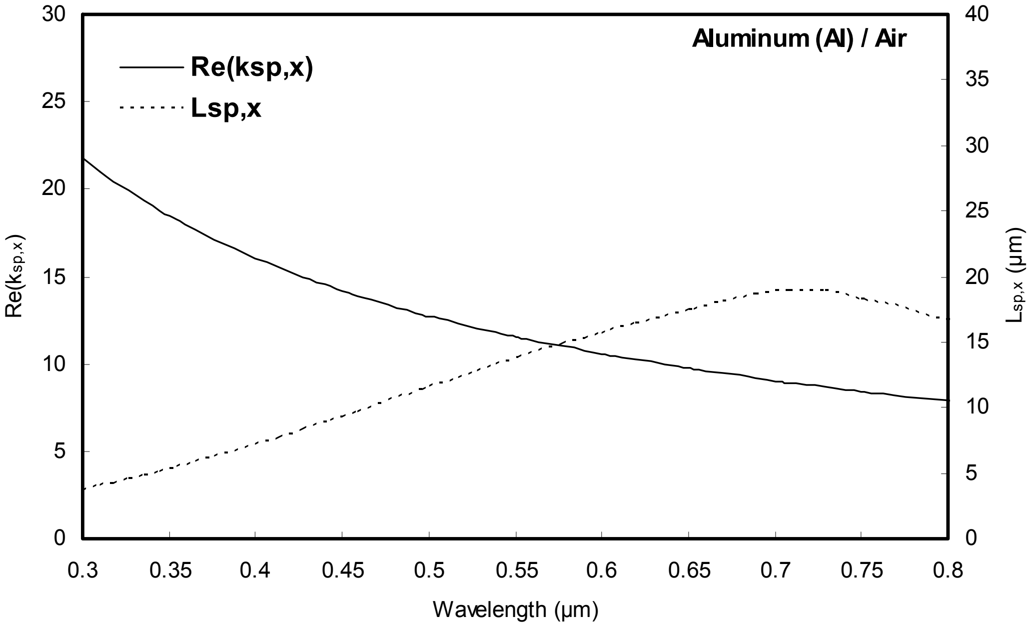

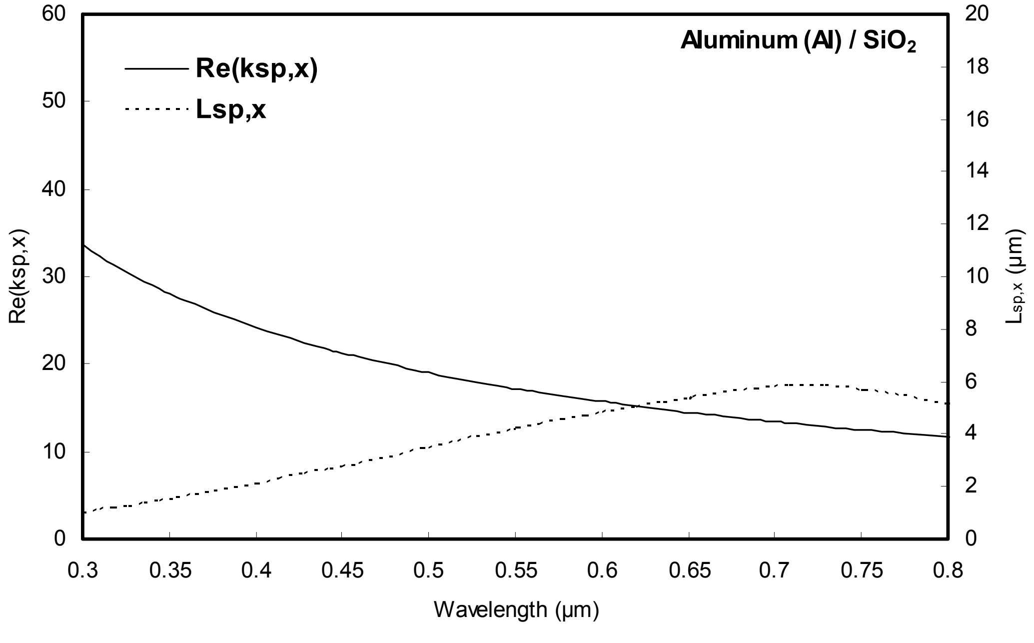

B.4. Tungsten (W)

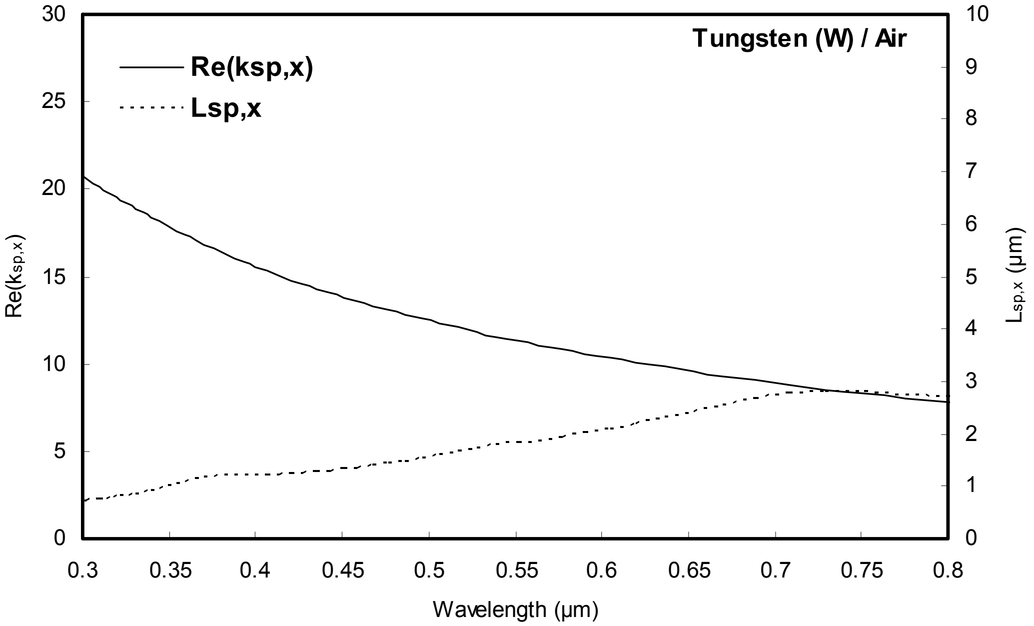

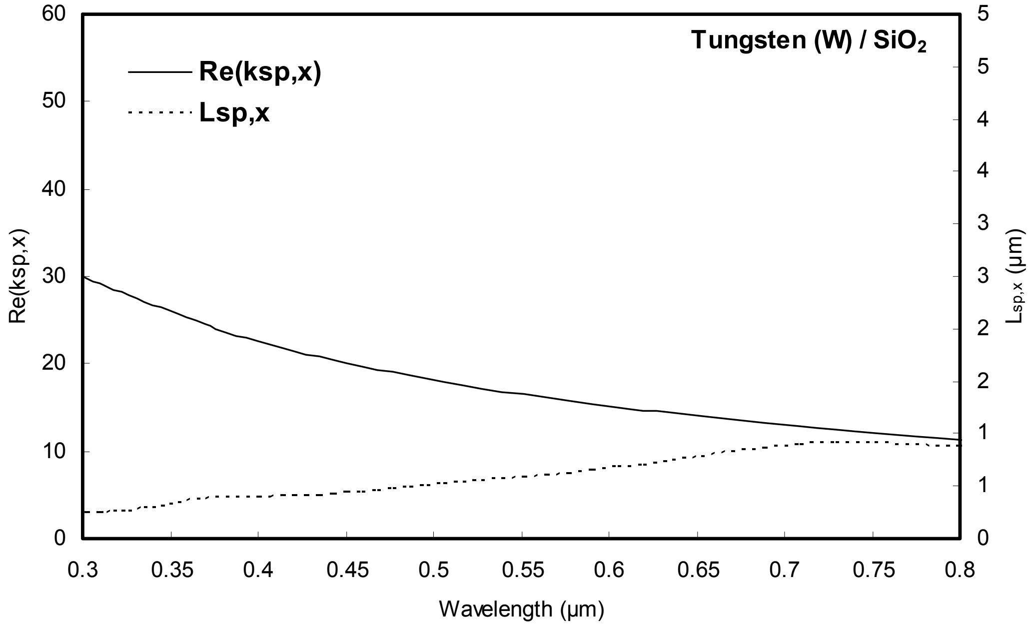

B.5. Gold (Au)

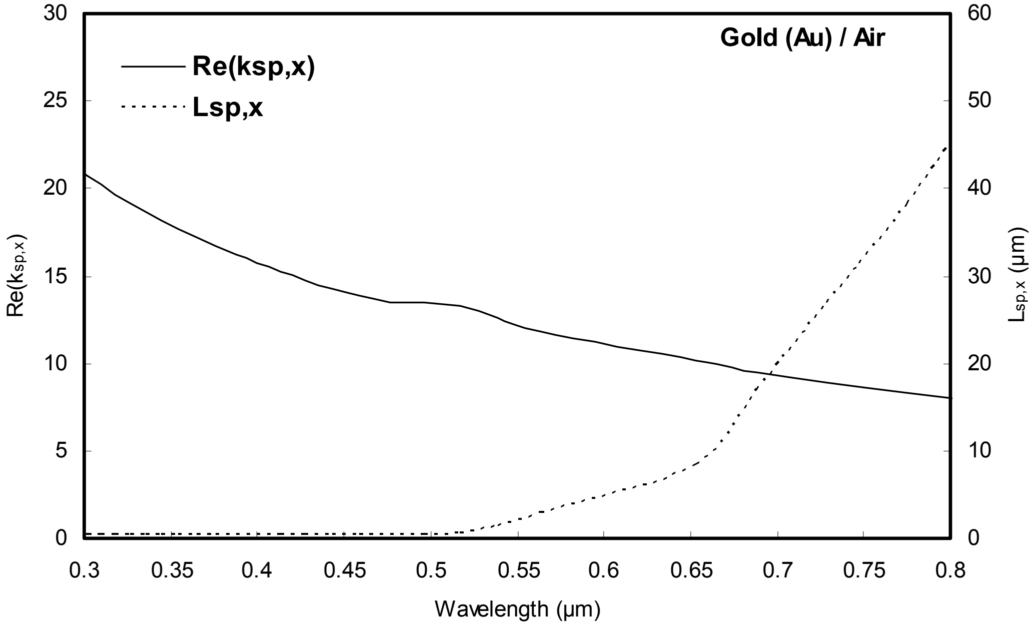
Gold (Au) / Air
Re(ksp,x)
Lsp,x
Re(ksp,x)
Lsp,x (µm)
Wavelength (µm)
0
5
10
15
20
25
30
0
10
20
30
40
50
60
0.3
0.35
0.4
0.45
0.5
0.55
0.6
0.65
0.7
0.75
0.8

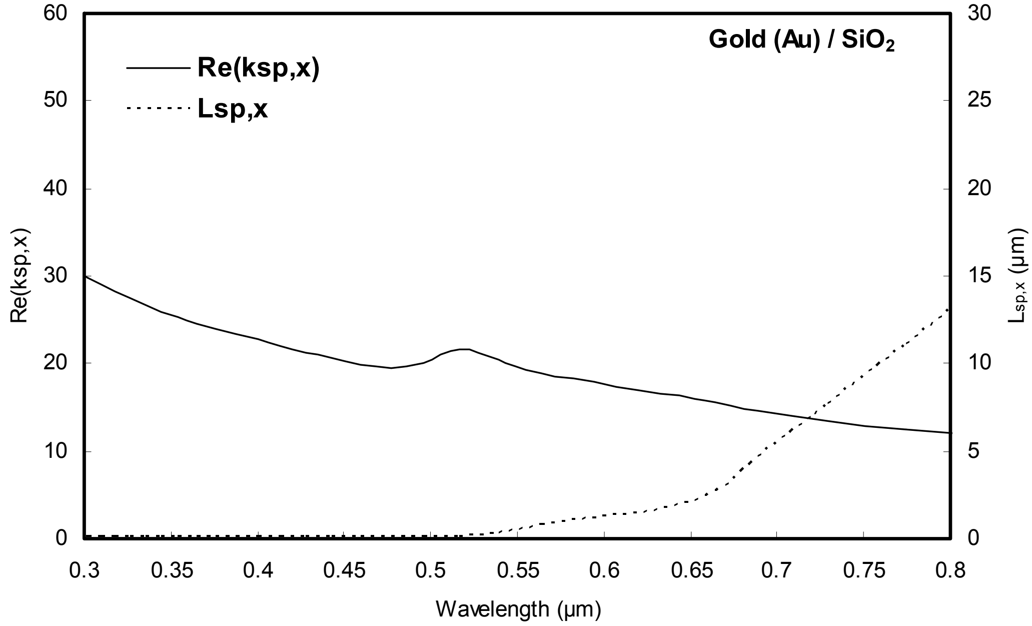
Gold (Au) / SiO2
Re(ksp,x)
Lsp,x
Re(ksp,x)
Lsp,x (µm)
Wavelength (µm)
0
10
20
30
40
50
60
0
5
10
15
20
25
30
0.3
0.35
0.4
0.45
0.5
0.55
0.6
0.65
0.7
0.75
0.8

APPENDIX C

TEMPEST INPUT SOURCE CODE

C.1. Plasmonic zone plate lens with high resolution

Simulation Parameters;

- Metal: Ag, Dielectric: PMMA, Incident Wavelength: 405 nm, Node Size: 20nm
- Plasmonic zone plate: *f* (focal length) = 0.5 µm, t_{Ag} = 100 nm, t_{PMMA} = 50 nm

```
wavelength 0.405        /* wavlength is 405nm */
x_node 400              /* # cells in domain x-dimension */
y_node 400              /* # cells in domain y-dimension */
z_node 150              /* # cells in domain z-dimension */
x_dim 8.0               /* length of the domain x-dimension */

/* excite a normally incident plane wave traveling in the upward (z) direction */
plane_source xy position 0.0 8.0 0.0 8.0 0.20 1 0 0 1 0 uniform 0 0
plane_source xy position 0.0 8.0 0.0 8.0 0.20 0 1 0 1 90 uniform 0 0

/* whole block fills the domain with air */
rectangle position 0.0 8.0 0.0 8.0 0.00 3.00 index 1.0 0.0

/* first block fills the domain with fused silica */
rectangle position 0.0 8.0 0.0 8.0 0.12 0.90 index 1.47 0.0

/* next block forms a plasmonic zone plate with silver */
rectangle position 0.0 8.0 0.0 8.0 0.90 1.00 dispersive 0.173 2.01
zcylinder position 3.246 0.60 0.70 4.0 4.0 index 1.53 0.0
zcylinder position 3.144 0.60 0.70 4.0 4.0 dispersive 0.173 2.01
zcylinder position 2.836 0.60 0.70 4.0 4.0 index 1.53 0.0
zcylinder position 2.733 0.60 0.70 4.0 4.0 dispersive 0.173 2.01
zcylinder position 2.423 0.60 0.70 4.0 4.0 index 1.53 0.0
zcylinder position 2.320 0.60 0.70 4.0 4.0 dispersive 0.173 2.01
zcylinder position 2.008 0.60 0.70 4.0 4.0 index 1.53 0.0
zcylinder position 1.903 0.60 0.70 4.0 4.0 dispersive 0.173 2.01
zcylinder position 1.587 0.60 0.70 4.0 4.0 index 1.53 0.0
zcylinder position 1.481 0.60 0.70 4.0 4.0 dispersive 0.173 2.01
zcylinder position 1.155 0.60 0.70 4.0 4.0 index 1.53 0.0
zcylinder position 1.044 0.60 0.70 4.0 4.0 dispersive 0.173 2.01
zcylinder position 0.689 0.60 0.70 4.0 4.0 index 1.53 0.0
zcylinder position 0.559 0.60 0.70 4.0 4.0 dispersive 0.173 2.01

/* next block fills the domain with PMMA */
```

```
rectangle position 0.0 8. 0 0.0 8. 0 0.70 0.75 index 1.53 0.0

/* 6 cells of PML (matched to fused silica) at the bottom of the domain form the
absorbing boundary condition at the bottom of the domain */
rectangle position 0.0 8.0 0.0 8.0 0.00 0.12 pml 0 0 -1 2.1609 1 0 0

/* 6 cells of PML (matched to air) at the top of the domain form the absorbing boundary
condition at the top of the domain */
rectangle position 0.0 8.0 0.0 8.0 2.88 3.00 pml 0 0 1 1.0 1 0 0

/* output the electric field intensity at the domain (xz-plane, y = 4.0) */
plot ex steady 0.00 position 0 8.0 4.0 4.0 0.12 2.88 exi
plot ey steady 0.00 position 0 8.0 4.0 4.0 0.12 2.88 eyi
plot ez steady 0.00 position 0 8.0 4.0 4.0 0.12 2.88 ezi
plot ex steady 0.25 position 0 8.0 4.0 4.0 0.12 2.88 exq
plot ey steady 0.25 position 0 8.0 4.0 4.0 0.12 2.88 eyq
plot ez steady 0.25 position 0 8.0 4.0 4.0 0.12 2.88 ezq

/* output the electric field intensity at the domain (yz-plane, x = 4.0) */
plot ex steady 0.00 position 4.0 4.0 0 8.0 0.12 2.88 dxi
plot ey steady 0.00 position 4.0 4.0 0 8.0 0.12 2.88 dyi
plot ez steady 0.00 position 4.0 4.0 0 8.0 0.12 2.88 dzi
plot ex steady 0.25 position 4.0 4.0 0 8.0 0.12 2.88 dxq
plot ey steady 0.25 position 4.0 4.0 0 8.0 0.12 2.88 dyq
plot ez steady 0.25 position 4.0 4.0 0 8.0 0.12 2.88 dzq

/* output the electric field intensity at the domain (xy-plane, input side of zone plate) */
plot ex steady 0.00 position 0 8.0 0 8.0 0.60 0.60 fxi
plot ey steady 0.00 position 0 8.0 0 8.0 0.60 0.60 fyi
plot ez steady 0.00 position 0 8.0 0 8.0 0.60 0.60 fzi
plot ex steady 0.25 position 0 8.0 0 8.0 0.60 0.60 fxq
plot ey steady 0.25 position 0 8.0 0 8.0 0.60 0.60 fyq
plot ez steady 0.25 position 0 8.0 0 8.0 0.60 0.60 fzq

/* output the electric field intensity at the domain (xy-plane, output side of zone plate) */
plot ex steady 0.00 position 0 8.0 0 8.0 0.70 0.70 gxi
plot ey steady 0.00 position 0 8.0 0 8.0 0.70 0.70 gyi
plot ez steady 0.00 position 0 8.0 0 8.0 0.70 0.70 gzi
plot ex steady 0.25 position 0 8.0 0 8.0 0.70 0.70 gxq
plot ey steady 0.25 position 0 8.0 0 8.0 0.70 0.70 gyq
plot ez steady 0.25 position 0 8.0 0 8.0 0.70 0.70 gzq

/* plot the refractive index */
plot refractive position 0.0 8.0 4.0 4.0 0.00 3.0 en1
```

```
plot refractive position 0.0 8.0 0.0 8.0 1.0 1.0 en2
```

C.2. Plasmonic zone plate lens with high efficiency

Simulation Parameters;

- Metal: Ag, Dielectric: SiO$_2$, Incident Wavelength: 405 nm, Node Size: 30nm
- Plasmonic zone plate: f (focal length) = 1.0 µm, t_{Ag} = 30 nm, t_{SiO2} = 30 nm
  N (building block) = 5

```
wavelength 0.405      /* wavlength is 405nm */
x_node 270            /* # cells in domain x-dimension */
y_node 270            /* # cells in domain y-dimension */
z_node 175            /* # cells in domain z-dimension */
x_dim 8.10            /* length of the domain x-dimension */

/* excite a normally incident plane wave traveling in the upward (z) direction */
plane_source xy position 0.0 8.10 0.0 8.10 0.20 1 0 0 1 0 uniform 0 0
plane_source xy position 0.0 8.10 0.0 8.10 0.20 0 1 0 1 90 uniform 0 0

/* whole block fills the domain with air */
rectangle position 0.0 8.10 0.0 8.10 0.00 5.25 index 1.0 0.0

/* first block fills the domain with fused silica */
rectangle position 0.0 8.10 0.0 8.10 0.12 0.60 index 1.47 0.0

/* 1st building block forms a plasmonic zone plate with silver */
rectangle position 0.0 8.10 0.0 8.10 0.60 0.63 dispersive 0.173 2.01
zcylinder position 3.702 0.60 0.63 4.0 4.0 index 1.0 0.0
zcylinder position 3.492 0.60 0.63 4.0 4.0 dispersive 0.173 2.01
zcylinder position 3.281 0.60 0.63 4.0 4.0 index 1.0 0.0
zcylinder position 3.069 0.60 0.63 4.0 4.0 dispersive 0.173 2.01
zcylinder position 2.855 0.60 0.63 4.0 4.0 index 1.0 0.0
zcylinder position 2.639 0.60 0.63 4.0 4.0 dispersive 0.173 2.01
zcylinder position 2.422 0.60 0.63 4.0 4.0 index 1.0 0.0
zcylinder position 2.201 0.60 0.63 4.0 4.0 dispersive 0.173 2.01
zcylinder position 1.976 0.60 0.63 4.0 4.0 index 1.0 0.0
zcylinder position 1.746 0.60 0.63 4.0 4.0 dispersive 0.173 2.01
zcylinder position 1.509 0.60 0.63 4.0 4.0 index 1.0 0.0
zcylinder position 1.259 0.60 0.63 4.0 4.0 dispersive 0.173 2.01
zcylinder position 0.987 0.60 0.63 4.0 4.0 index 1.0 0.0
zcylinder position 0.668 0.60 0.63 4.0 4.0 dispersive 0.173 2.01

/* 1st building block forms a plasmonic zone plate with silicon oxide */
```

```
rectangle position 0.0 8.10 0.0 8.10 0.63 0.66 index 1.47 0.0
zcylinder position 3.702 0.63 0.66 4.0 4.0 index 1.0 0.0
zcylinder position 3.492 0.63 0.66 4.0 4.0 index 1.47 0.0
zcylinder position 3.281 0.63 0.66 4.0 4.0 index 1.0 0.0
zcylinder position 3.069 0.63 0.66 4.0 4.0 index 1.47 0.0
zcylinder position 2.855 0.63 0.66 4.0 4.0 index 1.0 0.0
zcylinder position 2.639 0.63 0.66 4.0 4.0 index 1.47 0.0
zcylinder position 2.422 0.63 0.66 4.0 4.0 index 1.0 0.0
zcylinder position 2.201 0.63 0.66 4.0 4.0 index 1.47 0.0
zcylinder position 1.976 0.63 0.66 4.0 4.0 index 1.0 0.0
zcylinder position 1.746 0.63 0.66 4.0 4.0 index 1.47 0.0
zcylinder position 1.509 0.63 0.66 4.0 4.0 index 1.0 0.0
zcylinder position 1.259 0.63 0.66 4.0 4.0 index 1.47 0.0
zcylinder position 0.987 0.63 0.66 4.0 4.0 index 1.0 0.0
zcylinder position 0.668 0.63 0.66 4.0 4.0 index 1.47 0.0

/* 2nd building block forms a plasmonic zone plate with silver */
rectangle position 0.0 8.10 0.0 8.10 0.66 0.69 dispersive 0.173 2.01
zcylinder position 3.702 0.66 0.69 4.0 4.0 index 1.0 0.0
zcylinder position 3.492 0.66 0.69 4.0 4.0 dispersive 0.173 2.01
zcylinder position 3.281 0.66 0.69 4.0 4.0 index 1.0 0.0
zcylinder position 3.069 0.66 0.69 4.0 4.0 dispersive 0.173 2.01
zcylinder position 2.855 0.66 0.69 4.0 4.0 index 1.0 0.0
zcylinder position 2.639 0.66 0.69 4.0 4.0 dispersive 0.173 2.01
zcylinder position 2.422 0.66 0.69 4.0 4.0 index 1.0 0.0
zcylinder position 2.201 0.66 0.69 4.0 4.0 dispersive 0.173 2.01
zcylinder position 1.976 0.66 0.69 4.0 4.0 index 1.0 0.0
zcylinder position 1.746 0.66 0.69 4.0 4.0 dispersive 0.173 2.01
zcylinder position 1.509 0.66 0.69 4.0 4.0 index 1.0 0.0
zcylinder position 1.259 0.66 0.69 4.0 4.0 dispersive 0.173 2.01
zcylinder position 0.987 0.66 0.69 4.0 4.0 index 1.0 0.0
zcylinder position 0.668 0.66 0.69 4.0 4.0 dispersive 0.173 2.01

/* 2nd building block forms a plasmonic zone plate with silicon oxide */
rectangle position 0.0 8.10 0.0 8.10 0.69 0.72 index 1.47 0.0
zcylinder position 3.702 0.69 0.72 4.0 4.0 index 1.0 0.0
zcylinder position 3.492 0.69 0.72 4.0 4.0 index 1.47 0.0
zcylinder position 3.281 0.69 0.72 4.0 4.0 index 1.0 0.0
zcylinder position 3.069 0.69 0.72 4.0 4.0 index 1.47 0.0
zcylinder position 2.855 0.69 0.72 4.0 4.0 index 1.0 0.0
zcylinder position 2.639 0.69 0.72 4.0 4.0 index 1.47 0.0
zcylinder position 2.422 0.69 0.72 4.0 4.0 index 1.0 0.0
zcylinder position 2.201 0.69 0.72 4.0 4.0 index 1.47 0.0
zcylinder position 1.976 0.69 0.72 4.0 4.0 index 1.0 0.0
```

```
zcylinder position 1.746 0.69 0.72 4.0 4.0 index 1.47 0.0
zcylinder position 1.509 0.69 0.72 4.0 4.0 index 1.0 0.0
zcylinder position 1.259 0.69 0.72 4.0 4.0 index 1.47 0.0
zcylinder position 0.987 0.69 0.72 4.0 4.0 index 1.0 0.0
zcylinder position 0.668 0.69 0.72 4.0 4.0 index 1.47 0.0

/* 3rd building block forms a plasmonic zone plate with silver */
rectangle position 0.0 8.10 0.0 8.10 0.72 0.75 dispersive 0.173 2.01
zcylinder position 3.702 0.72 0.75 4.0 4.0 index 1.0 0.0
zcylinder position 3.492 0.72 0.75 4.0 4.0 dispersive 0.173 2.01
zcylinder position 3.281 0.72 0.75 4.0 4.0 index 1.0 0.0
zcylinder position 3.069 0.72 0.75 4.0 4.0 dispersive 0.173 2.01
zcylinder position 2.855 0.72 0.75 4.0 4.0 index 1.0 0.0
zcylinder position 2.639 0.72 0.75 4.0 4.0 dispersive 0.173 2.01
zcylinder position 2.422 0.72 0.75 4.0 4.0 index 1.0 0.0
zcylinder position 2.201 0.72 0.75 4.0 4.0 dispersive 0.173 2.01
zcylinder position 1.976 0.72 0.75 4.0 4.0 index 1.0 0.0
zcylinder position 1.746 0.72 0.75 4.0 4.0 dispersive 0.173 2.01
zcylinder position 1.509 0.72 0.75 4.0 4.0 index 1.0 0.0
zcylinder position 1.259 0.72 0.75 4.0 4.0 dispersive 0.173 2.01
zcylinder position 0.987 0.72 0.75 4.0 4.0 index 1.0 0.0
zcylinder position 0.668 0.72 0.75 4.0 4.0 dispersive 0.173 2.01

/* 3rd building block forms a plasmonic zone plate with silicon oxide */
rectangle position 0.0 8.10 0.0 8.10 0.75 0.78 index 1.47 0.0
zcylinder position 3.702 0.75 0.78 4.0 4.0 index 1.0 0.0
zcylinder position 3.492 0.75 0.78 4.0 4.0 index 1.47 0.0
zcylinder position 3.281 0.75 0.78 4.0 4.0 index 1.0 0.0
zcylinder position 3.069 0.75 0.78 4.0 4.0 index 1.47 0.0
zcylinder position 2.855 0.75 0.78 4.0 4.0 index 1.0 0.0
zcylinder position 2.639 0.75 0.78 4.0 4.0 index 1.47 0.0
zcylinder position 2.422 0.75 0.78 4.0 4.0 index 1.0 0.0
zcylinder position 2.201 0.75 0.78 4.0 4.0 index 1.47 0.0
zcylinder position 1.976 0.75 0.78 4.0 4.0 index 1.0 0.0
zcylinder position 1.746 0.75 0.78 4.0 4.0 index 1.47 0.0
zcylinder position 1.509 0.75 0.78 4.0 4.0 index 1.0 0.0
zcylinder position 1.259 0.75 0.78 4.0 4.0 index 1.47 0.0
zcylinder position 0.987 0.75 0.78 4.0 4.0 index 1.0 0.0
zcylinder position 0.668 0.75 0.78 4.0 4.0 index 1.47 0.0

/* 4th building block forms a plasmonic zone plate with silver */
rectangle position 0.0 8.10 0.0 8.10 0.78 0.81 dispersive 0.173 2.01
zcylinder position 3.702 0.78 0.81 4.0 4.0 index 1.0 0.0
zcylinder position 3.492 0.78 0.81 4.0 4.0 dispersive 0.173 2.01
```

```
zcylinder position 3.281 0.78 0.81 4.0 4.0 index 1.0 0.0
zcylinder position 3.069 0.78 0.81 4.0 4.0 dispersive 0.173 2.01
zcylinder position 2.855 0.78 0.81 4.0 4.0 index 1.0 0.0
zcylinder position 2.639 0.78 0.81 4.0 4.0 dispersive 0.173 2.01
zcylinder position 2.422 0.78 0.81 4.0 4.0 index 1.0 0.0
zcylinder position 2.201 0.78 0.81 4.0 4.0 dispersive 0.173 2.01
zcylinder position 1.976 0.78 0.81 4.0 4.0 index 1.0 0.0
zcylinder position 1.746 0.78 0.81 4.0 4.0 dispersive 0.173 2.01
zcylinder position 1.509 0.78 0.81 4.0 4.0 index 1.0 0.0
zcylinder position 1.259 0.78 0.81 4.0 4.0 dispersive 0.173 2.01
zcylinder position 0.987 0.78 0.81 4.0 4.0 index 1.0 0.0
zcylinder position 0.668 0.78 0.81 4.0 4.0 dispersive 0.173 2.01

/* 4th building block forms a plasmonic zone plate with silicon oxide */
rectangle position 0.0 8.10 0.0 8.10 0.81 0.84 index 1.47 0.0
zcylinder position 3.702 0.81 0.84 4.0 4.0 index 1.0 0.0
zcylinder position 3.492 0.81 0.84 4.0 4.0 index 1.47 0.0
zcylinder position 3.281 0.81 0.84 4.0 4.0 index 1.0 0.0
zcylinder position 3.069 0.81 0.84 4.0 4.0 index 1.47 0.0
zcylinder position 2.855 0.81 0.84 4.0 4.0 index 1.0 0.0
zcylinder position 2.639 0.81 0.84 4.0 4.0 index 1.47 0.0
zcylinder position 2.422 0.81 0.84 4.0 4.0 index 1.0 0.0
zcylinder position 2.201 0.81 0.84 4.0 4.0 index 1.47 0.0
zcylinder position 1.976 0.81 0.84 4.0 4.0 index 1.0 0.0
zcylinder position 1.746 0.81 0.84 4.0 4.0 index 1.47 0.0
zcylinder position 1.509 0.81 0.84 4.0 4.0 index 1.0 0.0
zcylinder position 1.259 0.81 0.84 4.0 4.0 index 1.47 0.0
zcylinder position 0.987 0.81 0.84 4.0 4.0 index 1.0 0.0
zcylinder position 0.668 0.81 0.84 4.0 4.0 index 1.47 0.0

/* 5th building block forms a plasmonic zone plate with silver */
rectangle position 0.0 8.10 0.0 8.10 0.84 0.87 dispersive 0.173 2.01
zcylinder position 3.702 0.84 0.87 4.0 4.0 index 1.0 0.0
zcylinder position 3.492 0.84 0.87 4.0 4.0 dispersive 0.173 2.01
zcylinder position 3.281 0.84 0.87 4.0 4.0 index 1.0 0.0
zcylinder position 3.069 0.84 0.87 4.0 4.0 dispersive 0.173 2.01
zcylinder position 2.855 0.84 0.87 4.0 4.0 index 1.0 0.0
zcylinder position 2.639 0.84 0.87 4.0 4.0 dispersive 0.173 2.01
zcylinder position 2.422 0.84 0.87 4.0 4.0 index 1.0 0.0
zcylinder position 2.201 0.84 0.87 4.0 4.0 dispersive 0.173 2.01
zcylinder position 1.976 0.84 0.87 4.0 4.0 index 1.0 0.0
zcylinder position 1.746 0.84 0.87 4.0 4.0 dispersive 0.173 2.01
zcylinder position 1.509 0.84 0.87 4.0 4.0 index 1.0 0.0
zcylinder position 1.259 0.84 0.87 4.0 4.0 dispersive 0.173 2.01
```

```
zcylinder position 0.987 0.84 0.87 4.0 4.0 index 1.0 0.0
zcylinder position 0.668 0.84 0.87 4.0 4.0 dispersive 0.173 2.01

/* 5th building block forms a plasmonic zone plate with silicon oxide */
rectangle position 0.0 8.10 0.0 8.10 0.87 0.90 index 1.47 0.0
zcylinder position 3.702 0.87 0.90 4.0 4.0 index 1.0 0.0
zcylinder position 3.492 0.87 0.90 4.0 4.0 index 1.47 0.0
zcylinder position 3.281 0.87 0.90 4.0 4.0 index 1.0 0.0
zcylinder position 3.069 0.87 0.90 4.0 4.0 index 1.47 0.0
zcylinder position 2.855 0.87 0.90 4.0 4.0 index 1.0 0.0
zcylinder position 2.639 0.87 0.90 4.0 4.0 index 1.47 0.0
zcylinder position 2.422 0.87 0.90 4.0 4.0 index 1.0 0.0
zcylinder position 2.201 0.87 0.90 4.0 4.0 index 1.47 0.0
zcylinder position 1.976 0.87 0.90 4.0 4.0 index 1.0 0.0
zcylinder position 1.746 0.87 0.90 4.0 4.0 index 1.47 0.0
zcylinder position 1.509 0.87 0.90 4.0 4.0 index 1.0 0.0
zcylinder position 1.259 0.87 0.90 4.0 4.0 index 1.47 0.0
zcylinder position 0.987 0.87 0.90 4.0 4.0 index 1.0 0.0
zcylinder position 0.668 0.87 0.90 4.0 4.0 index 1.47 0.0

/* 6 cells of PML (matched to fused silica) at the bottom of the domain form the
absorbing boundary condition at the bottom of the domain */
rectangle position 0.0 8.10 0.0 8.10 0.00 0.12 pml 0 0 -1 2.1609 1 0 0

/* 6 cells of PML (matched to air) at the top of the domain form the absorbing boundary
condition at the top of the domain */
rectangle position 0.0 8.10 0.0 8.10 5.13 5.25 pml 0 0 1 1.0 1 0 0

/* output the electric field intensity at the domain (xz-plane, y = 4.0) */
plot ex steady 0.00 position 0 8.0 4.0 4.0 0.12 2.88 exi
plot ey steady 0.00 position 0 8.0 4.0 4.0 0.12 2.88 eyi
plot ez steady 0.00 position 0 8.0 4.0 4.0 0.12 2.88 ezi
plot ex steady 0.25 position 0 8.0 4.0 4.0 0.12 2.88 exq
plot ey steady 0.25 position 0 8.0 4.0 4.0 0.12 2.88 eyq
plot ez steady 0.25 position 0 8.0 4.0 4.0 0.12 2.88 ezq

/* output the electric field intensity at the domain (yz-plane, x = 4.0) */
plot ex steady 0.00 position 0 8.10 4.0 4.0 0.12 5.13 exi
plot ey steady 0.00 position 0 8.10 4.0 4.0 0.12 5.13 eyi
plot ez steady 0.00 position 0 8.10 4.0 4.0 0.12 5.13 ezi
plot ex steady 0.25 position 0 8.10 4.0 4.0 0.12 5.13 exq
plot ey steady 0.25 position 0 8.10 4.0 4.0 0.12 5.13 eyq
plot ez steady 0.25 position 0 8.10 4.0 4.0 0.12 5.13 ezq
```

```
/* output the electric field intensity at the domain (xy-plane, input side of zone plate) */
plot ex steady 0.00 position 4.0 4.0 0 8.10 0.12 5.13 dxi
plot ey steady 0.00 position 4.0 4.0 0 8.10 0.12 5.13 dyi
plot ez steady 0.00 position 4.0 4.0 0 8.10 0.12 5.13 dzi
plot ex steady 0.25 position 4.0 4.0 0 8.10 0.12 5.13 dxq
plot ey steady 0.25 position 4.0 4.0 0 8.10 0.12 5.13 dyq
plot ez steady 0.25 position 4.0 4.0 0 8.10 0.12 5.13 dzq

/* output the electric field intensity at the domain (xy-plane, output side of zone plate) */
plot ex steady 0.00 position 0 8.10 0 8.10 0.90 0.90 gxi
plot ey steady 0.00 position 0 8.10 0 8.10 0.90 0.90 gyi
plot ez steady 0.00 position 0 8.10 0 8.10 0.90 0.90 gzi
plot ex steady 0.25 position 0 8.10 0 8.10 0.90 0.90 gxq
plot ey steady 0.25 position 0 8.10 0 8.10 0.90 0.90 gyq
plot ez steady 0.25 position 0 8.10 0 8.10 0.90 0.90 gzq

/* plot the refractive index */
plot refractive position 0.0 8.10 4.0 4.0 0.00 5.25 en1
plot refractive position 0.0 8.10 0.0 8.10 0.90 0.90 en2
```

C.3. SERS-active Substrate

Simulation Parameters;

- Metal: Ag, Spacer: SiO_2, Incident Wavelength: 785 nm, Grid Size: 5nm
- Equilateral triangular prism-shaped particle: Resonant Length = 110 nm, Particle t_{Ag} = 40 nm, Spacer t_{SiO2} = 20 nm, Lower t_{Ag} = 100 nm

```
wavelength 0.785        /* wavlength is 785 nm */
x_node 200              /* # cells in domain x-dimension */
y_node 200              /* # cells in domain y-dimension */
z_node 400              /* # cells in domain z-dimension */
x_dim 1.0               /* Length of the domain x-dimension */

/* excite a normally incident plane wave traveling in the upward (z) direction */
plane_source xy position 0.0 1.0 0.0 1.0 0.12 1 0 0 1 0 uniform 0 0
plane_source xy position 0.0 1.0 0.0 1.0 0.12 0 1 0 1 90 uniform 0 0

/* whole block fills the domain with air */
rectangle position 0.0 1.0 0.0 1.0 0.0 2.0 index 1.0 0.0

/* first block forms a nanoparticle with silver */
zwedge position 0.94 0.98 0.445 0.435 0.445 0.565 0.555 0.500 dispersive 0.143
```

```
/* next block fills the domain with SiO2 as spacer layer */
rectangle position 0.0 1.0 0.0 1.0 0.98 1.0 index 1.45 0.0

/* next block forms a lower metal layer with silver */
rectangle position 0.0 1.0 0.0 1.0 1.0 1.1 dispersive 0.143 5.17

/* next block fills the domain with SiO2 as substrate */
rectangle position 0.0 1.0 0.0 1.0 1.1 2.0 index 1.45 0.0

/* 20 cells of PML (matched to air) at the bottom of the domain form the absorbing
boundary condition at the bottom of the domain */
rectangle position 0.0 1.0 0.0 1.0 0.0 0.1 pml 0 0 -1 1.0 1 0 0

/* 20 cells of PML (matched to SiO2) at the top of the domain form the absorbing
boundary condition at the top of the domain */
rectangle position 0.0 1.0 0.0 1.0 1.9 2.0 pml 0 0 1 2.1025 1 0 0

/* output the electric field intensity at the domain (xz-plane, y = 0.5) */
plot ex steady 0.00 position 0 1.0 0.50 0.50 0.10 1.90 exi
plot ey steady 0.00 position 0 1.0 0.50 0.50 0.10 1.90 eyi
plot ez steady 0.00 position 0 1.0 0.50 0.50 0.10 1.90 ezi
plot ex steady 0.25 position 0 1.0 0.50 0.50 0.10 1.90 exq
plot ey steady 0.25 position 0 1.0 0.50 0.50 0.10 1.90 eyq
plot ez steady 0.25 position 0 1.0 0.50 0.50 0.10 1.90 ezq

/* output the electric field intensity at the domain (yz-plane, x = 0.445) */
plot ex steady 0.00 position 0.445 0.445 0 1.0 0.10 1.90 dxi
plot ey steady 0.00 position 0.445 0.445 0 1.0 0.10 1.90 dyi
plot ez steady 0.00 position 0.445 0.445 0 1.0 0.10 1.90 dzi
plot ex steady 0.25 position 0.445 0.445 0 1.0 0.10 1.90 dxq
plot ey steady 0.25 position 0.445 0.445 0 1.0 0.10 1.90 dyq
plot ez steady 0.25 position 0.445 0.445 0 1.0 0.10 1.90 dzq

/* output the electric field intensity at the domain (yz-plane, x = 0.555) */
plot ex steady 0.00 position 0.555 0.555 0 1.0 0.10 1.90 cxi
plot ey steady 0.00 position 0.555 0.555 0 1.0 0.10 1.90 cyi
plot ez steady 0.00 position 0.555 0.555 0 1.0 0.10 1.90 czi
plot ex steady 0.25 position 0.555 0.555 0 1.0 0.10 1.90 cxq
plot ey steady 0.25 position 0.555 0.555 0 1.0 0.10 1.90 cyq
plot ez steady 0.25 position 0.555 0.555 0 1.0 0.10 1.90 czq

/* output the electric field intensity at the domain (xy-plane, surface of particle) */
plot ex steady 0.00 position 0 1.0 0 1.0 0.94 0.94 fxi
plot ey steady 0.00 position 0 1.0 0 1.0 0.94 0.94 fyi
```

```
plot ez steady 0.00 position 0 1.0 0 1.0 0.94 0.94 fzi
plot ex steady 0.25 position 0 1.0 0 1.0 0.94 0.94 fxq
plot ey steady 0.25 position 0 1.0 0 1.0 0.94 0.94 fyq
plot ez steady 0.25 position 0 1.0 0 1.0 0.94 0.94 fzq

/* output the electric field intensity at the domain (xy-plane, between particle and
spacer) */
plot ex steady 0.00 position 0 1.0 0 1.0 0.98 0.98 gxi
plot ey steady 0.00 position 0 1.0 0 1.0 0.98 0.98 gyi
plot ez steady 0.00 position 0 1.0 0 1.0 0.98 0.98 gzi
plot ex steady 0.25 position 0 1.0 0 1.0 0.98 0.98 gxq
plot ey steady 0.25 position 0 1.0 0 1.0 0.98 0.98 gyq
plot ez steady 0.25 position 0 1.0 0 1.0 0.98 0.98 gzq

/* output the electric field intensity at the domain (xy-plane, between spacer and lower
metal layer) */
plot ex steady 0.00 position 0 1.0 0 1.0 1.00 1.00 hxi
plot ey steady 0.00 position 0 1.0 0 1.0 1.00 1.00 hyi
plot ez steady 0.00 position 0 1.0 0 1.0 1.00 1.00 hzi
plot ex steady 0.25 position 0 1.0 0 1.0 1.00 1.00 hxq
plot ey steady 0.25 position 0 1.0 0 1.0 1.00 1.00 hyq
plot ez steady 0.25 position 0 1.0 0 1.0 1.00 1.00 hzq

/* plot the refractive index */
plot refractive position 0.0 1.0 0.50 0.50 0.0 2.0 en1
plot refractive position 0.0 1.0 0.0 1.0 0.96 0.96 en2
```

C.4. Infrared dipole antenna

Simulation Parameters;

- Metal: Au, Substrate: SiC, Incident Wavelength: 10.6 µm, Grid Size: 50 nm
- Dipole Antenna: Gap = 100 nm, Resonant Antenna Length = 16.4 µm, Antenna Width = 400 nm, Dipole Gold t_{Au} = 100 nm

```
wavelength 10.6        /* wavlength is 10.6 um */
x_node 400             /* # cells in domain x-dimension */
y_node 120             /* # cells in domain y-dimension */
z_node 200             /* # cells in domain z-dimension */
x_dim 20.0             /* Length of the domain x-dimension */

/* excite a normally incident plane wave traveling in the upward (z) direction */
plane_source xy position 0.0 20.0 0.0 6.0 0.50 1 0 0 1 0 uniform 0 0
plane_source xy position 0.0 20.0 0.0 6.0 0.50 0 1 0 1 90 uniform 0 0
```

```
/* whole block fills the domain with air */
rectangle position 0.0 20.0 0.0 6.0 0.0 10.0 index 1.0 0.0

/* first block forms a dipole antenna with gold */
rectangle position 1.75 9.95 2.8 3.2 5.4 5.5 dispersive 13.54 57.55
rectangle position 10.05 18.25 2.8 3.2 5.4 5.5 dispersive 13.54 57.55

/* next block fills the domain with SiC as substrate */
rectangle position 0.0 20.0 0.0 6.0 5.5 10.0 dispersive 0.0605 1.074

/* 8 cells of PML (matched to air) at the bottom of the domain form the absorbing
boundary condition at the bottom of the domain */
rectangle position 0.0 20.0 0.0 6.0 0.00 0.40 pml 0 0 -1 1.0 1 0 0

/* 8 cells of PML (matched to SiC) at the top of the domain form the absorbing
boundary condition at the top of the domain */
rectangle position 0.0 20.0 0.0 6.0 9.60 10.0 pml 0 0 1 0.00366025 1 0 0

/* output the electric field intensity at the domain (xz-plane, y = 3.0) */
plot ex steady 0.00 position 0 20.0 3.0 3.0 0.40 9.60 exi
plot ey steady 0.00 position 0 20.0 3.0 3.0 0.40 9.60 eyi
plot ez steady 0.00 position 0 20.0 3.0 3.0 0.40 9.60 ezi
plot ex steady 0.25 position 0 20.0 3.0 3.0 0.40 9.60 exq
plot ey steady 0.25 position 0 20.0 3.0 3.0 0.40 9.60 eyq
plot ez steady 0.25 position 0 20.0 3.0 3.0 0.40 9.60 ezq

/* output the electric field intensity at the domain (yz-plane, x = 10.0) */
plot ex steady 0.00 position 10.0 10.0 0.0 6.0 0.40 9.60 dxi
plot ey steady 0.00 position 10.0 10.0 0.0 6.0 0.40 9.60 dyi
plot ez steady 0.00 position 10.0 10.0 0.0 6.0 0.40 9.60 dzi
plot ex steady 0.25 position 10.0 10.0 0.0 6.0 0.40 9.60 dxq
plot ey steady 0.25 position 10.0 10.0 0.0 6.0 0.40 9.60 dyq
plot ez steady 0.25 position 10.0 10.0 0.0 6.0 0.40 9.60 dzq

/* output the electric field intensity at the domain (xy-plane, surface of dipole antenna)
*/
plot ex steady 0.00 position 0 20.0 0 6.0 5.4 5.4 fxi
plot ey steady 0.00 position 0 20.0 0 6.0 5.4 5.4 fyi
plot ez steady 0.00 position 0 20.0 0 6.0 5.4 5.4 fzi
plot ex steady 0.25 position 0 20.0 0 6.0 5.4 5.4 fxq
plot ey steady 0.25 position 0 20.0 0 6.0 5.4 5.4 fyq
plot ez steady 0.25 position 0 20.0 0 6.0 5.4 5.4 fzq
```

```
/* output the electric field intensity at the domain (xy-plane, middle of dipole antenna) */
plot ex steady 0.00 position 0 20.0 0 6.0 5.45 5.45 gxi
plot ey steady 0.00 position 0 20.0 0 6.0 5.45 5.45 gyi
plot ez steady 0.00 position 0 20.0 0 6.0 5.45 5.45 gzi
plot ex steady 0.25 position 0 20.0 0 6.0 5.45 5.45 gxq
plot ey steady 0.25 position 0 20.0 0 6.0 5.45 5.45 gyq
plot ez steady 0.25 position 0 20.0 0 6.0 5.45 5.45 gzq

/* output the electric field intensity at the domain (xy-plane, between dipole antenna and substrate) */
plot ex steady 0.00 position 0 20.0 0 6.0 5.5 5.5 hxi
plot ey steady 0.00 position 0 20.0 0 6.0 5.5 5.5 hyi
plot ez steady 0.00 position 0 20.0 0 6.0 5.5 5.5 hzi
plot ex steady 0.25 position 0 20.0 0 6.0 5.5 5.5 hxq
plot ey steady 0.25 position 0 20.0 0 6.0 5.5 5.5 hyq
plot ez steady 0.25 position 0 20.0 0 6.0 5.5 5.5 hzq

/* plot the refractive index */
plot refractive position 0.0 20.0 3.0 3.0 0.00 10.0 en1
plot refractive position 0.0 20.0 0.0 6.0 5.45 5.45 en2
```

APPENDIX D

GAP SURFACE PLASMON EFFECTIVE REFECTIVE INDICES AND PROPAGATION LENGTHS AT THE INTERFACE BETWEEN METALS AND SILICON OXIDE

D.1. Copper (Cu)

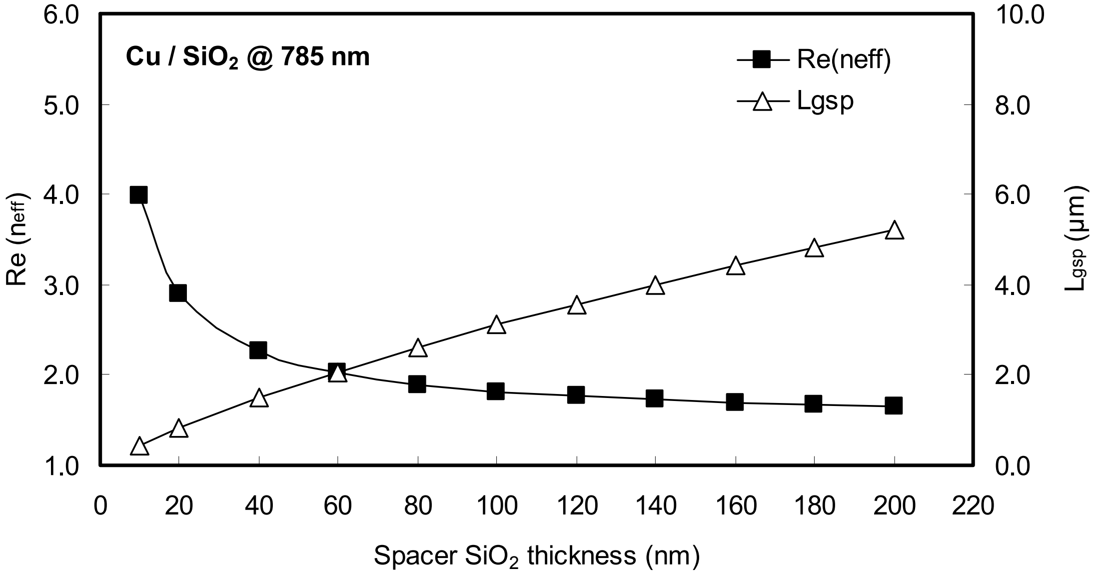

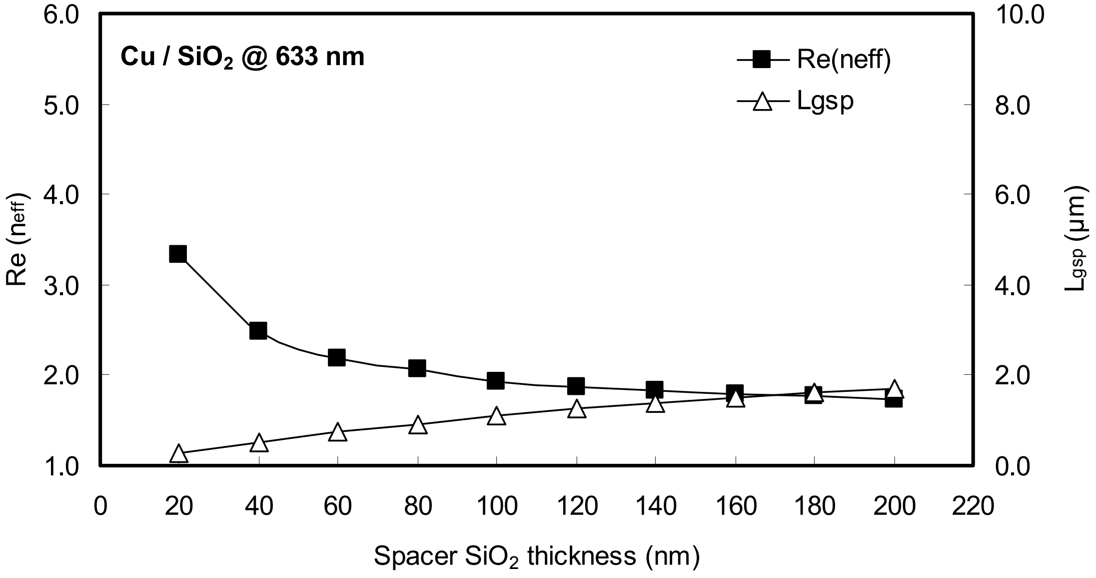

D.2. Aluminum (Al)

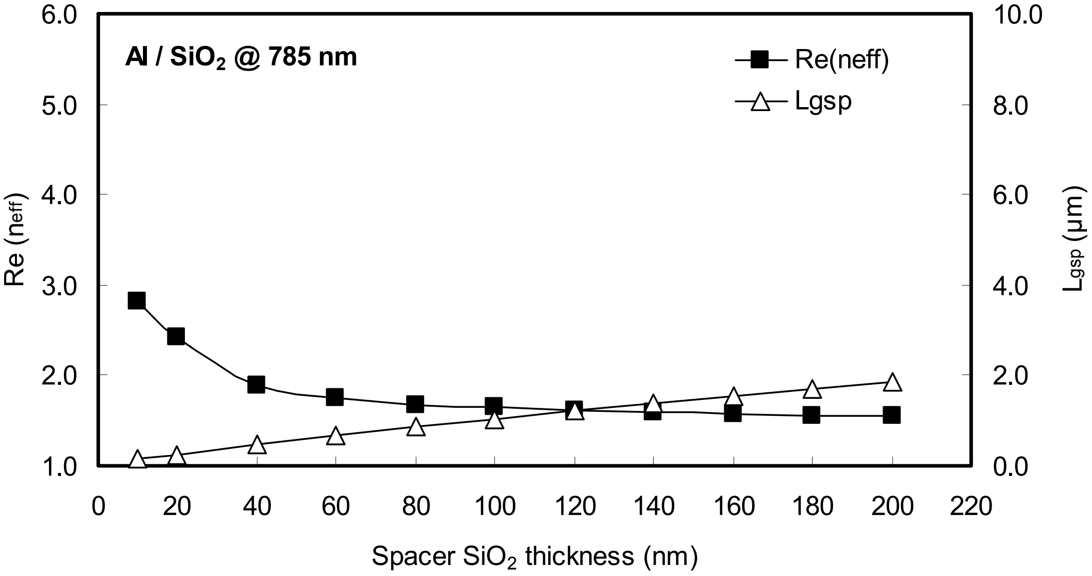

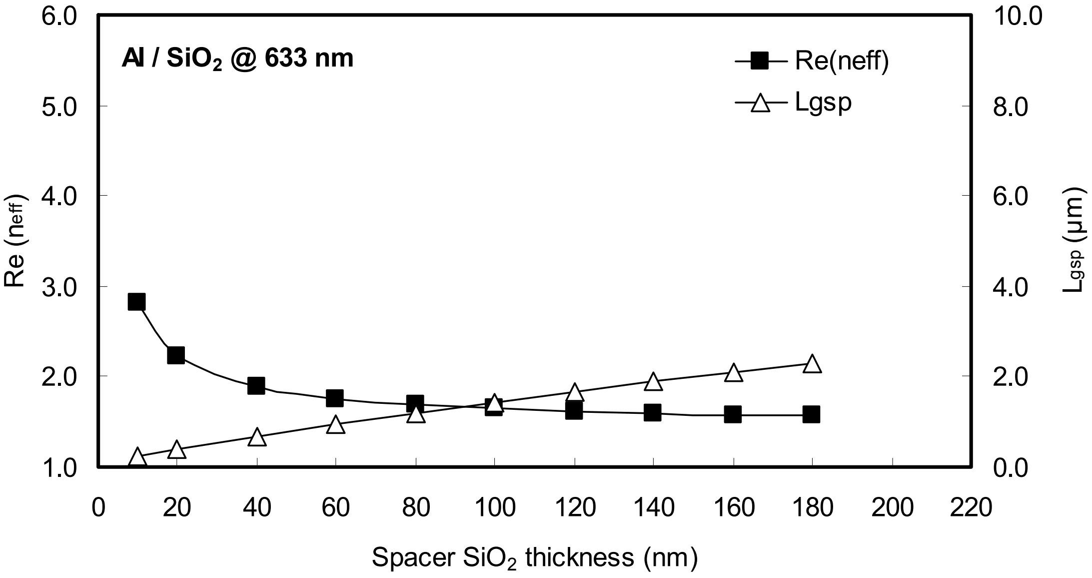

D.3. Tungsten (W)

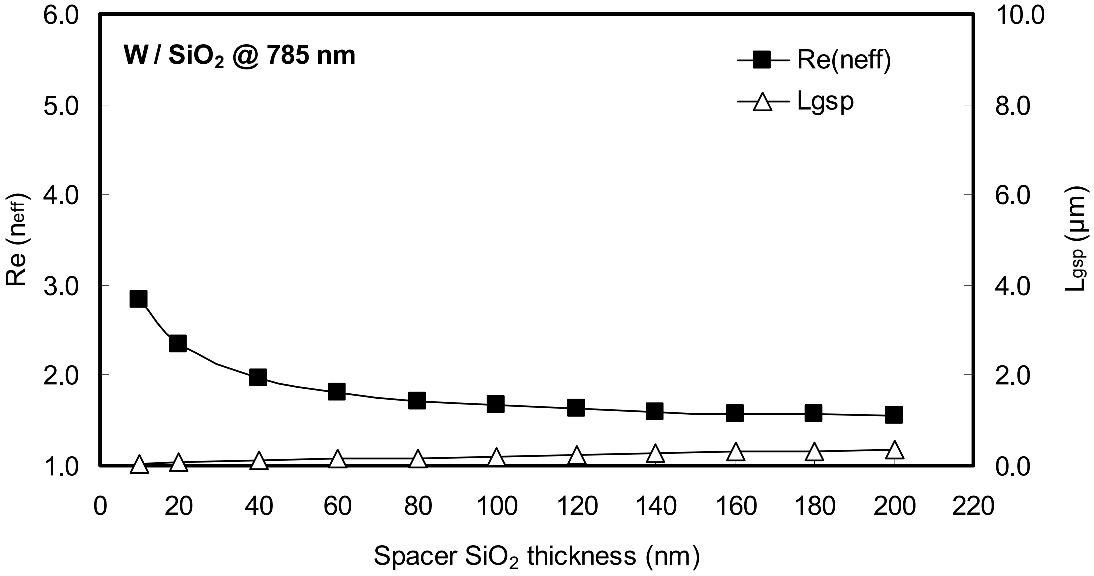

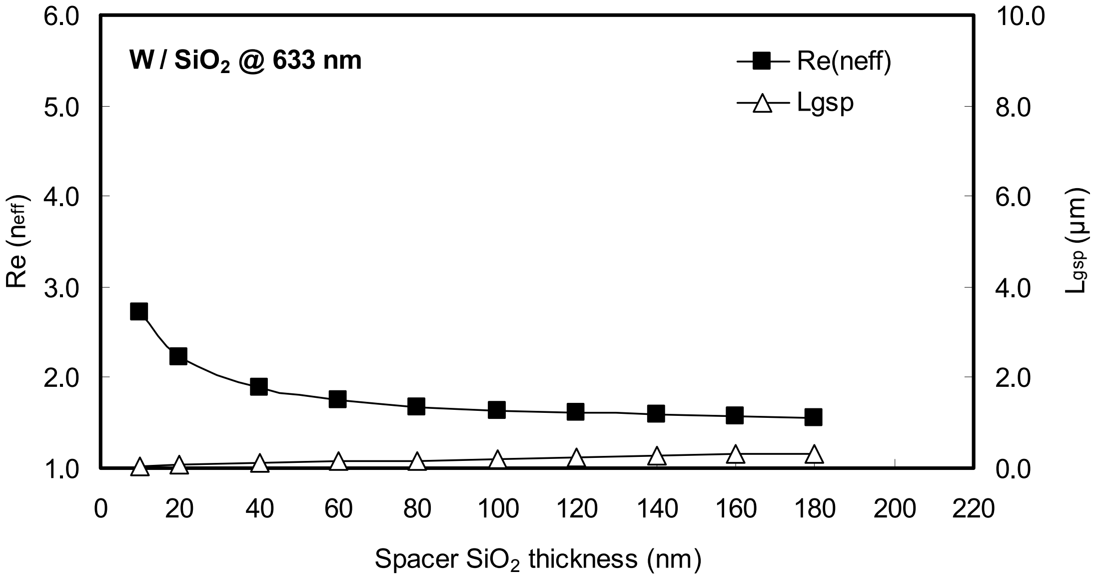

D.4. Gold (Au)

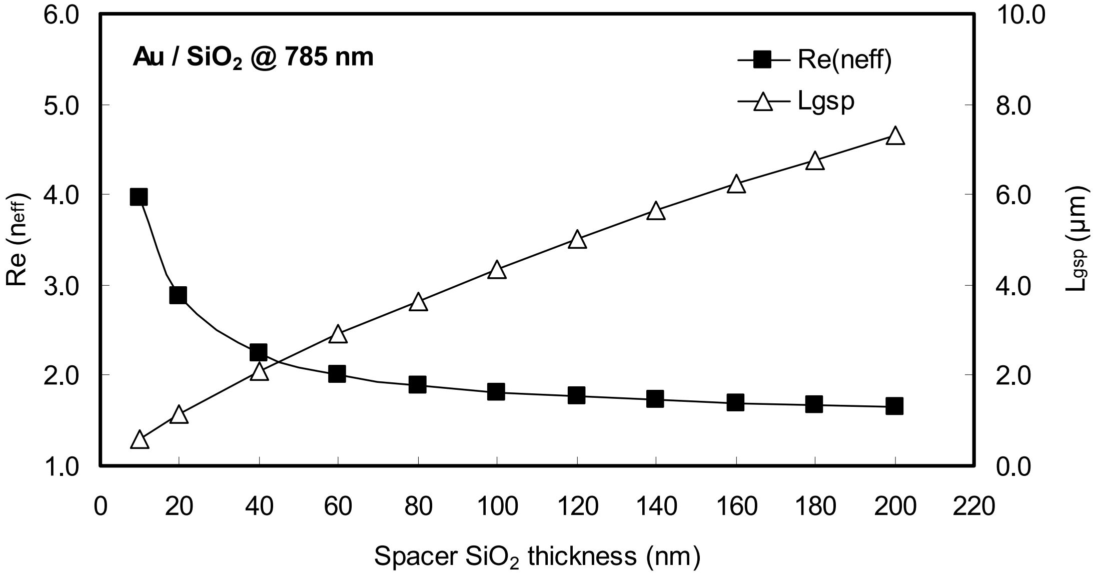
Au / SiO$_2$ @ 785 nm
Re(neff)
Lgsp
Re (neff)
Lgsp (µm)
6.0
5.0
4.0
3.0
2.0
1.0
10.0
8.0
6.0
4.0
2.0
0.0
0
20
40
60
80
100
120
140
160
180
200
220
Spacer SiO$_2$ thickness (nm)

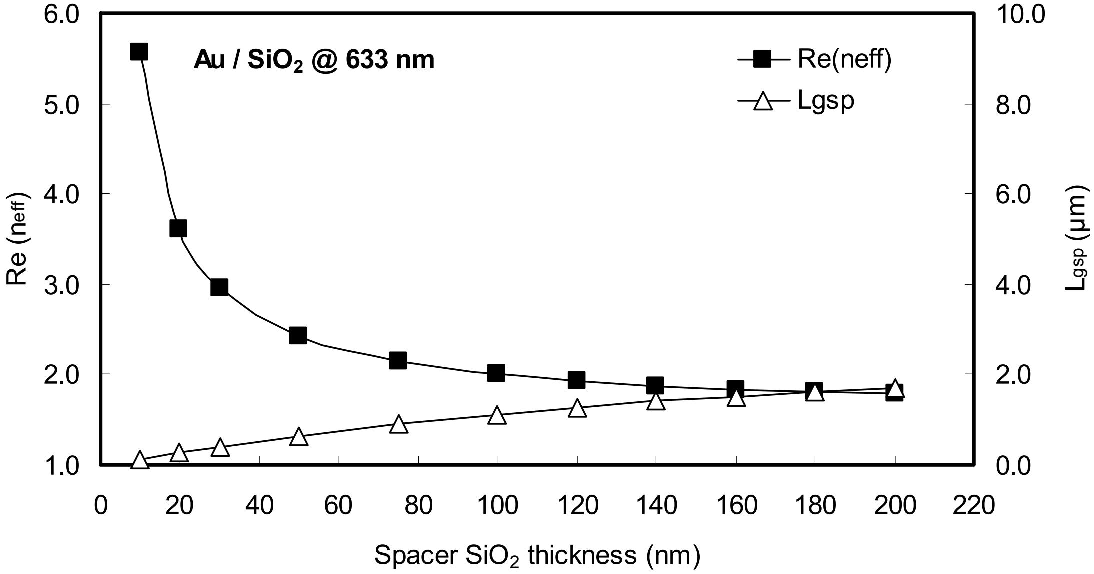
Au / SiO$_2$ @ 633 nm
Re(neff)
Lgsp
Re (neff)
Lgsp (µm)
6.0
5.0
4.0
3.0
2.0
1.0
10.0
8.0
6.0
4.0
2.0
0.0
0
20
40
60
80
100
120
140
160
180
200
220
Spacer SiO$_2$ thickness (nm)

APPENDIX E

OPTICAL PROPERTIES OF POLAR MATERIALS

E.1. Aluminum Oxide. (Al_2O_3)

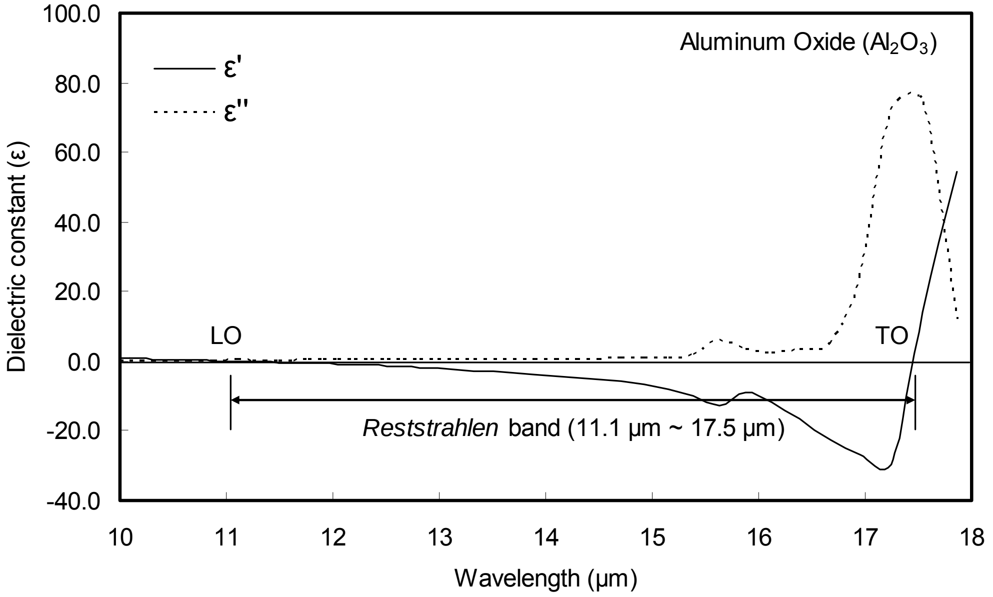

E.2. Gallium Arsenide (GaAs)

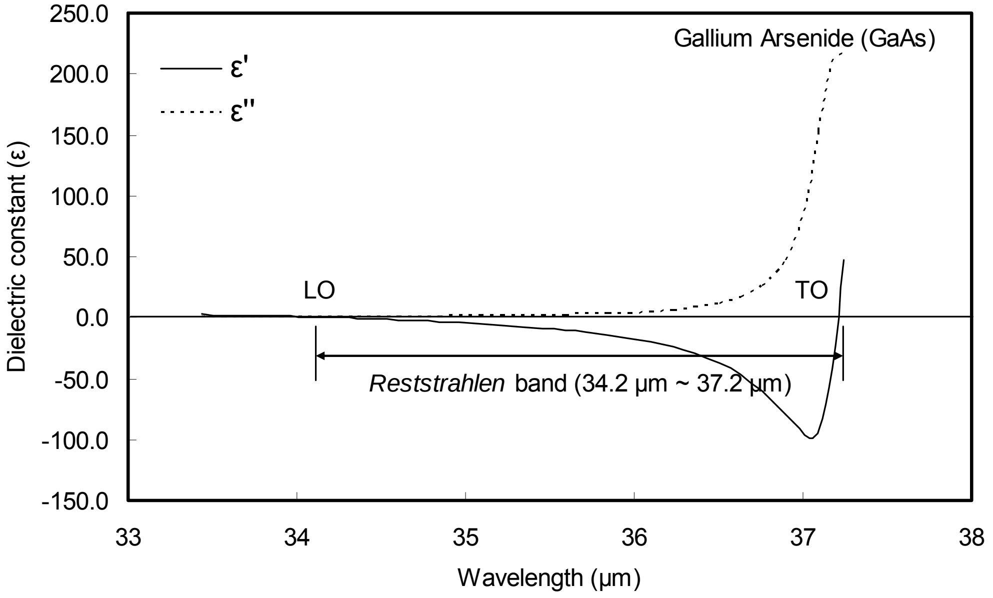

E.3. Cadmium Telluride (CdTe)

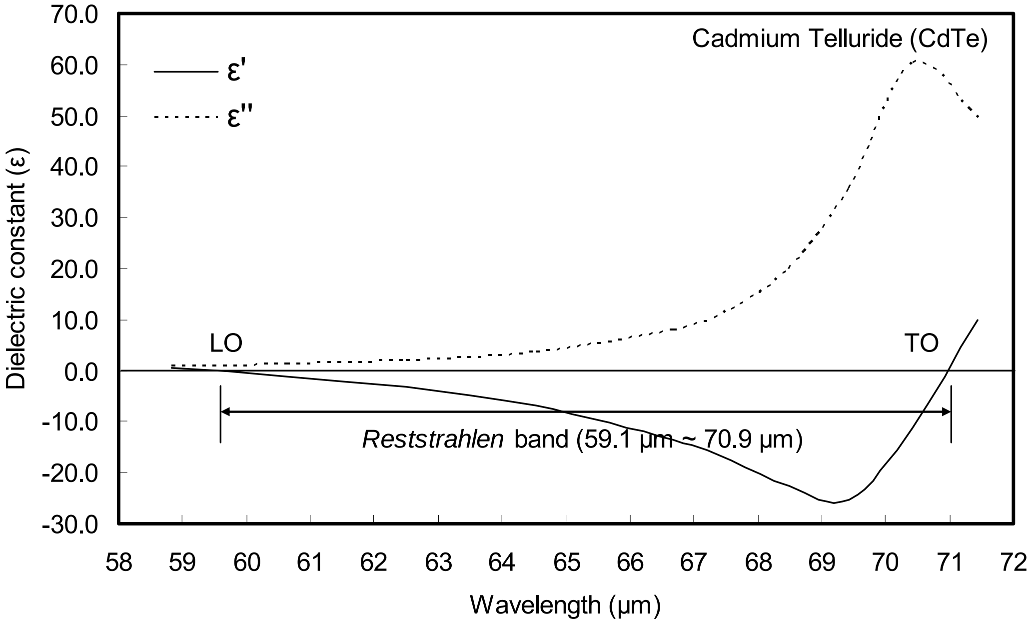

E.4. Lead Selenium (PbSe)

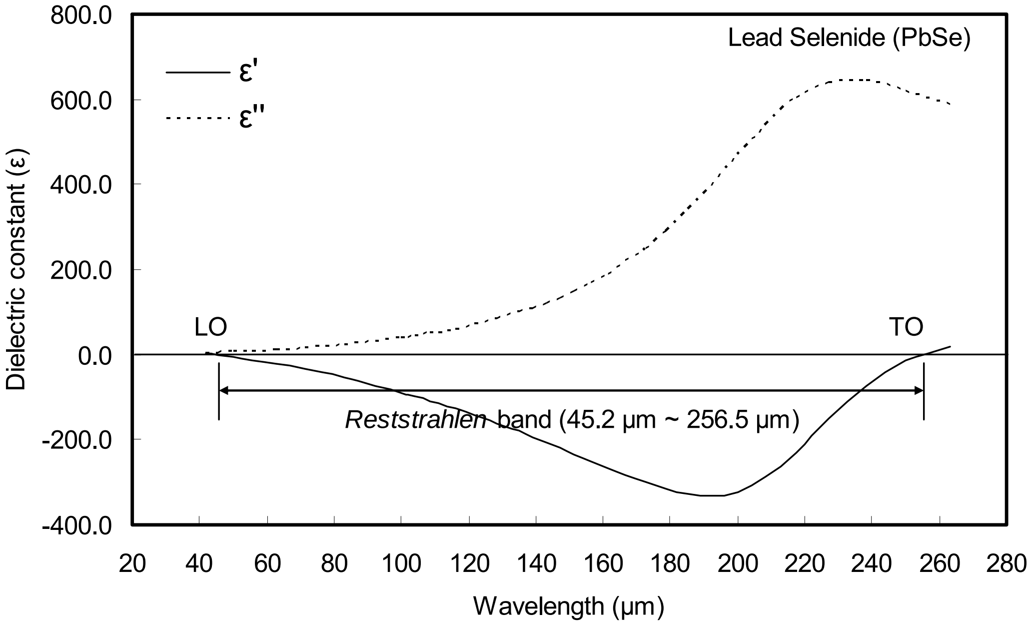

APPENDIX F

SURFACE PHONON POLARITONS EFFECTIVE REFRACTIVE INDEX AND PROPAGATION LENGTHS AT THE INTERFACE BETWEEN POLAR MATERIALS AND AIR

F.1. Aluminum Oxide. (Al_2O_3)

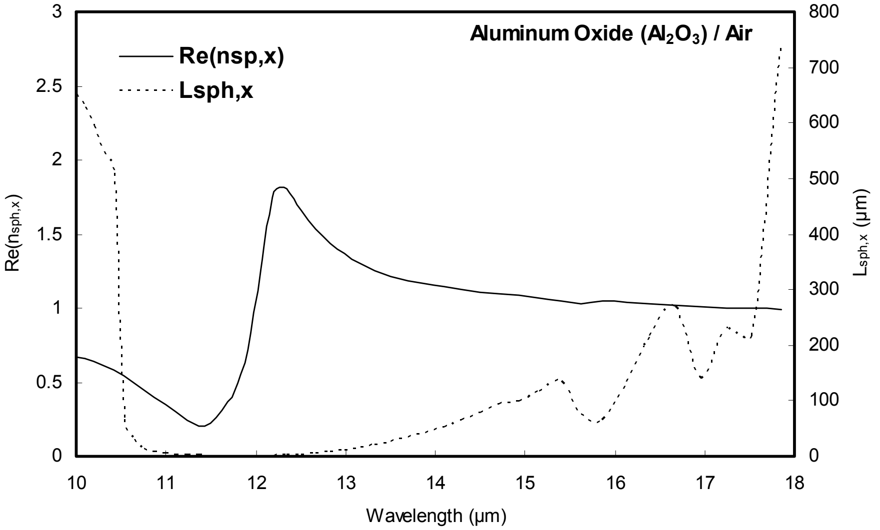

F.2. Gallium Arsenide (GaAs)

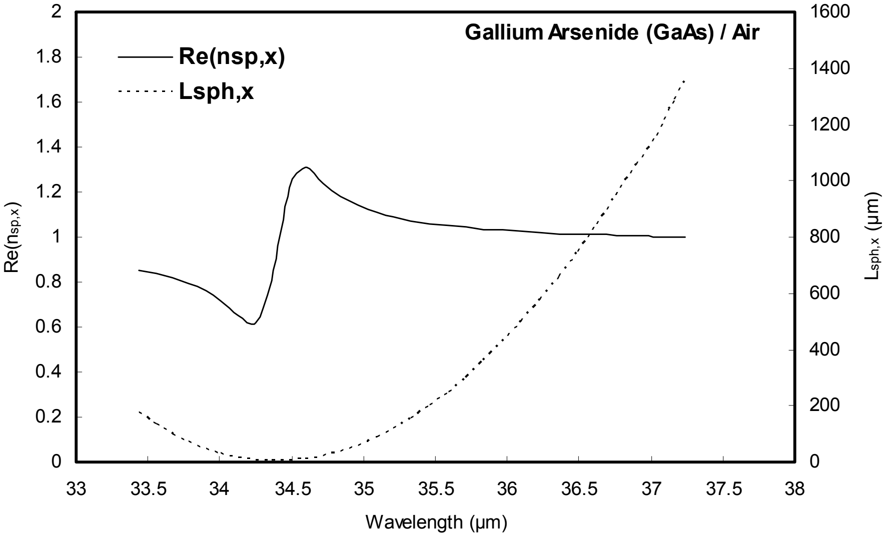

F.3. Cadmium Telluride (CdTe)

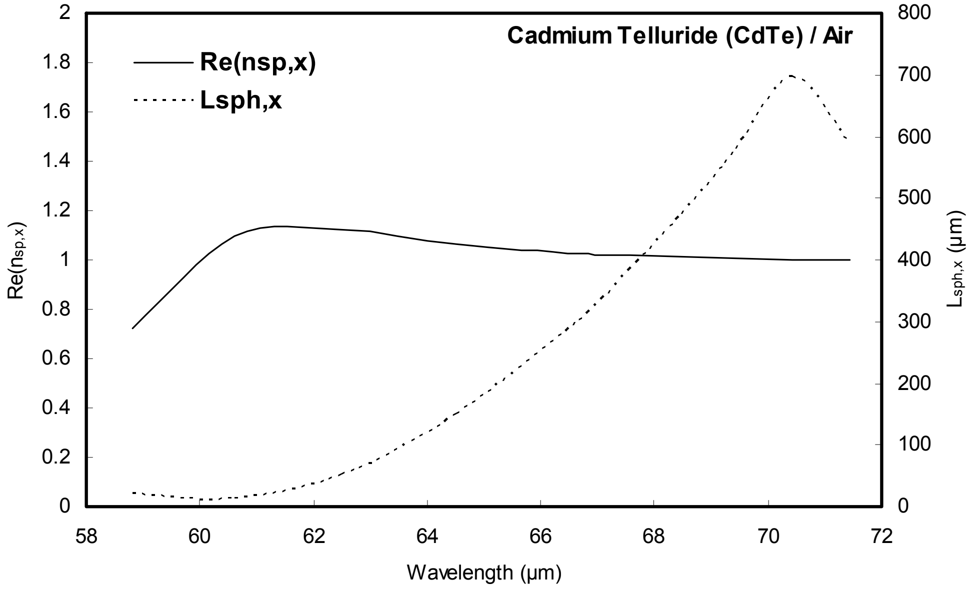

F.4. Lead Selenium (PbSe)

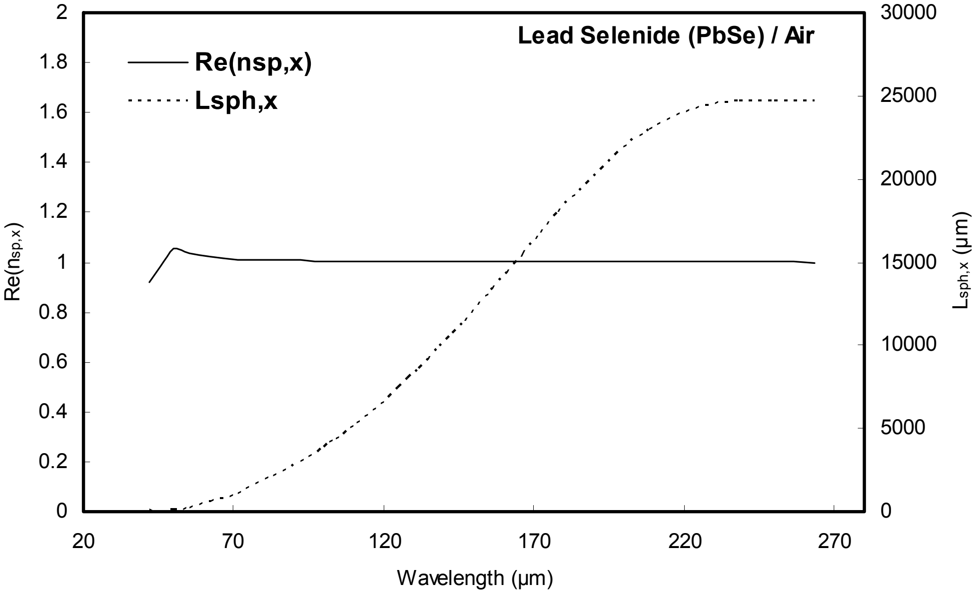

VITA

Hyun Chul Kim was born in Seoul, Korea. He received his B.S. and M.S. degrees in metallurgical engineering from Sungkyunkwan University, Korea in 1994 and 1997, respectively. He started to work at Samsung Electronics, Korea, as a process integration engineer, in February 1997. He entered the doctoral program in electrical and computer engineering at Texas A&M University, via the Human Resource Cultivation Program supported by Samsung Electronics, in September 2004 and received his Ph.D. degree in August 2009. He can be reached at the following address:

Hyun Chul Kim
Department of Electrical and Computer Engineering
Texas A&M University
214 Zachry Engineering Center, TAMU 3128
College Station, Texas 77843-3128